

WIDE BAND GAP SEMICONDUCTING THIN FILMS FOR OPTOELECTRONIC
AND SPINTRONIC APPLICATIONS:
RESULTS ON ZINC OXIDE

THESIS

Presented to the Graduate Council
of Texas State University-San Marcos
in Partial Fulfillment
of the Requirements

for the Degree

Master of SCIENCE

by

Casey Smith, B.A.

San Marcos, Texas

August 2004

COPYRIGHT

By

Casey Smith

2004

ACKNOWLEDGEMENTS

I would like to offer my sincere thanks to all those who made this work possible. My thesis advisor, Dr. Carlos Gutierrez, has continuously offered the full extent of his wisdom and resources. His instruction has deepened my understanding of Solid State Physics and motivated me to make a career related to this branch of science. The various projects I've been a part of while working in his research group were always challenging and interesting. It is through his guidance that I have developed a deeper understanding of materials science and a versatile set of skills for conducting scientific inquiry. I am extremely grateful to have worked with such an outstanding experimental physicist.

Dr. Anup Bandyopadhyay has patiently and expertly shown me the intricacies of operation and maintenance for nearly every piece of equipment I've used during this work. He is always cheerful and willing to help me complete tasks that might have otherwise been left undone. I am thankful for such a reliable, intelligent, and knowledgeable co-worker within Dr. Gutierrez's group because without his expertise, I would have lost valuable time and patience in bringing this work together.

Steven Rios, Daniel Ralls and Isabel Gallardo are fellow student members of Dr. Gutierrez's research group. Steven kindly showed me the ropes when I first integrated into the group and continues to offer meaningful discussion and advice on this project. Daniel Ralls has provided steadfast support by absorbing new responsibilities within the

group to give me valuable time as well as assisting me with sample preparation and synthesis. Isabel has also aided me in sample preparation and monitoring of several sputtering processes. Additionally, her support in writing and revising standard operating procedures for X-ray analysis and sample alignment has deepened my understanding of both.

My second committee member, Dr. Wilhelmus Geerts, helped lay the foundation for my current understanding of Modern Physics through his excellent teaching. I thoroughly enjoy talking with Dr. Geerts because his mind quickly captures the essence of the matter at hand. His expertise in device physics and insight as an electrical engineer has widened the scope of my thesis and provided a crucial point of view during the revision of this document. In addition to his wisdom, he has graciously made available the pertinent equipment, personnel, and resources of his lab. I offer my thanks to Dennis Jordan for facilitating the acquisition of I-V characteristics and Chris O'Brien for his diligence in bringing the van der Pauw apparatus online for sample analysis.

My third committee member, Dr. Gary Beall, first challenged and inspired me when I returned to seek my M.S. degree. His unique style of instruction is both empowering and grueling. Dr. Beall graciously inducted me into the ranks of Graduate Research Assistants to investigate nanocomposite materials. This project planted a seed in my mind that has blossomed into a desire to continue meaningful research. Additionally, his encouragement led me to embark on a thrilling and intensive internship at the Air Force Research Lab. His instruction has broadened my knowledge base as a scientist while the research opportunities have expanded my abilities as an

experimentalist. What I appreciate most about Dr. Beall is that he always willing to make time for his students and expects nothing but your best.

I'd like to thank Dr. Heather Galloway for allowing me to make use of her research group's AFM apparatus. Also, her instruction in Quantum Mechanics was very enlightening and taught me the meaning of attention to detail. Eric Botello, a fellow graduate student, graciously made time to conduct the AFM scans and provide data analysis.

William Gibson and Joel Dunn assisted me in diagnosing problems with the RF-50 source and compiled an excellent set of pictures for the RA-IBS system.

Mr. Kevin Matney at Bede Incorporated has been extremely helpful with advice on modeling XRR data as well as helping to sort out various software gremlins.

Finally, I must express my undying gratitude to my family. My parents fostered my love of learning and supported me through college with unwavering enthusiasm. My loving wife has continually encouraged me during the pursuit of my M.S. degree and accommodated my increasingly hectic schedule throughout this research. Marcella, our first born, unknowingly inspires me to greatness not only in academia but life in general.

This manuscript was submitted on July 15th 2004

TABLE OF CONTENTS

	Page
ACKNOWLEDGEMENTS.....	iv
LIST OF TABLES.....	xi
LIST OF FIGURES.....	xiii
CHAPTERS	
I. INTRODUCTION.....	1
1.1 Wide Band Gap Semiconductors	
1.2 Motivation for this Research	
II. BACKGROUND.....	8
2.1 Zinc Oxide Epitaxial Film Growth	
2.1.1 Substrates	
2.1.2 Structure	
2.1.3 Various Fabrication Techniques	
2.1.4 Deposition Temperature	
2.1.5 Oxygen Partial Pressure	
2.2 Sapphire/Zinc Oxide Lattice Mismatch	
2.2.1 Sapphire Properties	
2.2.2 Plane Alignment	
2.2.3 Growth Evolution	

2.2.4	Buffer Layers	
2.2.4.1	Homoepitaxial Buffer Layers	
2.2.4.2	Heteroepitaxial Buffer Layers	
2.3	Carriers in Zinc Oxide	
2.3.1	Doping Asymmetry	
2.3.2	Hydrogen in ZnO	
2.3.3	Native Defects	
2.3.4	N-type Doping	
2.4	P-type Zinc Oxide	
2.4.1	Nitrogen Doping	
2.4.2	Codoping and Cluster Doping	
2.5	Diluted Magnetic Semiconducting ZnO	
2.5.1	Predictions	
2.5.2	Epitaxial Mn:ZnO	
III.	EXPERIMENTAL.....	56
3.1	Ion Beam Sputter Deposition	
3.2	Radical Assist –Ion Beam Sputtering (RA-IBS) System	
3.3	Substrate Preparation	
3.4	Experimental Matrices	
IV.	X-RAY ANALYSIS.....	68
4.1	Theory	
4.2	Bede D1 Diffractometer	
4.2.1	Types of Scans	

4.2.2	XRR Modeling with REFS	
4.2.3	HRXRD Modeling with RADS	
4.3	HRXRD Data	
4.3.1	Substrate Cleaning	
4.3.2	Oxygen Partial Pressure	
4.3.3	Oxygen Deficient Film	
4.3.4	Deposition Temperature	
4.3.5	Buffer Layers	
4.3.6	N-type and P-type ZnO	
4.3.7	Mn Doped ZnO	
4.4	Phi Scans	
4.5	Reflectivity (XRR) Data	
V.	ATOMIC FORCE MICROSCOPY ANALYSIS.....	120
5.1	Theory	
5.2	Apparatus	
5.3	AFM Data	
VI.	ELECTRICAL PROPERTIES ANALYSIS.....	126
6.1	Hot Probe Experiment (Thermal EMF)	
6.2	I-V Characteristics	
6.3	Hall Effect Measurement	
VII.	VIBRATING SAMPLE MAGNETOMETER ANALYSIS.....	137
7.1	Theory	
7.2	Apparatus	

7.3 VSM Data

VIII. CONCLUSIONS.....	144
APPENDICES.....	146
BIBLIOGRAPHY.....	166

LIST OF TABLES

Table 1: Properties of various wide band gap semiconductors ⁵⁻⁸	5
Table 2: Zinc Oxide Physical and Chemical Properties ^{7, 14}	9
Table 3: Physical and Chemical Properties of Sapphire ³¹	17
Table 4: ZnO Doping Through Various Techniques ⁵¹	37
Table 5: Characteristics of Homoepitaxial MBE N:ZnO Films ⁶⁰	43
Table 6: Cluster Doping Predictions ⁶³	45
Table 7: IBSD Applications ⁸⁰	58
Table 8: Dual Ion Beam Sputter (DIBS) Applications ⁸⁰	59
Table 9: Phase 1 (undoped ZnO) Experimental Matrix.....	66
Table 10: Phase 2 (doped ZnO) Experimental Matrix.....	67
Table 11: Systematic Extinctions Due to Translational Symmetry Elements ⁸⁷	71
Table 12: XRR Qualitative Features.....	75
Table 13: FWHM of ZnO (002) for Different Plasma Treatments.....	81
Table 14: Approximate Crystallite Size for Different Plasma Treatment.....	83
Table 15: Strain for Different Plasma Treatment.....	85
Table 16: Omega Rocking Curve FWHM for Different O Flow During Deposition.....	87
Table 17: Approximate Crystallite Size for Different O Flow During Deposition.....	88
Table 18: Strain for Different Oxygen Flow During Deposition.....	89
Table 19: Crystallite Size for Different Process Temperatures.....	92

Table 20: Strain for Different Processing Temperatures.....	93
Table 21: Strain for Different Homoepitaxial Buffer Layers.....	96
Table 22: Strain for MgO Buffer Layer Films.....	98
Table 23: Strain for Best Attempts at n and p Type ZnO.....	103
Table 24: Sample Designations for Mn Doped ZnO Films.....	104
Table 25: Strain for Mn Doped ZnO Films.....	105
Table 26: REFS Model Properties for Different Substrate Preparation.....	113
Table 27: REFS Model Properties for Different O Flow During Deposition.....	114
Table 28: REFS Model Properties for Different Deposition Temperatures.....	116
Table 29: REFS Model Properties for Different Homoepitaxial Buffer Layers.....	117
Table 30: REFS Model Properties for Mn Doped ZnO.....	119
Table 31: AFM Data for Optimized Undoped ZnO Sample.....	123
Table 32: Thermal EMF Results for ZnO Films.....	128

LIST OF FIGURES

Figure 1: A depiction of the band theory of solids ³	3
Figure 2: Direct versus indirect band gaps ⁴	4
Figure 3a: Zinc Oxide Crystal Structure ¹⁹	11
Figure 3b: Zinc Oxide Unit Cell ²⁰	11
Figure 4: Condensed Zinc Oxide Phase ²²	12
Figure 5a: Sapphire Hexagonal Crystal ³¹	16
Figure 5b: Corundum Structure ²²	16
Figure 6: Oxygen Sublattice Alignment at Sapphire/ZnO Interface ⁸	18
Figure 7: TEM Images ¹⁸ of ZnO on Al ₂ O ₃	19
Figure 8: Phi scan of the (0112) planes for ZnO and Sapphire ³⁴	20
Figure 9: a-Sapphire as an Alternate Substrate Material ³⁵	21
Figure 10: RHEED Pattern Transition as a Function of Temperature ⁸	22
Figure 11: TEM Micrographs of 2D and 3D ZnO Layers ³⁶	23
Figure 12: Evolution of ZnO (002) Rocking Curve vs. Film Thickness ³⁷	24
Figure 13: AFM images of 2D and 3D ZnO layers ³⁷	25
Figure 14: SEM Micrographs for PLD ZnO Films of Increasing Thickness ³⁸	26
Figure 15: RHEED Pattern Evolution for ZnO on Sapphire with a MgO buffer ¹⁶	29
Figure 16: Reciprocal Space Map for Sapphire, MgO buffer, and ZnO epilayer ⁴³	30
Figure 17: Hydrogen Incorporation into the ZnO Wurtzite Structure ⁴⁵	32

Figure 18: Raman Spectra Showing 6 Hydrogen Related Stretching Modes ⁴⁶	32
Figure 19: Conductivity and Mobility ⁵⁰ vs. Deposition Temperature for Al:ZnO.....	35
Figure 20: Band Gap Shift Due to Increasing Carrier Concentration ⁵⁰	36
Figure 21: Native Donor Defects ⁵³ in ZnO.....	39
Figure 22: Native Acceptor Defects ⁵³ in ZnO.....	39
Figure 23: Nitrogen-Native acceptor Complexes ⁵³	40
Figure 24: Nitrogen Based Double and Single Shallow Donor Defects ⁵³	40
Figure 25: ZnO Lattice Changes as a Function of Mn Concentration ⁷³	50
Figure 26: MR for Undoped (top) and 19% Mn: Doped ZnO:Al Films ⁷³	51
Figure 27: MR for various TM in ZnO prepared by Laser MBE ⁷⁷	52
Figure 28: XRD Peak Shift due to Mn doping ⁷⁸	53
Figure 29: M vs H Hysteresis Curve for 10%Mn:ZnO Film ⁷⁸	53
Figure 30: RT SQUID Generated Hysteresis Loops for 2% Mn:ZnO pellets ⁷⁹	54
Figure 31: RT Hysteresis Loops for 2.2% PLD Mn:ZnO on Quartz ⁷⁹	55
Figure 32: Schematic of a Standard DIBS System ⁸⁰	57
Figure 33: Kaufman Hot Filament Gridded Ion Source ⁸¹	61
Figure 34: Specular vs non-specular geometry ⁸²	62
Figure 35: OAR Atomic Radical Source ⁸³	63
Figure 36: Schematic of OAR Atomic Radical Source ⁸³	63
Figure 37: Bragg Condition for X-ray Diffraction ⁸⁵	69
Figure 38: Sealed Tube X-ray Source ⁸⁵	69
Figure 39: Spectrum of Copper X-ray Source ⁸⁵	70
Figure 40: Symmetric 2Theta-Omega X-ray Scan Setup ⁸⁸	72

Figure 41: Top-Down View of the Bede D1 Diffractometer ⁸⁹	73
Figure 42: Silicon Dual Channel Collimating Crystals ⁸⁹	74
Figure 43: “Good” REFS fit of 2 layer ZnO model.....	76
Figure 44: Omega-2Theta scan of ZnO (002) for Different Plasma Treatments.....	79
Figure 45: Omega Rocking Curve of ZnO (002) for Different Plasma Treatments.....	81
Figure 46: Omega Rocking Curve for Bare Sapphire Substrate.....	82
Figure 47: ω -2 θ curves of Al ₂ O ₃ (006) and ZnO (002) for Different Plasma Treatment.	84
Figure 48: ω -2 θ scan of ZnO (002) for Different O Flow During Deposition.....	86
Figure 49: ω -Rocking Curve of ZnO (002) for Different O Flow During Deposition....	87
Figure 50: ω -2 θ curves for Different O Flow During Deposition.....	88
Figure 51: Omega-2Theta scan of ZnO (002) for Oxygen Starved Film.....	90
Figure 52: ω -2 θ scans of ZnO (002) for Different Processing Temperatures.....	91
Figure 53: ω -Rocking Curve of ZnO (002) for Different Processing Temperatures.....	92
Figure 54: ω -2 θ curves for Different Processing Temperatures.....	93
Figure 55: ω -2 θ scans of ZnO (002) for Different Homoepitaxial Buffer Layers.....	94
Figure 56: Omega Rocking Curves for Different Homoepitaxial Buffer Layers.....	95
Figure 57: ω -2 θ curves for Different Homoepitaxial Buffer Layers.....	96
Figure 58: Omega-2Theta scans of MgO buffer layered ZnO (002)	97
Figure 59: Omega-2Theta Curves for MgO Buffer Layer Samples.....	98
Figure 60: 2Theta-Omega scan of ZnO on MgO.....	99
Figure 61: Omega-2Theta Curves of ZnO (002) for Ga:ZnO and Ga/N:ZnO.....	101
Figure 62: Omega Rocking Curves of ZnO (002) for Ga:ZnO and Ga/N:ZnO.....	102
Figure 63: Omega-2Theta Curves for Ga:ZnO and Ga/N:ZnO.....	103

Figure 64: Omega-2Theta Curves for Mn Doped ZnO Films.....	105
Figure 65: Phi Scan for Sample Exposed to 5 sccm O Radical Plasma Treatment.....	108
Figure 66: Phi Scan for Sample Exposed to No O Radical Plasma Treatment.....	108
Figure 67: Single Layer Model Fit for REFS v3.5b.....	109
Figure 68: Double Layer Model Fit for REFS v3.5b.....	110
Figure 69: Low Density Top Layer as Suggested by Researchers at Bede Inc.....	111
Figure 70: Single Layer Model Generated by REFS Version 4.....	111
Figure 71: 2 Layer model generated by REFS Version 4.....	112
Figure 72: Effect of Substrate Preparation by Oxygen Radical Plasma.....	113
Figure 73: Effect of Oxygen Flow Rate During Deposition.....	114
Figure 74: Effect of Deposition Temperature.....	116
Figure 75: Effect of Homoepitaxial Buffer Layer.....	117
Figure 76: XRR of Ga:ZnO and Ga/N:ZnO.....	118
Figure 77: XRR of Mn Doped ZnO.....	119
Figure 78: Damping Forces for Different Distances Between Sample and Tip ⁹²	120
Figure 79: Sample AFM Cantilever ⁹³	121
Figure 80: Photodiode Configuration ⁹³	121
Figure 81: As Received Sapphire Substrate and Optimized Sample (10X10).....	123
Figure 82: Optimized Sample (3X3).....	124
Figure 83: Optimized Sample (1X1).....	124
Figure 84: Hot Probe Experimental Setup ⁹⁴	126
Figure 85: Band Shifting Due to the Application of a Thermal Gradient ⁹⁴	127
Figure 86: I vs V for an undoped ZnO film at room temperature and 373K.....	130

Figure 87: I-V curves for ZnO 040510 (LT buffer layer)	131
Figure 88: I-V curves for Attempted n and p Type ZnO.....	132
Figure 89: I vs. V Under U-V Irradiation from a Hg Lamp for Undoped ZnO.....	133
Figure 90: Hall Effect ⁹⁵	134
Figure 91: Van der Pauw Configuration for Determining Sheet Resistance ⁹⁵	135
Figure 92: Setup for Determining Hall Voltage and Carrier Mobility ⁹⁵	136
Figure 93: Standard Components of a VSM ⁹⁶	137
Figure 94: Points of Interest for a Standard Hysteresis Loop ⁹⁷	138
Figure 95: In plane Quick VSM Scan of Mn/Ga:ZnO.....	140
Figure 96: Out of Plane Quick VSM Scan of Mn/Ga:ZnO.....	141
Figure 97: Accurate Scan of Mn/Ga/N:ZnO.....	142
Figure 98: Accurate Scan of Mn/Ga:ZnO.....	142
Figure 99: Accurate Scan of Mn:ZnO (400 °C)	143

I. INTRODUCTION

Materials can be classified as metals, insulators, or semiconductors based on their electrical resistivity. Semiconductors are defined¹ as having room temperature resistivities of 10^{-2} to 10^9 ohm-cm. Some classical semiconductor crystals include Silicon, Germanium, and Gallium Arsenide whose applications include diodes, switches, lasers, photovoltaic cells, and transistors. Many important characteristics of these materials are best described using the band theory of Solid State Physics.

Quantum Mechanics has shown that electrons within a material must obey Fermi-Dirac statistics in accordance with the Pauli Exclusion Principle. Exchange symmetry combines both spin and spatial character to define the state of a particle.² Consider a system of two electrons (x_1 and x_2) described by a single wave function. If the spatial states of the two particles (a and b) are identical, then the anti-symmetric spatial state must equal zero.

$$\Psi_a(x_1)\Psi_b(x_2) - \Psi_a(x_2)\Psi_b(x_1) = 0$$

Hence, the spatial component of the Schrödinger wave function that describes a system of two fermions must be symmetric (otherwise the wave function collapses). This in turn requires the spin state to be anti-symmetric. For example, if both electrons have the quantum numbers $n=2$, $l=1$, $m_l=1$ (spatial) then the spins must be opposite ($m_s=+1/2$ and $-1/2$ respectively). It is important to note that the Pauli Exclusion Principle holds true for

any system of multiple fermions but only if they are indistinguishable (a system consisting of a proton and electron doesn't count because you can tell the difference between these two fermions).

Bloch predicted that the solutions to Schrödinger's equation for an electron in a crystal lattice take the form of a plane wave multiplied by a function with the periodicity of the lattice. Further analysis shows that localized wave packets (electrons) propagate freely through the Bloch potential created by the ion cores that make up the lattice. The Kronig-Penney Model is comprised of an array of square potential wells and its solutions provide the necessary periodic function required for the Bloch form.

The general consequence of the previous Quantum Mechanical principles is that there are some electronic states that are forbidden due to the absence of a proper solution for the electron wave function. These states tend to form "bands" within the material representing energy states that are inaccessible to the electrons.

Even at $T=0K$ all electrons are not at the same energy level. They are forced to settle into available states in order of increasing energy. My professor for Solid State Physics offered an analogy to an apartment complex. Only 2 electrons with the same spatial quantum numbers can fit into an apartment (spin up and spin down) and everyone wants to be on the ground floor (stairs require energy). The highest level occupied by electrons at absolute zero is defined at the edge of the valence band in a material. Electrons in the valence band do not participate in conduction. The first unfilled level above the valence band is defined as the edge of the conduction band. Metals exhibit no inaccessible states separating their overlapping valence and conduction bands, insulators

have appreciable gaps, and semiconductors fall somewhere in the middle as depicted in figure 1.

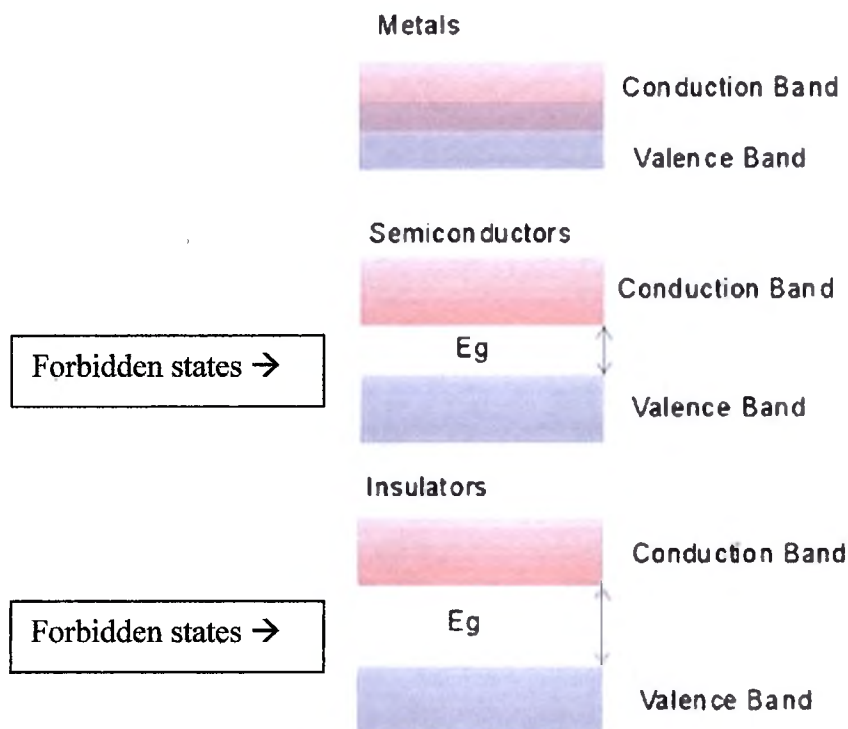


Figure 1: A depiction of the band theory of solids³

Electrons gain access to the conduction band through the addition of energy. Thermal energy, optical excitation, and electrical bias are just a few ways to coerce an electron to jump the gap. Once the electron leaves the crowded valence band and reaches the conduction band it is free to move about because there are many more states available than electrons to occupy them. So while semiconductors are poor conductors at room temperature due to the absence of electrons in the conduction band, at higher temperatures, there will be a significant fraction of electrons with enough energy to reach the conduction band and consequently the conductivity increases as more thermal energy becomes available. Similarly, application of light energy of the appropriate wavelength

(i.e. band gap energy) can dramatically increase the conductivity of a semiconductor material due to an increase of charge carriers in the conduction band.

Bands in semiconductors are further classified into direct and indirect gaps. The actual shape of the bands in a solid can be modeled with parabolic functions as depicted in figure 2.

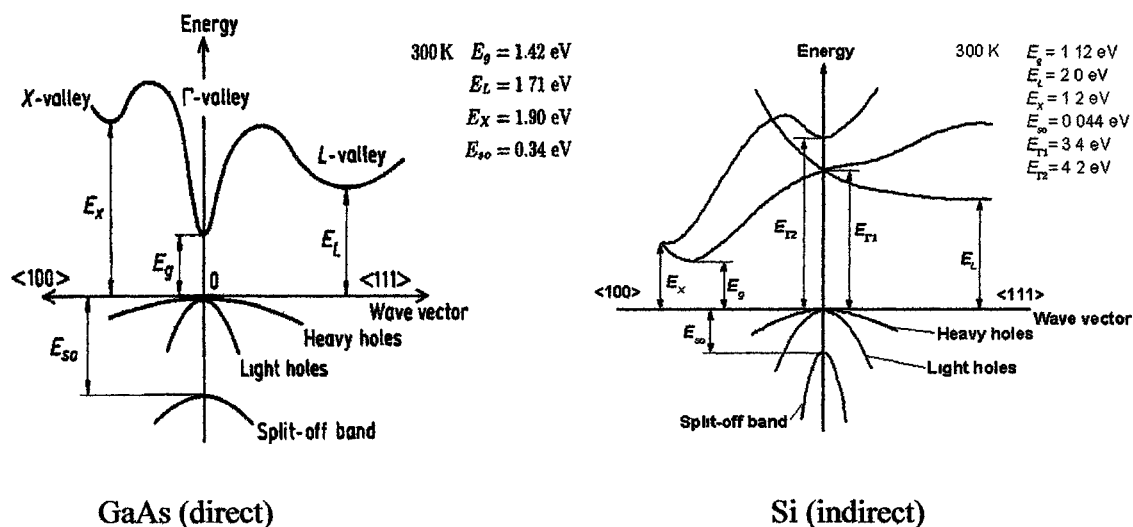


Figure 2: Direct versus indirect band gaps⁴

The major difference between direct and indirect band gaps is the alignment of the valence band maximum and conduction band minimum in wave vector or k-space. Transitions from the valence to conduction band for an indirect band gap semiconductor must be mediated by a lattice vibration or phonon to conserve wave number. This additional phonon mediation has important ramifications for LEDs, lasers, and photovoltaic cells where absorption and emission of light via transitions needs to be as favorable as possible, making indirect band gap semiconductors an inefficient choice for these devices.

1.1 Wide Band Gap Semiconductors

Semiconductors are categorized rather arbitrarily² as any insulator with a band gap smaller than ~ 2 eV. However, the more recent designation of wide band gap semiconductor includes materials with energy gaps as large as 8eV. Several examples of the most extensively studied wide band gap semiconductors and their properties are listed in table 1.

Material	Structure	Density (g/cm ³)	Bandgap (eV)	Electron mobility (cm ² /Vs)	Hole Mobility (cm ² /Vs)	Exciton binding energy (meV)
ZnO	Wurtzite	5.68	3.37	100-200	180	60
ZnSe	Zinc blende	4.04	2.70	600	28	20
ZnS	Wurtzite	4.09	3.8	180	10	39
GaN	Wurtzite	6.15	3.39	1000	350	21
α -SiC	Wurtzite	3.21	2.86	400	90	
AlN	Wurtzite	3.25	6.026	300	14	
GaP	Zinc blende	4.14	2.26	250	150	
Diamond	Diamond	3.515	5.6	2200	1800	
MgO	Rock salt	3.6	7.8			

Table 1: Properties of various wide band gap semiconductors⁵⁻⁸

Wide band gap semiconductors have received considerable attention in recent years due to their potential applications. High efficiency optoelectronic devices such as UV-blue emitting diodes and lasers could help companies realize affordable solid state lighting as well as high density data storage. Various high power, high temperature and high frequency electronics for sensors could allow for innovative non-destructive testing

techniques, gas detection, and voltage regulation. Semiconductor spintronics may also be realized by engineering the properties of these materials.

1.2 Motivation for this Research

Zinc Oxide has been the subject of numerous studies due to its high conductivity, piezoelectricity, large exciton binding energy, optical transparency, and radiation hardness. This material is environmentally benign, abundant, and extremely versatile with potential applications ranging from transparent solar cell windows to spintronic transistors. Our principle motivation for this research was to further establish well defined protocols for reliably fabricating intrinsic ZnO epitaxial films by controlling substrate preparation, deposition temperature, oxygen partial pressure, and buffer layers. Through the use of various dopants, we also set our sights on overcoming difficulties in fabricating p-type and diluted magnetic ZnO.

II. BACKGROUND

While GaN has received considerable attention for possible UV and blue light emitters, ZnO offers some distinct advantages. Firstly, Ga is rarer than gold (but only ~1/3 as expensive) while ZnO is easily obtained and used abundantly in paint pigment, vulcanized rubber, soil additives, cosmetics, and various ointments.⁹ Secondly, ZnO has an exciton binding energy which is 2.4 times larger than GaN, making it a more efficient emitter and lasing material.¹⁰ Thirdly, Eagle Picher has recently developed a Seeded Physical Vapor Transport (SPVT) process to reliably produce bulk ZnO wafers.⁹ Fourthly, ZnO offers more easily managed thermal and atmospheric processing conditions than GaN due to lower kinetic barriers to solid formation.¹¹ Finally, ZnO is more radiation resistant than GaN.¹²

Zinc Oxide is a binary II-VI compound direct band gap semiconductor. Zincite is a naturally occurring ore of ZnO that may contain some Mg or Fe.¹³ The mineral is relatively rare and typically forms along with other minerals as the result of hydrothermal replacement deposits with the premier North American localities in New Jersey. Pure ZnO is white but field samples exhibit deep red to orange color due to the presence of Mg. Some of the more important physical and chemical properties of this material are listed in table 2.

Atomic Weight	40.69 amu
Enthalpy of Formation	-350.5 kJ/mol
Melting Point	2248 K
Enthalpy of Fusion	52.30 kJ/mol
Specific Heat	0.494 J/g*K
Thermal Expansion Coefficient	$4.5-7.7 \cdot 10^{-6} \text{ } ^\circ\text{C}^{-1}$ (from 50-300 $^\circ\text{C}$)
Hardness	4-5 (Mohs scale)
Density	5.68 g/cm^3
Index of Refraction	~ 2.01
Solubility	insoluble- H_2O , slightly soluble-dilute acid
CAS registry #	1314-13-2
Magnetic Susceptibility	$-27.7 \cdot 10^{-6} \text{ cm}^3/\text{mol}$
Lattice Potential Energy	4142 kJ/mol
Energy Gap (direct)	3.2 eV @ room temperature (387nm)
Exciton Binding Energy	$\sim 60 \text{ meV}$
Electron effective mass	$0.24 m_0$
Hole effective mass	$0.59 m_0$
Electron mobility (ZnO ceramics)	$100-200 \text{ cm}^2/\text{V}\cdot\text{s}$
Hole mobility (ZnO ceramics)	$180 \text{ cm}^2/\text{V}\cdot\text{s}$
Thermal Conductivity (ZnO crystals)	$\sim 540 \text{ mW/cm}\cdot\text{K}$ @300K
Price per gram (99.9995 % purity)	\$1.86-\$2.46 (in 1995)

Table 2: Zinc Oxide Physical and Chemical Properties^{7, 14}

2.1 Zinc Oxide Epitaxial Film Growth

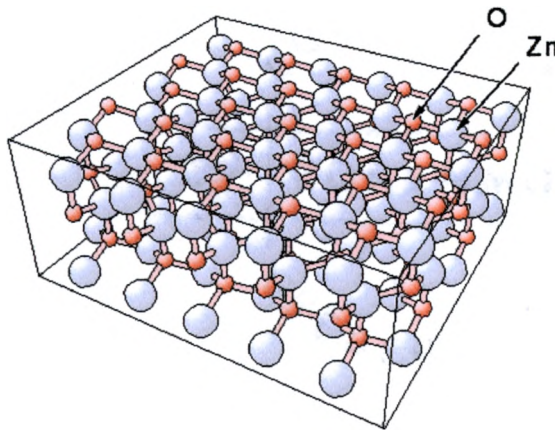
2.1.1 Substrates

Reports in the literature primarily focus on the use of sapphire, silicon, glass, and quartz as substrates for ZnO thin film growth. The goal of producing highly crystalline ZnO requires the use of a template to promote epitaxial growth and thus limits the use of silicon, glass, and quartz as viable substrate materials. Due to its availability and compatibility with the ZnO lattice, alpha or c-plane sapphire is the currently preferred substrate. Several reports have detailed protocols for cleaning sapphire substrates prior to deposition. For instance, Tsurumi et al. detail a degreasing protocol consisting of sonication of sapphire (001) substrates in acetone followed by ethanol.¹⁵ The researchers then anneal the substrates in air for 1 hour at a temperature of 1050 °C to ensure that the surface is atomically flat. Another group headed by Y. Chen reports rinsing their substrates with acetone and methanol followed by a chemical etch in a 3:1 sulfuric acid/phosphoric acid bath at 160 °C for 15 minutes.^{8, 16-17} After a deionized water rinse and spin dry, the sapphire is exposed to oxygen plasma for 30 minutes at 650 °C. The solvents and acid etch were utilized to remove organic contaminants from the surface while the plasma treatment ensured that the surface of the sapphire was oxygen terminated. The most crucial step in preparing the substrates for epitaxial growth is oxygen plasma treatment because any remaining contaminants from the surface of the substrates, particularly carbon compounds, will quickly recombine with atomic oxygen species and be gently sputtered off and swept out by the vacuum system. In a study of Plasma Enhanced Molecular Beams Epitaxy (PEMBE) ZnO deposited on sapphire,

Vigue et al. point out that the first planes of ZnO stack without any disorder on oxygen plasma treated substrates due to the efficiency of this cleaning process.¹⁸

2.1.2 Structure

Under normal conditions, ZnO forms the wurtzite (space group $P6_3mc$, C_{6v} symmetry group) structure depicted in figures 3a and 3b.



ZnO (wurtzite) lattice (0001) stacking

Wurtzite is a hexagonal structure of 2 different atoms. Each atom has 4 nearest neighbors of the opposite type.
 $c/a = (8/3)^{1/2}$

Figure 3a: Zinc Oxide Crystal Structure¹⁹

Each unit cell (outlined in blue) contains 2 Zn atoms and 2 O atoms. Note the tetrahedral coordination of the ZnO bonds.

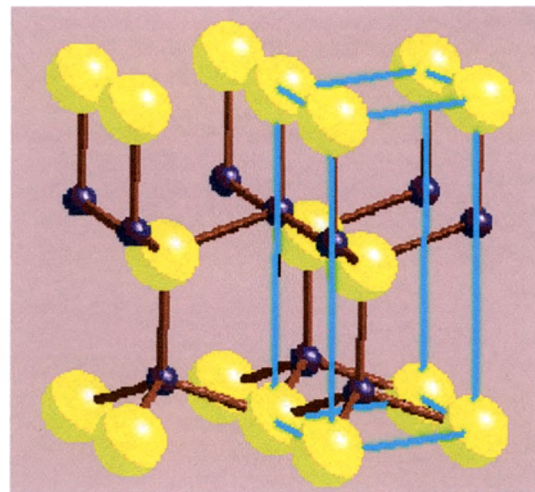


Figure 3b: Zinc Oxide Unit Cell²⁰

The unit cell contains 2 formula units²¹ and has a volume of 47.58 cubic angstroms with lattice parameters $a = 0.32494$ nm and $c = 0.52038$ nm. There also exists a high- pressure allotrope with the rocksalt structure (space group $Fm\bar{3}m$) depicted in figure 4.

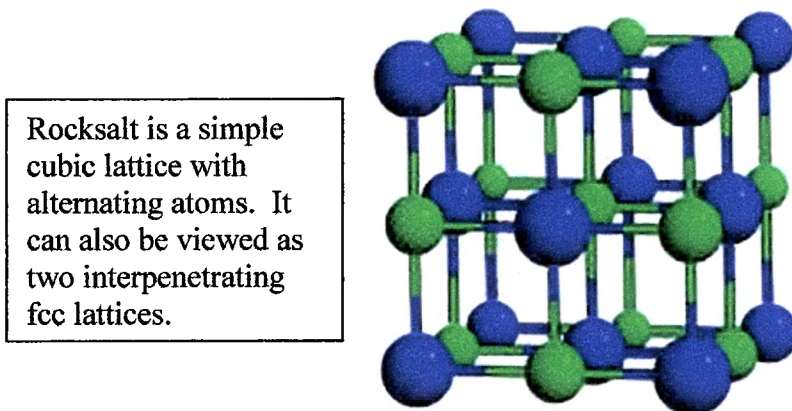


Figure 4: Condensed Zinc Oxide Phase²²

When the ambient pressure is raised above 9.3 GPa, ZnO, like many group III nitrides, transforms from the wurtzite to rocksalt structure via intermediate states that are still not completely understood.²³

2.1.3 Various Fabrication Techniques

There exist many techniques for growing both doped and undoped ZnO including Chemical Vapor Deposition (CVD), Molecular Beam Epitaxy (MBE), Radio Frequency/Direct Current Magnetron Sputtering (RFMS/DCMS), Spray Pyrolysis, Pulsed Laser Deposition (PLD), Chemical Beam Deposition, Electrodeposition, Metal Organic Chemical Vapor Deposition (MOCVD), Seeded Physical Vapor Transport (SPVT), and Evaporation. Some researchers have claimed that reactive sputtering is the best technique for epitaxial ZnO growth.²⁴ This process discharges gas into a chamber where a metal target is being sputtered. Metal atoms from the target material must favorably combine with the gas species on the substrate surface to produce compound

film growth. However, one must be careful to maintain not only the proper stoichiometry between gas species and metal ions but also ensure that their reaction maintains a stable thermodynamic probability. Our process utilizes ceramic targets composed of the compounds we are attempting to deposit and thus allows for more flexibility. The reactive assist gases in our system can be varied to supplement the growth of the film or introduce additional dopant species not already present in the target.

2.1.4 Deposition Temperature

Deposition temperature during ZnO growth has been shown to directly influence photoluminescence spectra, crystallinity, resistivity, and growth rate. Matsuoka et al.²⁵ report that the FWHM of the ZnO (002) peak grown on thermally oxidized silicon monotonically decreases as the deposition temperature is raised from 30 to 300 °C. This would indicate that higher deposition temperatures lead to a more ordered crystalline array of ZnO planes parallel to the substrate surface. However, in the same study, the authors show evidence of worsening surface smoothness as evidenced by SEM micrographs. The films deposited at higher temperatures tended to form hexagonal crystallites with a diameter of 0.3 microns. Sundaram and Kahn explain the effect of substrate temperature on deposition rate in terms of adatom mobility.²⁶ An adatom is a particle that moves over the growing surface of a film under the influence of the intermolecular potential until it finds a binding site to sufficiently lower its energy. Cool surfaces have low adatom mobility and result in low density, porous, rough crystalline structures. At higher temperatures, adatom mobility is increased and results in re-evaporation of poorly aligned structures that have not achieved the lowest energy configuration within the growing crystalline lattice. This results in a higher quality film

because only those adatoms that fit “perfectly” into the appropriate lattice site will lower their energy enough to stick. This process also explains why higher deposition temperature results in a decrease in deposition rate. RF magnetron sputtering of a ZnO target at 50 °C shows a deposition rate of 15 nm/min that decreases linearly to 5 nm/min at 250 °C before changing to asymptotic behavior. The researchers also show that the resistivity of the films increases with an increase in substrate temperature. Supposedly, better crystals will have fewer grain boundaries and hence less conductive pathways. Yet another paper from I. Ohkubo et al. reports improvement in the crystallinity and PL spectra of laser MBE ZnO deposited on sapphire with an increase in deposition temperature.²⁷ The FWHM of the film deposited at 835 °C is 14 arcseconds indicating excellent crystal quality. The PL spectrum at the same temperature is extremely narrow and centered at 3.36 eV. This narrow PL profile shows a lack of defect states that might evidence themselves as broadening of the central peak or even peaks shifted to lower energies.

2.1.5 Oxygen Partial Pressure

Oxygen partial pressure during deposition has been shown to affect deposition rate, crystallinity, and resistivity. Sundaram and Kahn²⁶ report an increase of 2 orders of magnitude for the resistivity of an RF magnetron sputtered ZnO film when the percentage of Oxygen in the sputtering ambient is increased from 15 to 30%. An RF sputtering experiment by Yoshino et al.²⁸ investigating ZnO epilayers for Surface Acoustical Wave (SAW) devices reports an exponential decrease in deposition rate from 0.5 to 0.2 nm/s as the oxygen concentration in the sputtering gas varies from 0 to 100% (sputtering pressure = 0.13 Pa). Lee et al. show a similar trend with slightly lower deposition rates.²⁹ The

study reveals a sharp decrease in deposition rate as the oxygen content in the sputtering gas is increased from 0 to 10% with a linear decrease up to 70% for four different substrates. Finally, Barker et al. explain the importance of oxidizing Zn atoms before they reach the adatom surface for good crystalline growth at room temperature.³⁰ If free Zn atoms reach the substrate, they tend to site interstitially in the lattice resulting in deformation and introduction of a shallow donor defect state.

2.2 Sapphire/Zinc Oxide Lattice Mismatch

2.2.1 Sapphire Properties

Sapphire is the second hardest material known to man behind diamond. Crystals of this material exhibit hexagonal corundum structure (Pearson $D5_1$) depicted in figures 5a and 5b.

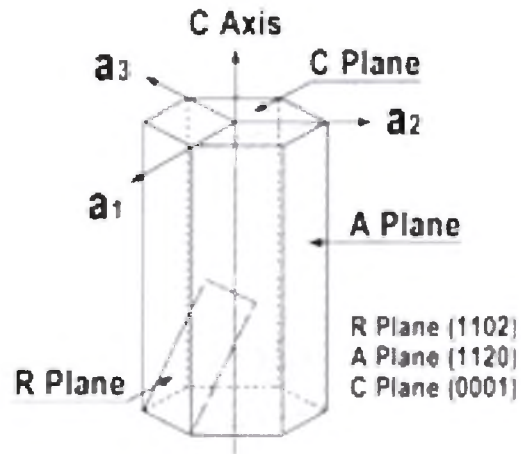


Figure 5a: Sapphire Hexagonal Crystal³¹

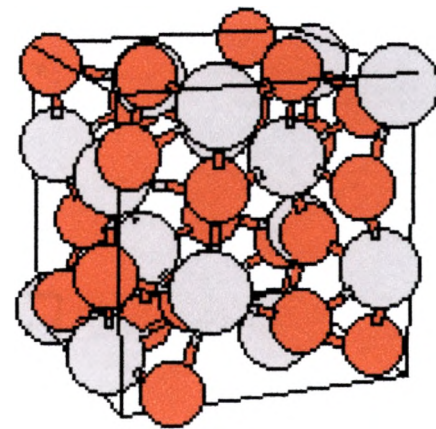


Figure 5b: Corundum Structure²²

It's physical, chemical and optical properties make it robust in terms of temperature, pressure and radiation. Some of the more important properties are listed in table 3.

Physical Properties	
Chemical Formula	Al ₂ O ₃
Structure	hexagonal-rhombohedral
Molecular weight	101.96
Lattice Constants Å	a=4.765, c=13.000
Density (g/cm ³)	3.98
Band Gap	9.9 eV (125nm)
Hardness	9 Mohs
Young Modulus (Gpa)	379 at 30° to C-axis, 352 at 45° to C-axis 345 at 60° to C-axis, 386 at 75° to C-axis
Shear Modulus (Gpa)	145
Bulk Modulus (Gpa)	240
Bending Modulus/ Modulus of Rupture (MPa)	350 to 690
Tensile strength (MPa)	400 at 25°C, 275 at 500°C, 345 at 1000°C
Elastic Coefficients	C ₁₁ =496, C ₁₂ =164, C ₁₃ =115, C ₃₃ =498, C ₄₄ =148
Apparent Elastic Limit (MPa)	448 to 689
Flexural Strength (GPa)	2.5 - 4.0
Poisson ratio	0.25 - 0.30
Thermal Properties	
Melting Point (°C)	2040
Maximum use temperature (°C)	1800
Specific Heat J/(kg × K)	105 at 91 K 761 at 291 K
Thermal coefficient of linear expansion at 323 K (K-1)	6.66 × 10 ⁻⁶ parallel to optical axis 5 × 10 ⁻⁶ perpendicular to optical axis
Thermal conductivity (W/m °K) at 20° C	41.9
Thermal Expansion (20 - 1000°C)	Parallel to C-axis: 9.03 × 10 ⁻⁶ °C Perpendicular to C-axis: 8.31 × 10 ⁻⁶ °C 60° to C-axis: 8.4 × 10 ⁻⁶ °C

Table 3: Physical and Chemical Properties of Sapphire³¹

2.2.2 Plane Alignment

The nominal lattice mismatch between sapphire and ZnO is approximately 32%. This mismatch is reduced to 18% when the planes of ZnO undergo a rotation to reduce stress and lower the energy of the ZnO/sapphire interface. Chen et al. were among the first to investigate the plane orientations of ZnO on sapphire.⁸ The authors report an alignment of the ZnO $[2\bar{1}\bar{1}0]$ with the Al_2O_3 $[1\bar{1}00]$ and the ZnO $[1\bar{1}00]$ with Al_2O_3 $[1\bar{2}10]$. This indicates a 30 degree rotation of the ZnO epitaxial layer with respect to the sapphire substrate as depicted in figure 6.

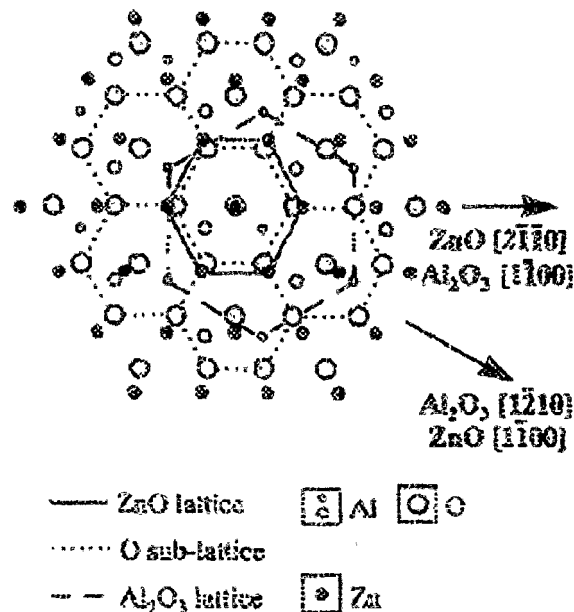


Figure 6: Oxygen Sublattice Alignment at Sapphire/ZnO Interface⁸

The ZnO aligns itself with the oxygen sublattice of the sapphire in order to reduce the lattice mismatch. This need for an oxygen template validates the importance of oxygen radical treatment of the substrate prior to deposition. Another report detailing a 30 degree ZnO rotation from Narayan et al. cites a different set of aligned planes but

similarly concludes that domain matching epitaxy controls the epitaxial growth of ZnO on sapphire.³² Transmission Electron Microscope (TEM) micrographs published by Vigue et al.¹⁸ also reveal the epitaxial relationship between PEMBE ZnO and sapphire at the interface as depicted in figure 7.

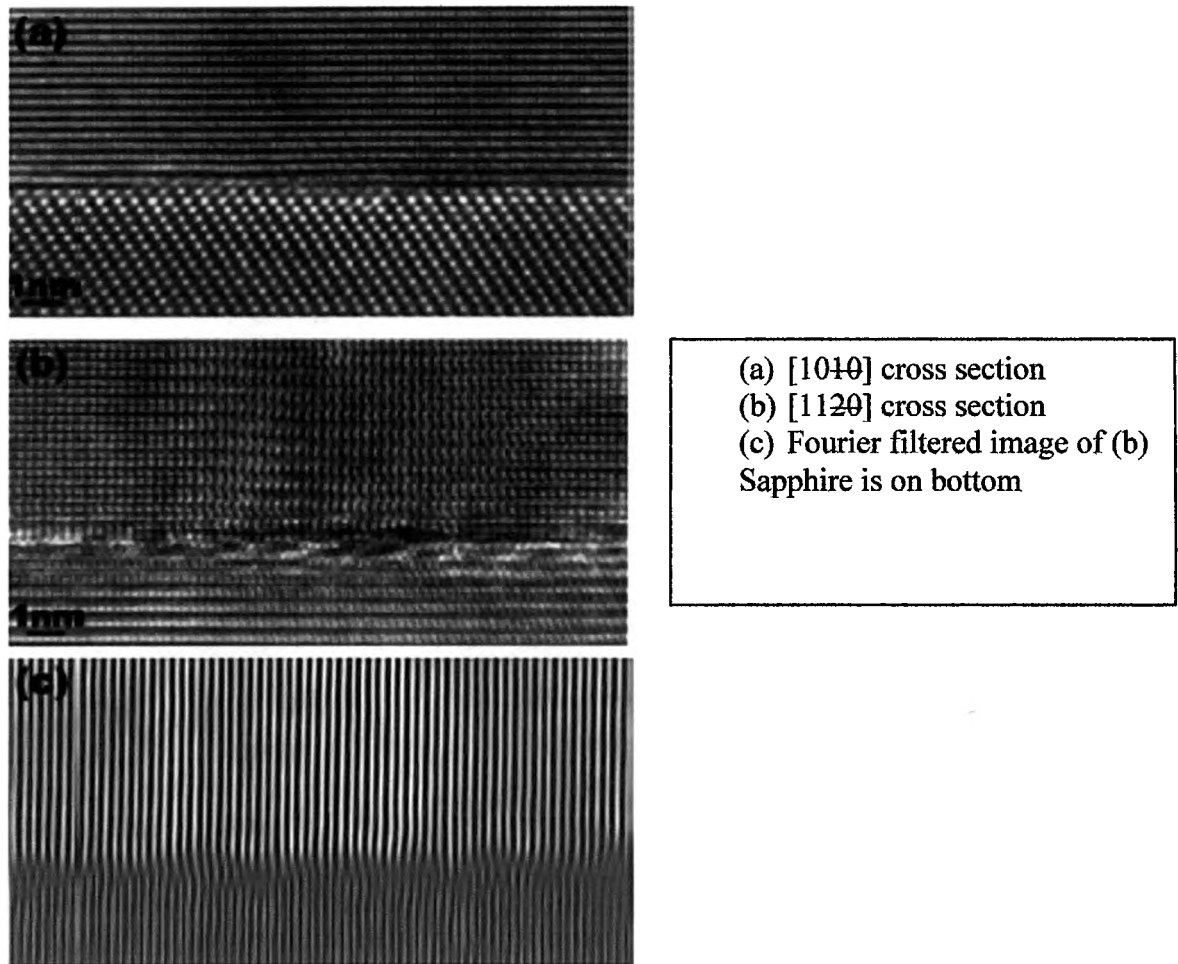
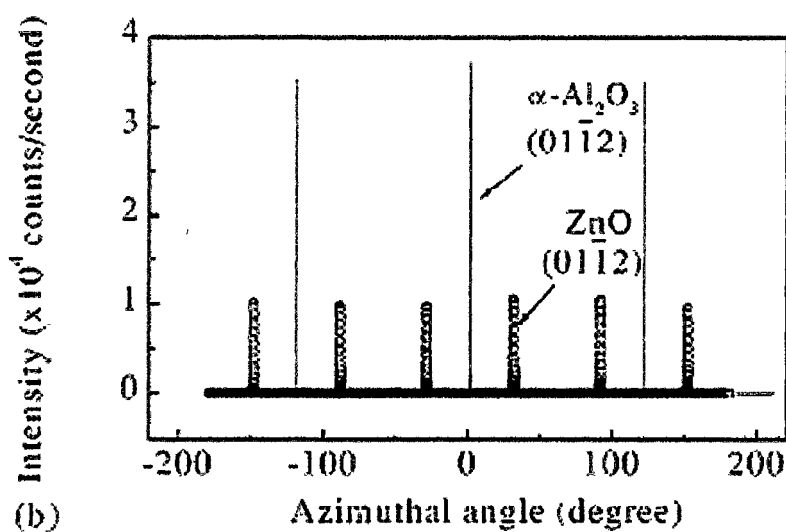


Figure 7: TEM Images¹⁸ of ZnO on Al₂O₃

Once again, the lack of disorder at the interface stresses the importance of the oxygen plasma treatment employed by these researchers and others. Ohkubo et al.³³ report

differing plane orientations for ZnO on sapphire at deposition temperatures of 400-450 °C and 800-835 °C. The authors conclude that the most thermodynamically stable orientation occurs when the hexagonal-closest-packed (hcp) oxygen sublattices in the substrate and film align. This situation results in an 18% lattice mismatch between ZnO and Al₂O₃. At the lower temperatures, an alternate plane orientation results in a 31.8% mismatch. Films deposited at both low and high temperatures are c-axis aligned, with higher temperatures and lower deposition rates primarily producing the most stable configuration. The authors also confirm that the best lattice match occurs when ZnO encounters an oxygen terminated sapphire surface and report a FWHM for ZnO (0002) of 14.4 arcseconds for a film grown at 835 °C. The plane alignment of ZnO films grown by RF magnetron sputtering was reported by Kim et al. using a graphical representation that our group found very appealing.³⁴ The epitaxial nature of the ZnO film as well as the symmetry of the planes is clearly evident in the XRD phi scan depicted in figure 8.



Our group was able to reproduce the phi scan example shown here for the planes in question.

Figure 8: Phi scan of the (0112) planes for ZnO and Sapphire³⁴

It is worth noting that Fons et al. have published a report advocating the use of a-plane sapphire as a substrate³⁵ for ZnO as well as other wide band gap semiconductors including GaN and SiC. The more widely used c-sapphire consists of alternating layers of 3-fold symmetric Al atoms and 6-fold symmetric O atoms along the c-axis. ZnO wurtzite structure is 6-fold symmetric for both Zn and O along the c-axis. This requires the aforementioned rotation of ZnO planes to match the sapphire O layer. The authors propose that this orientation may be metastable. They go on to claim that the a-axis of ZnO and the c-axis of sapphire are related by a factor of 4 resulting in a lattice mismatch of <1% if you can coerce the film to grow along the (0001) direction of a-sapphire as depicted in figure 9.

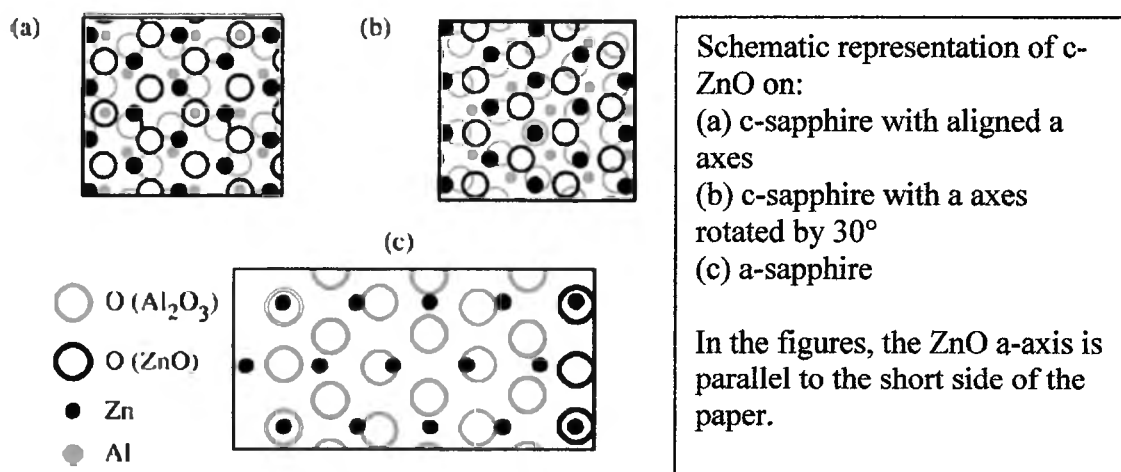


Figure 9: a-Sapphire as an Alternate Substrate Material³⁵

2.2.3 Growth Evolution

The deposition of ZnO undergoes an evolution from 2D to 3D growth on a timescale dependent upon the substrate temperature. Chen et al. used RHEED to monitor the growth of ZnO and discovered that it differed from the Stranski-Krastanow (SK)

mode.⁸ SK mode begins with 2D monolayer growth steadily building up strain. Upon reaching a critical thickness, the epilayer will relax and transition to 3D defect free island growth. As previously stated, the 18% mismatch between ZnO and sapphire makes the initial SK 2D layer by layer growth nearly impossible. The authors suggest that 2D islands with incoherent boundaries build up initially and act as nucleation cores for 3D islands. Their Reflective High Energy Electron Diffraction (RHEED) analysis clearly establish that the critical film thickness for the 2D-3D transition increases with higher growth temperatures as shown in figure 10.

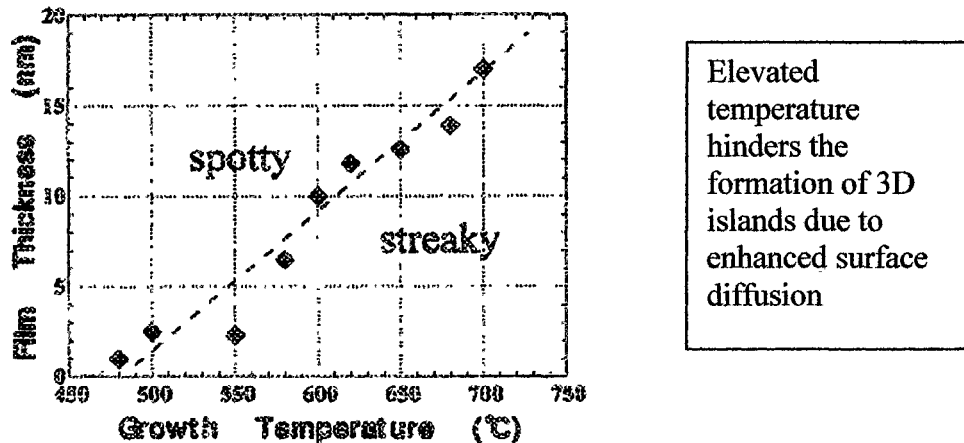


Figure 10: RHEED Pattern Transition as a Function of Temperature⁸

Another study of the ZnO 2D-3D growth mode by Vigue et al. reports the same trend of large diffuse RHEED lines (2D) to small intense points (3D) after 15 min at 0.5 microns/min growth rate.³⁶ The researchers include some fantastic TEM micrographs of 3D and 2D ZnO layers as shown in figure 11.

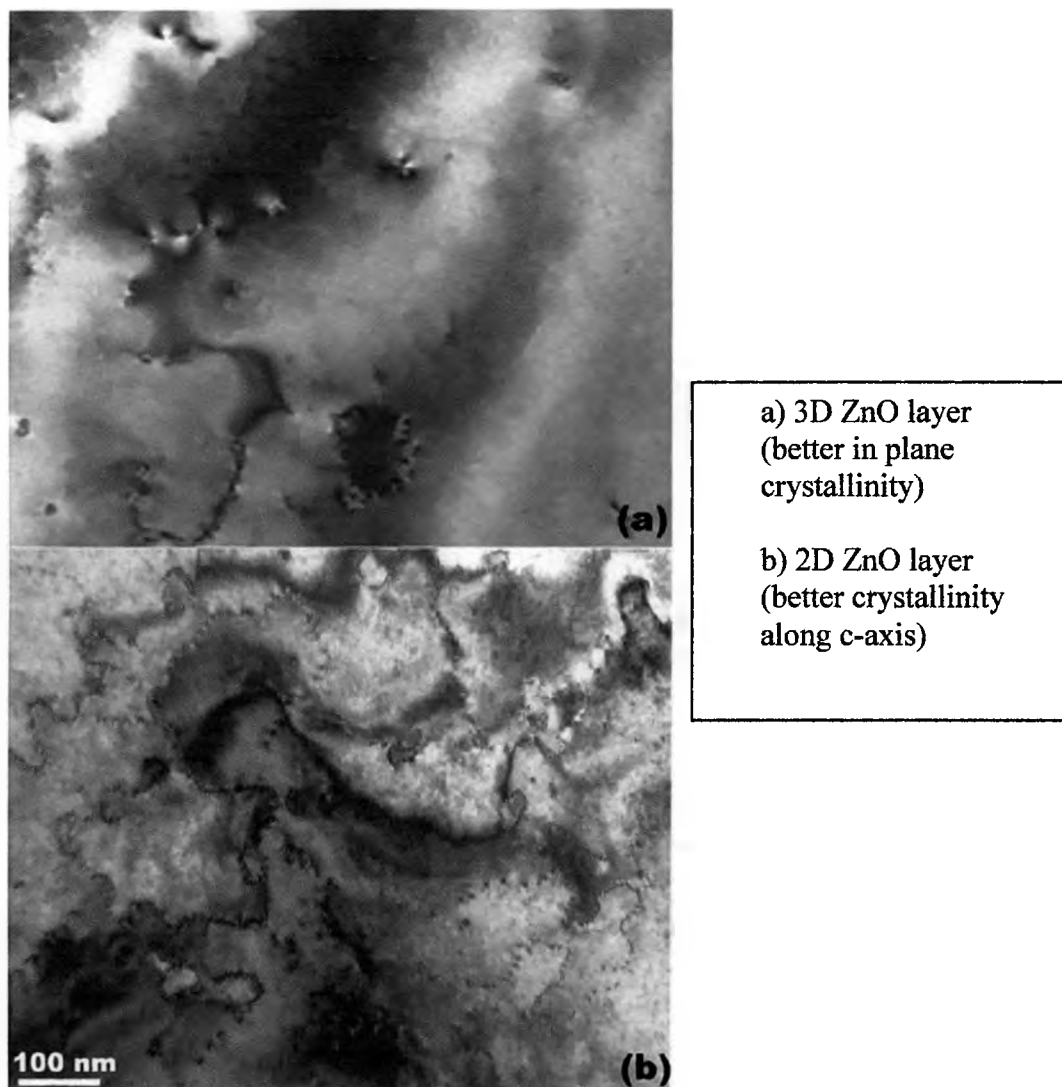


Figure 11: TEM Micrographs of 2D and 3D ZnO Layers³⁶

The authors proceed to evaluate the two types of layers with high resolution x-ray diffraction (HRXRD) to conclude that the structural quality of layers fabricated during the 3D growth mode parallel to the substrate (c-axis) is reduced while in plane crystal quality is increased compared to 2D growth mode ZnO. Another contribution to this topic comes from a paper by Park et al. where an x-ray synchrotron was used to monitor ZnO growth in real time.³⁷ The initial 2D growth mode is characterized by ZnO layers that are well aligned to the substrate but highly strained while the 3D layers are poorly

aligned and relaxed. The omega rocking curve of the ZnO (002) peak evolves as the thickness increases to a broad component superimposed on a sharp central peak. The onset seems to occur for film thickness greater than 80 angstroms as shown in figure 12.

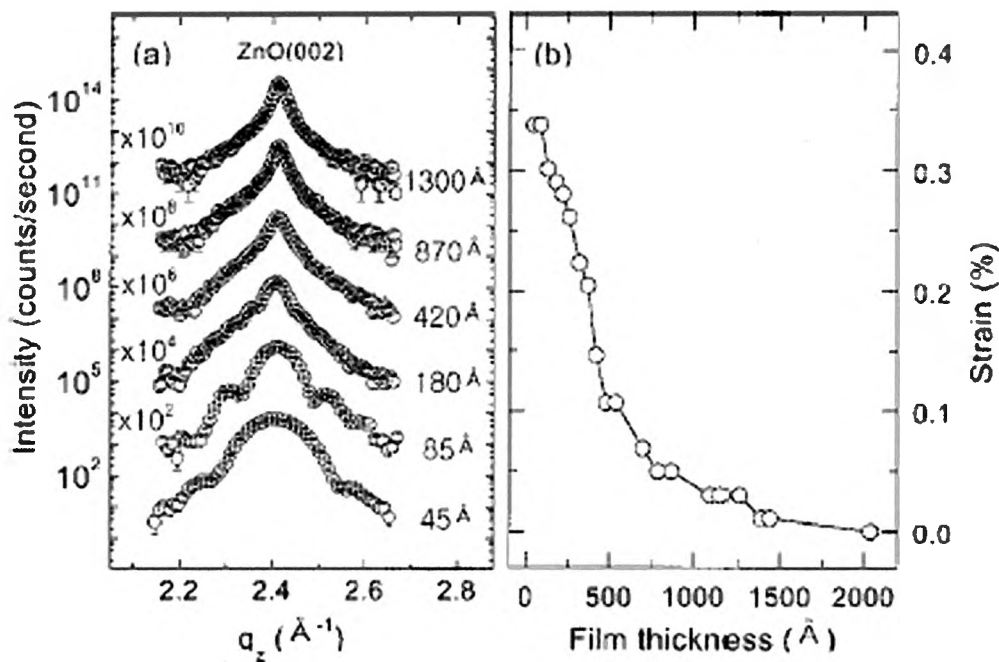


Figure 12: Evolution of ZnO (002) Rocking Curve vs. Film Thickness³⁷

When the film thickness reaches 180 angstroms, the 3D islands come into contact with one another and begin to form hexagonal columnar grains as confirmed by the Atomic Force Microscopy (AFM) images shown in figure 13.

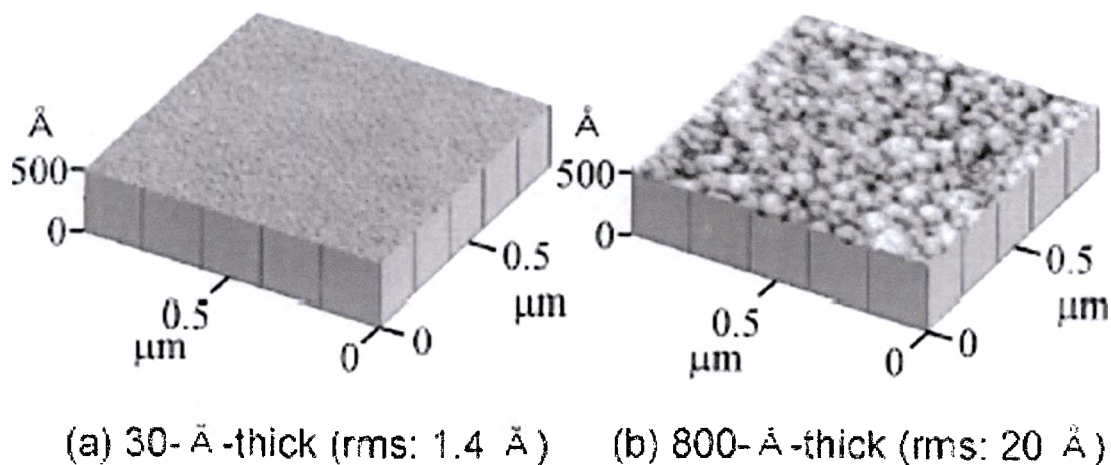


Figure 13: AFM images of 2D and 3D ZnO layers³⁷

It would seem that after the ZnO epilayer reaches a critical thickness, the presence of hexagonal columns should be accompanied by an increase in surface roughness. The final study included for this topic conducted by J-M. Myoung et al has examined the effect of film thickness on surface morphology.³⁸ This group proposes the same trend of 2D-3D growth mode, but the transition region is quite different compared to the previous studies. They claim that the onset of rough 3D island type growth occurs between 400 and 1700 angstroms as evidenced by SEM micrographs shown in figure 14.

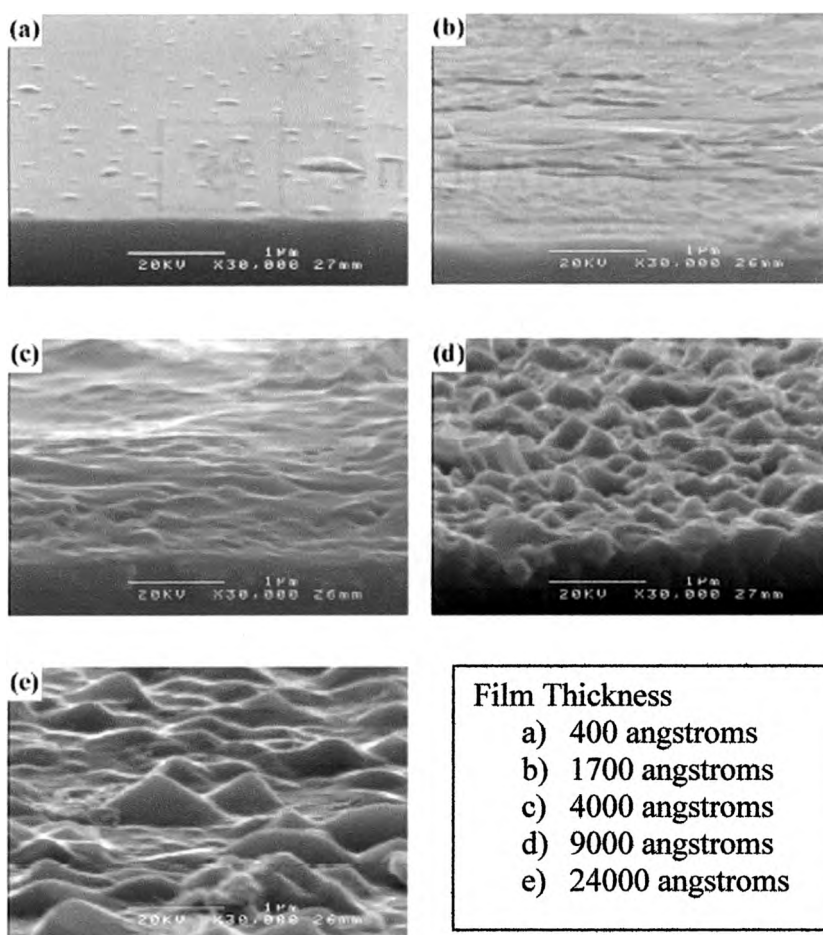


Figure 14: SEM Micrographs for PLD ZnO Films of Increasing Thickness³⁸

These films were deposited on sapphire by PLD at a deposition temperature of 400 °C. With this study in mind, it is entirely possible that our films may not transition to 3D growth mode due to thickness limitations and higher deposition temperatures. The authors also claim that the FWHM of the ZnO (002) rocking curve decreases with increasing film thickness, an indication of relaxation in the film and improved crystallinity.

2.2.4 Buffer Layers

In an attempt to mitigate the effects of the large mismatch between ZnO and sapphire, many researchers have attempted to introduce both homoepitaxial and heteroepitaxial buffer layers.

2.2.4.1 Homoepitaxial Buffer Layers

Yamauchi et al. report growing an initial ZnO layer $< 1/4$ of the total film thickness at $1/10^{\text{th}}$ the deposition rate results in improvements in PL spectra, orientation, and surface morphology.³⁹ An alternate approach was undertaken by Nakamura et al. whereby the homoepitaxial buffer layer was grown at lower temperature (LT).⁴⁰ The ZnO LT-buffer was grown at 500°C for 10 min with an additional layer deposited at 700°C for 55min. This optimized condition produces a 50nm LT buffer layer and decreases the FWHM of the ZnO rocking curve from 0.265 deg to 0.089 deg. We should also note that films without the buffer layer show hexagonal grains with a cell size of $\sim 300\text{nm}$ similar to earlier reports of hexagonal structures at the surface. The last paper detailing the use of a low temperature ZnO homoepitaxial buffer layer comes from Vigue et al.³⁶ A 20-50 nm buffer was deposited at 350°C and then annealed at 650°C before proceeding with the subsequent layer. However, the introduction of this buffer layer maintains a 2D growth mode throughout deposition and thus results in a film with less structural quality along the c-axis compared to a film grown in 3D mode. A paper from M. Joseph et al. proposes an alternate two step growth for PLD deposited ZnO suggesting that the use of a high temperature buffer layer is the key to improving crystal quality.⁴¹ The researchers deposit 5-10 nm on ZnO between $600\text{-}700^{\circ}\text{C}$ followed by a deposition at less than 400°C of a layer thicker than 200nm. The authors claim an improvement in

crystal quality but succeed only in showing that the PL spectra of the two step film just described and a one step film deposited at 700 °C are similar without investigating the crystallinity via XRD, AFM or TEM. A final theory concerning homoepitaxial ZnO buffer layers comes from Y. Chen et al. who suggest that the nature of the ZnO/sapphire interface automatically introduces a buffer layer that has a high defect density as observed by TEM measurements but relatively smooth morphology as evidenced by RHEED measurements during growth.⁸ Refining the thickness, deposition temperature, and deposition rate of the homoepitaxial buffer layer is required to improve the efficiency of ZnO epilayer growth on sapphire.

2.2.4.2 Heteroepitaxial Buffer Layers

Gerthsen et al report on a heteroepitaxial GaN buffer on sapphire grown by MOCVD[40]. The 2 micron buffer was deposited at 380 °C in an attempt to make use of the relatively low 1.9% mismatch between GaN and ZnO. The subsequent ZnO layer is riddled with stacking faults as opposed to the normally high density of threading dislocations found in ZnO on sapphire. Several papers have reported on the use of an extremely thin MgO buffer layer.^{16, 43-44} The general technique involves the deposition of a few nm of MgO, low temperature deposition of ZnO until the RHEED patterns transition to streaks, 5 min 700 °C anneal, and subsequent deposition of the ZnO epilayers at 650 °C. The RHEED patterns during deposition are depicted in figure 15.

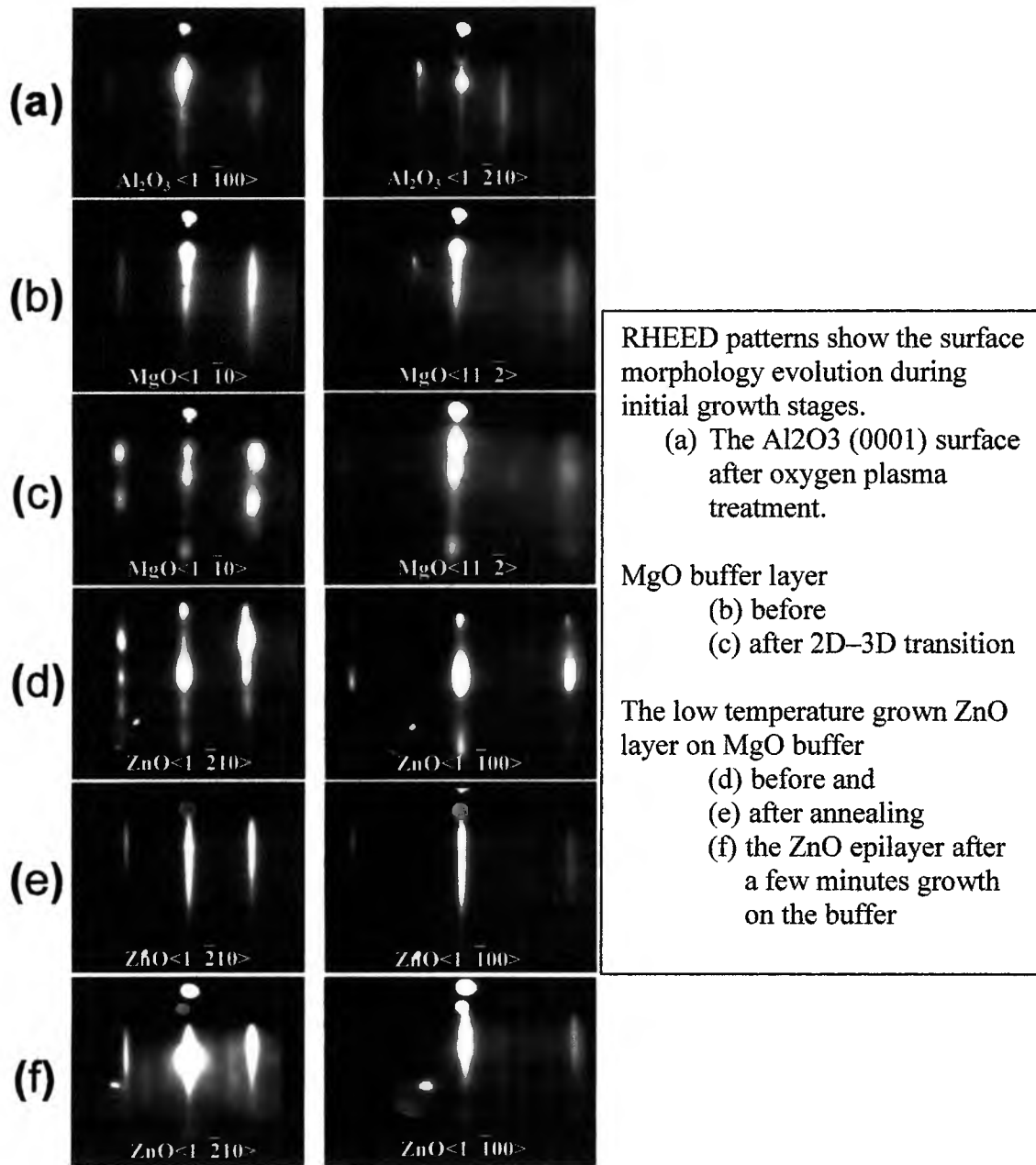


Figure 15: RHEED Pattern Evolution for ZnO on Sapphire with a MgO buffer¹⁶

Y. Chen et al. claim that the MgO layer creates favorable nucleation sites for the wetting of a ZnO overlayer. In a follow up paper by the same group, they detail the plane alignment using a reciprocal space map as shown in figure 16.

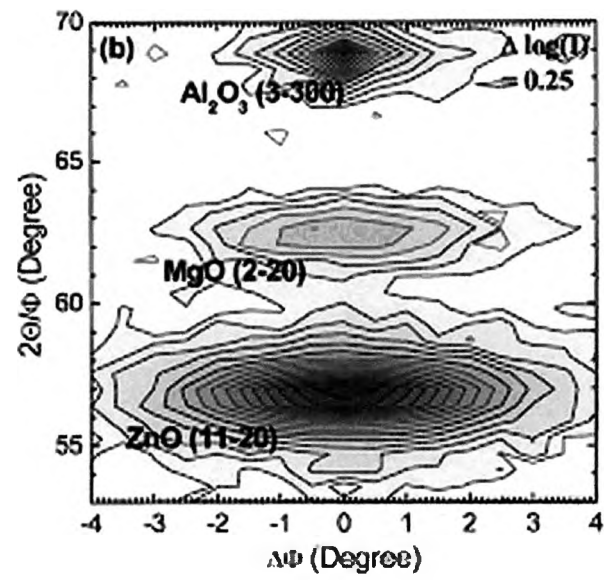


Figure 16: Reciprocal Space Map for Sapphire, MgO buffer, and ZnO epilayer⁴³

2.3 Carriers in Zinc Oxide

2.3.1 Doping Asymmetry

The most significant barrier to widespread application of Zinc Oxide based materials is an inherent doping asymmetry. Gerthsen et al.⁴² report unintentional (intrinsic) n-type conduction with a carrier density of 10^{16} - 10^{18} . Extrinsic n-type conductivity is easily realized through the use of group 3 dopant atoms such as Al or Ga while p-type conductivity is rather difficult to achieve. Other wide band gap semiconductors such as GaN and ZnSe show a similar difficulty in creating p-type material while the opposite is true for ZnTe. This doping anisotropy has been attributed to the presence of Hydrogen as well as native defects in ZnO.

2.3.2 Hydrogen in ZnO

Chris Van de Walle published a paper that explains the role of H as a shallow donor and thus a source of conductivity in ZnO.⁴⁵ Hydrogen typically acts as an amphoteric impurity, that is, in p-type material it acts as a donor by incorporating as H^+ while in n-type material, H^- acts as an acceptor. This behavior explains why the presence of hydrogen always counteracts the conductivity of the material. Surprisingly, H in ZnO occurs exclusively in the positive charge state and the low formation energy of H^+ allows for a large solubility. The researchers determined the possible exchange sites and determined their relative stability within the host lattice as depicted in figure 17.

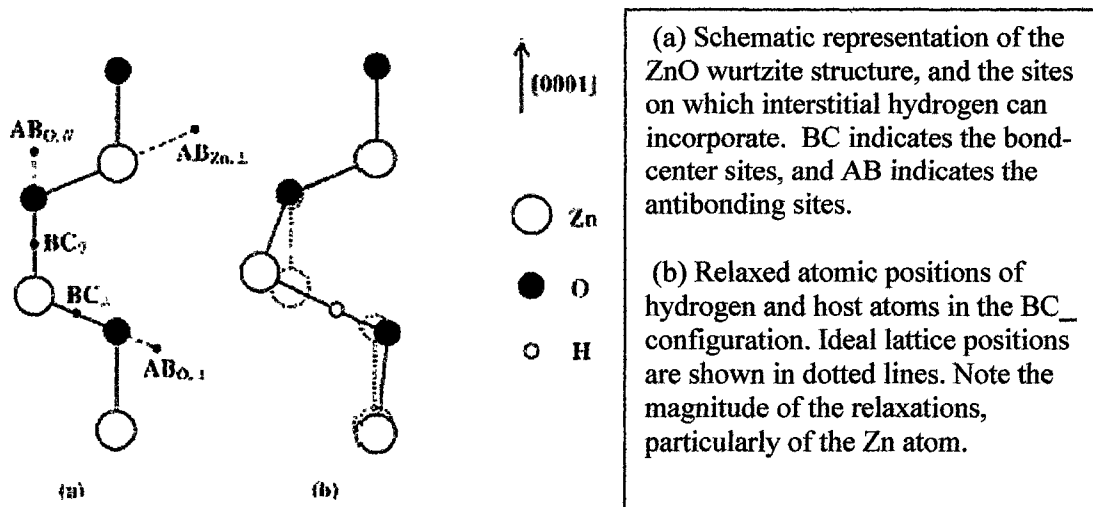


Figure 17: Hydrogen Incorporation into the ZnO Wurtzite Structure⁴⁵

N. Nickel and K. Fleicher have experimentally verified Van de Walle's predictions of high hydrogen solubility by studying vibrational modes of ZnO.⁴⁶ The scientists employed Raman backscattering spectroscopy to observe six local vibrational modes between 2800 and 3150 cm^{-1} related to the presence of H in undoped ZnO. The spectra of the ZnO sample is shown in figure 18.

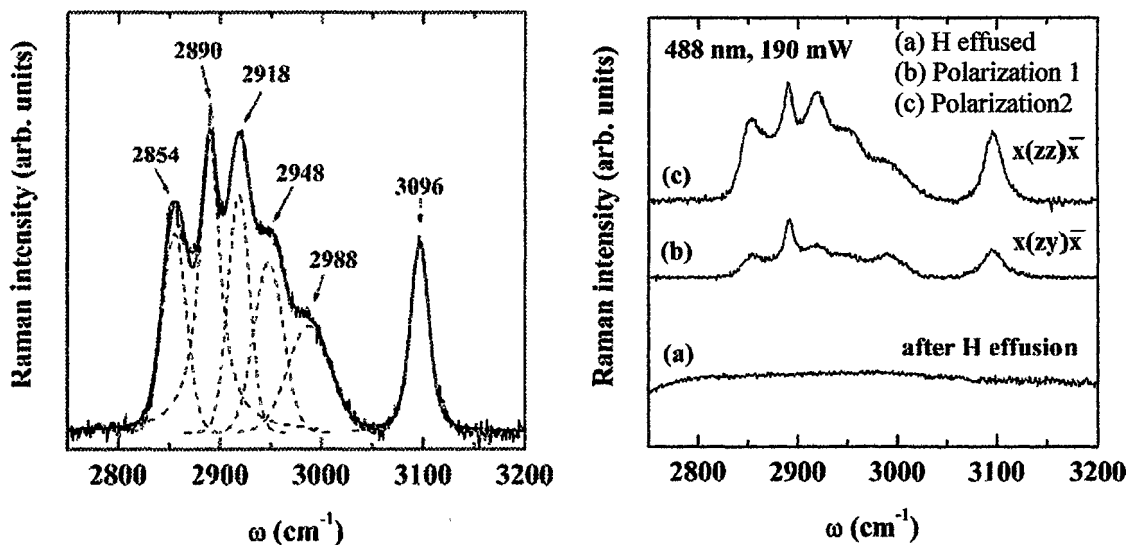


Figure 18: Raman Spectra Showing 6 Hydrogen Related Stretching Modes⁴⁶

After the researchers heated the samples up to 950 °C (to drive out the Hydrogen) the peaks disappeared. Van de Walle's predictions regarding H donors were verified by Hofmann et al. who studied nominally undoped ZnO single crystals.⁴⁷ Electron Paramagnetic Resonance (EPR) and electron nuclear double resonance (ENDOR) spectroscopy revealed the presence of a donor state related to the presence of Hydrogen. This state's thermal activation energy is 35 meV, it interacts with ~50 shells of Zn nuclei, has a Bohr radius of 1.5nm, and is present in a concentration of $6 \cdot 10^{16} \text{ cm}^{-3}$ in commercially available ZnO single crystals. The ZnO films discussed above were grown without the presence of H as a process gas but H is an extremely difficult contaminant to control (and detect for that matter) so it makes its way into the films anyway. Finally, we should make some remark about Hydrogen at the surface of ZnO. M. Kunat et al concluded that exposure to molecular and atomic Hydrogen leads to the formation of an overlayer at the surface of ZnO.⁴⁸ This study used He atom scattering to reveal the nature of the hydrogen at the surface in an attempt to overcome complications due to the low electron/x-ray photon cross section of H and the low reflectivity of the ZnO surface in the infrared. The authors contradict recently published work to show that the O-terminated ZnO surface is actually H-saturated. Further XPS studies must be undertaken to verify the prediction of an ordered array of oxygen vacancies.

2.3.3 Native Defects

Zhang et al. investigated the native defects in ZnO including Zinc interstitials (Zn_i), Zinc vacancies (V_{Zn}), Oxygen interstitials (O_i), Oxygen vacancies (V_{O}) and Zinc – Oxygen anti-sites (Zn_{O}) in an attempt to explain the intrinsic doping asymmetry.⁴⁹ The researchers showed that Zn_i is a shallow donor whose abundance is relatively large due to

a low enthalpy of formation for both O rich and Zn rich films. Hence, Zn rich films are inherently n-type because O_i and V_{Zn} , the only native defects capable of compensating Zn_i , are relatively rare due to a high enthalpy of formation. The authors also conclude that intrinsic p-type doping is impossible. For both Zn-rich and O-rich conditions, Zn_i , V_O and Zn_O , designated “hole killers”, all have low enthalpy of formation. Finally, the investigators attribute the green luminescence commonly observed in ZnO films to the oxygen vacancy defect and go on to claim that multiple hole capture by one of these defect centers leads to structural relaxation accompanied by electron hole recombination to explain the slow decay of photoconductivity in ZnO films.

2.3.4 N-type Doping

Oxygen deficiencies and interstitial Zn ions both act as donors and typically render ZnO an n-type conductor. Enhancement of this conductivity can be achieved with various dopant ions. Aluminum has been the element most widely used to dope ZnO. M. J Jayaraj et al. set out to produce transparent conducting films of aluminum doped ZnO via RF magnetron sputtering while optimizing substrate temperature, gas pressure, substrate to target distance, and substrate orientation.⁵⁰ The authors found that resistivity increased dramatically when oxygen was present in the sputtering gas which implies that conducting films require metal rich stoichiometries. The conductivity of the samples increased with increasing substrate temperature to a maximum at 423K as shown in figure 19

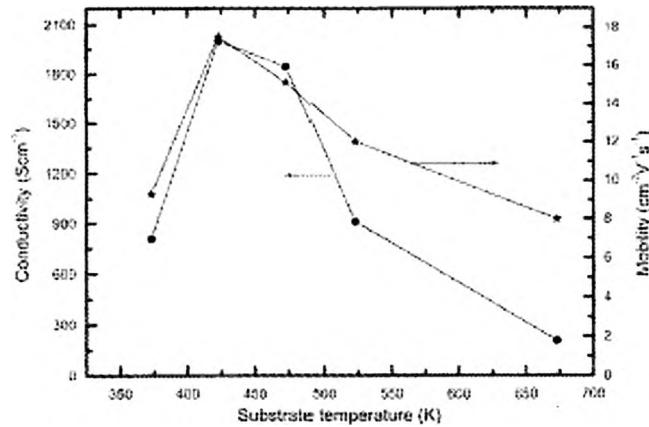


Figure 19: Conductivity and Mobility⁵⁰ vs. Deposition Temperature for Al:ZnO

Dopant concentration matched that present in the target and AFM revealed similar morphology for varying temperature, hence these parameters were found to be independent of substrate temperature. Once grown, the samples seem to show resistivity only slightly dependent upon temperature suggesting that the ZnO:Al films have high carrier concentrations in the conduction band even at room temperature. X-ray diffraction data shows that the c-axis orientation of the grains is both uniform and perpendicular to the substrate surface. Transmission >85% was achieved for all Al:ZnO regardless of dopant concentration while the optical band gap shifted with increasing carrier concentration shown in figure 20 in accordance with the Burstein-Moss effect .

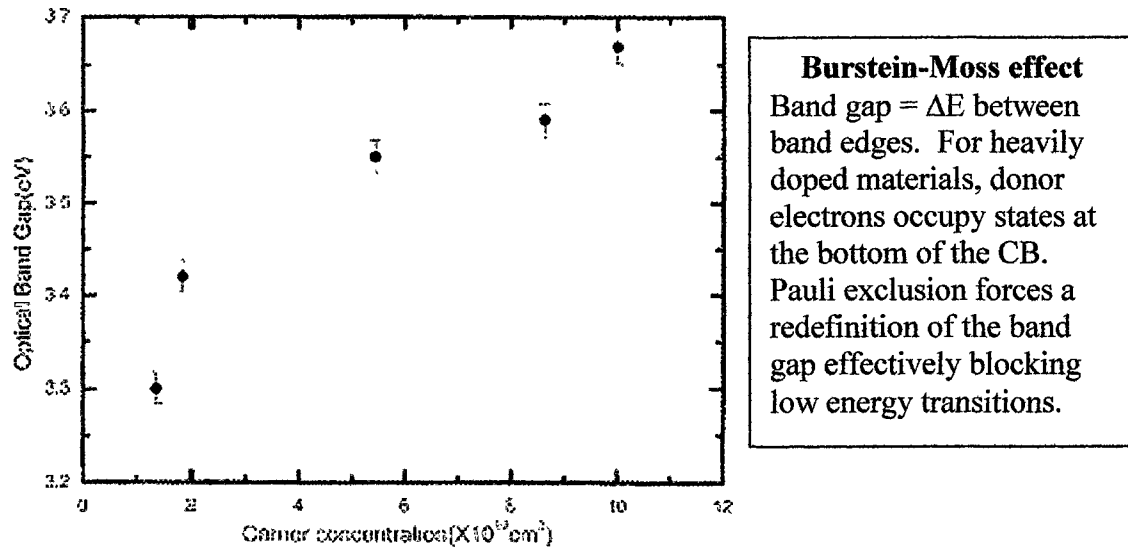


Figure 20: Band Gap Shift Due to Increasing Carrier Concentration⁵⁰

There are many other dopant ions available to modify the electrical characteristics of ZnO films. Table 4 shows the characteristics of several films grown by different methods.

Film Material	Deposition Technique	Deposition Temperature ($^{\circ}\text{C}$)	Resistivity ($\times 10^{-4} \Omega \cdot \text{cm}$)	Carrier Concentration ($\times 10^{20} \text{ cm}^{-3}$)	Hall Mobility ($\text{cm}^2 \text{ V}^{-1} \text{ s}^{-1}$)
ZnO	PLD	RT	20-30	-	-
ZnO:Al	PLD	300	9	5.8	12
ZnO:Al	PLD	300	1.4	15	30
ZnO:Ga	PLD	200	2.1	1	10
ZnO:Ga	PLD	300	3.6	8.7	18
ZnO	RFMS	90	5	1	120
ZnO	RFMS	-	4.6	5	27
ZnO	DCMS	-	40	-	-
ZnO:Al	DCMS	RT	7.7	4.2	19.5
ZnO:Al	DCRMS	300	4.2	2.6	57
ZnO:Al	ACRMS	300	4	4.9	32
ZnO	Spray	450	20	-	-
ZnO:Al	Spray	425	35	0.2	60
ZnO:In	Spray	375	8	4	16
ZnO:F	Spray	700	6.8	-	-
ZnO:Al	DCRMS	250	1.9	11	30
ZnO:Al	RFMS	RT	6.5	6.5	15
ZnO:Al	RFMS	90	1.9	15	22
ZnO:B	RFMS	90	6.4	2.5	39
ZnO:In	RFMS	90	8.1	4	20
ZnO:Ga	RFMS	90	5.1	2.5	39
ZnO:Al	MOCVD	420	3	8.8	23
ZnO:Al	CVD	350	71	-	-
ZnO:B	CVD-ALD	150	5.3	-	-
ZnO:Al	Sol-gel	450	7	6	10
ZnO:Al	Electroless	225	2.1	1.8	17

Table 4: ZnO Doping Through Various Techniques⁵¹

2.4 P-type Zinc Oxide

2.4.1 Nitrogen Doping

Due to the successful fabrication of low resistance p-type ZnSe via doping with Nitrogen and the prediction by first principles calculations that it will produce a shallow donor level in ZnO, many researchers have investigated the possibility of using N doping to achieve p-type ZnO. There have been contrasting reports in the literature regarding the success of such attempts. In general, the doping limit for any impurity is caused by compensation from undesirable defects, solubility, and ionization rate. Yan et al. have compiled a report detailing these factors that influence Nitrogen incorporation into ZnO films.⁵² The authors show that acceptor states produced when N occupies an O site are always compensated by oxygen vacancies. This N_O defect has a large enthalpy of formation and thus a low solubility in ZnO. Its room temperature ionization energy is estimated to be 10^{-4} so that even high concentrations of N_O will be reduced by a factor of 4. The researchers also propose solutions including H-assisted doping and molecular doping. The former introduces an interim defect (NH_O) with a lower formation enthalpy followed by annealing at high temperatures to remove the H resulting in a non-equilibrium concentration of N_O . They propose using NH_3 as a carrier gas but do not address to what extent the annealing process reduces the hydrogen concentration or activates other donor and acceptor states. Molecular doping with NO or NO_2 is touted as the most efficient route to p-type ZnO. The use of these particular species (as opposed to N_2O for example) reduces the probability of introducing the undesirable defect $(N_2)_O$, a shallow double donor, due to unfavorable reaction kinetics at the epilayer surface. In

order to better understand the specific defect states discussed above, we should examine several figures⁵³ from E-C. Lee et al. in figures 21-24.

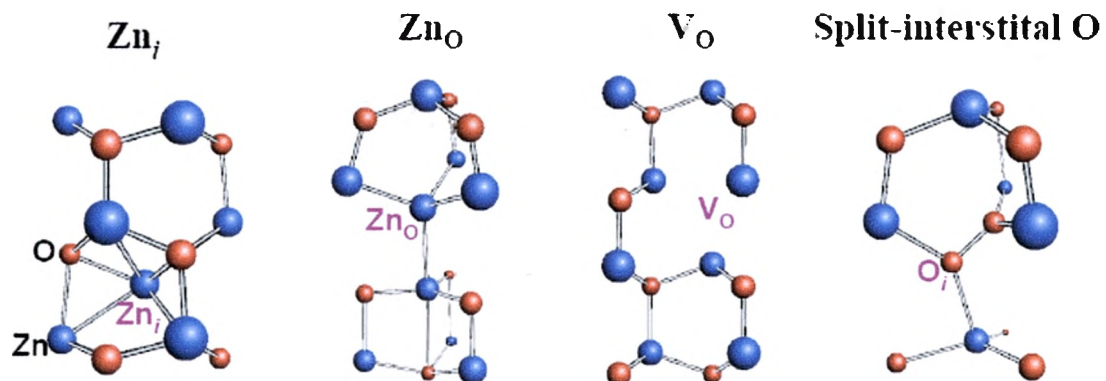


Figure 21: Native Donor Defects⁵³ in ZnO

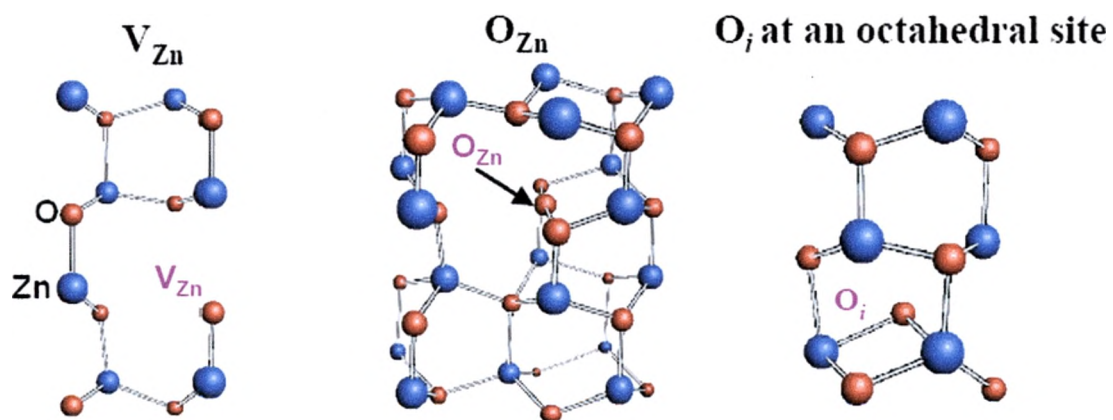


Figure 22: Native Acceptor Defects⁵³ in ZnO

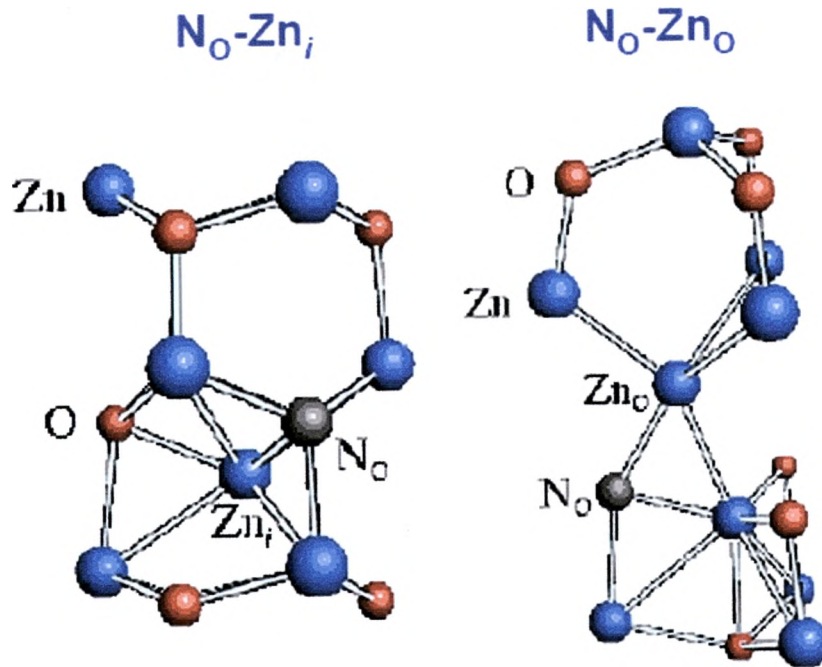


Figure 23: Nitrogen-Native acceptor Complexes⁵³

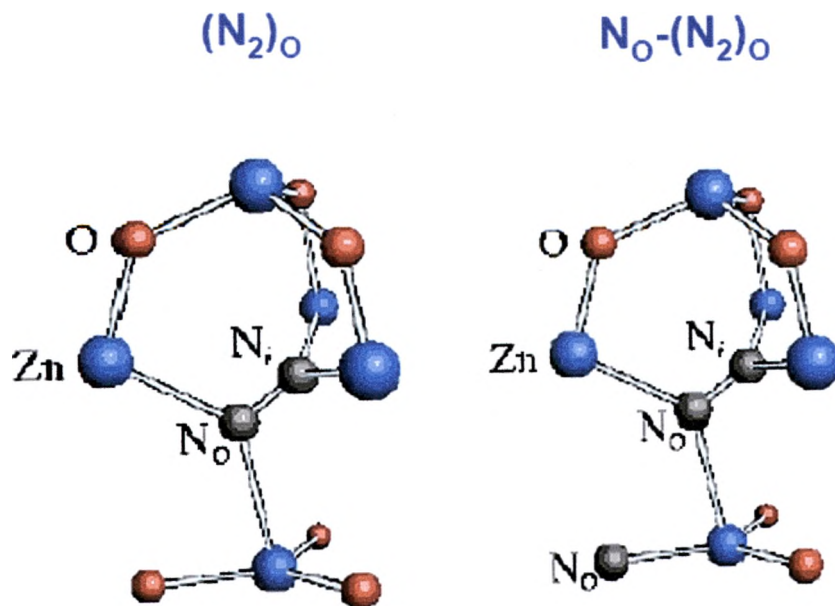


Figure 24: Nitrogen-Based Double and Single Shallow Donor Defects⁵³

Many attempts have been made using various techniques to incorporate Nitrogen as a p-type dopant into ZnO deposited on sapphire. The following accounts provide a brief survey of some unsuccessful and successful attempts. Nitrogen doping via Zn evaporation in mixed oxygen-nitrogen RF plasma was attempted by Yuichi and Susumu Sato.⁵⁴ They showed a trend of increasing resistivity and decreasing hall mobility with an increase in Nitrogen percentage of the plasma with carrier concentrations independent over the range of O:N ratios. Annealing of their samples increased the carrier concentration (electrons) by 2 orders of magnitude to 10^{20} cm^{-3} but they attribute this to dissociation of oxygen from the films rather than activation of a previously dormant donor state. For the highest percentages of N, photoluminescence was unobservable. K. Iwata et al. employ a radical source MBE technique previously used to fabricate high quality epitaxial ZnO to try and fabricate p-type material.⁵⁵ The layers were deposited on sapphire held at $350 \text{ }^{\circ}\text{C}$ while the N/O flow ratio was varied from 0.5-24%. The researchers show that higher N flow rates induce defects that manifest themselves in XRD pole figures as rotational domains and twins. They speculate that substitutional Nitrogen sites repel one another due to the large Madelung Energy (ME) contribution to the lattice (0.79eV) and therefore must be unstable. PL spectra of the N-doped samples show a broad peak near 2.2 eV with reduced emission at 3.38 eV compared to undoped samples. Additionally, carrier compensation by N resulted in a decrease in electron concentration up to 10% N with an electron concentration increase thereafter due to an increase in intrinsic donor defects. The authors were unable to produce p-type films in this manner and cite low activation rate of the N acceptor state and deep carrier traps due to N-induced defects as the reasons. Yet another method investigated by Wang et al.⁵⁶

uses plasma assisted MOCVD of ZnO on sapphire to try and realize N-doped p-type ZnO. They claim that a narrower FWHM of the ZnO (0002) 2θ peak indicates that N-doping results in better film quality. However, they do not specify the thickness of the layers which also directly influences the FWHM. Also, rocking curve analysis shows that the N-doped sample exhibits less mosaicity. Their films are all characterized as having high resistivity useful for SAWs devices, but not p-type carriers. ECR (N_2O) plasma assisted PLD was attempted⁵⁷ by Guo et al. on (1120) sapphire at $390^\circ C$ [54]. The films are c-axis oriented as expected with a smooth (5nm rms roughness) grainy surface. Unfortunately, the films have a large resistivity of 180 Ohm-cm so the authors could not confirm the conductivity or carrier type with Seebeck measurements. The final N-doping technique from Yamamuchi et al uses mixed N/O plasma assisted epitaxy.⁵⁸ Films deposited at $400^\circ C$ showed a conspicuous emission apparently due to an electron transition from donor to acceptor (DAP emission). The calculated donor and acceptor energies were 40 and 135 meV respectively. The PL spectra also indicates yellow and green band emission peaks from the oxygen interstitial and vacancy respectively while the electrical properties of the doped and undoped films were the same. They conclude that the presence of the DAP emission highlights the possibility of p-type doped ZnO provided that N can be precisely incorporated during Zn rich deposition conditions.

Mingenishi et al. reported p-type ZnO realized by CVD with NH_3 as a carrier gas.⁵⁹ The p-type film was deposited at $650^\circ C$ on a sapphire substrate, showed a resistivity of 34 Ohm-cm, Hall coefficient of $420\text{ cm}^3/C$, mobility of $12\text{ cm}^2/V*s$, and a hole concentration of $1.5*10^{16}\text{ cm}^{-3}$. Because the N_O impurity acts as a donor, the authors stress the need for Zn rich conditions during growth. However, it was discovered that N

incorporates into the film as ZnHN resulting in Hydrogen passivation which can be mitigated by a post-deposition anneal. Researches at Eagle-Picher and AFRL conducted a study of the properties of MBE homoepitaxial N-doped ZnO films.⁶⁰ The substrates were chemo-mechanically polished ZnO wafers doped with Li to facilitate Hall effect measurements without substrate interference. Deposition of a 1.9 micron thick epilayer occurred at 525⁰C with a flux of N₂ (10-100 times less than the level of oxygen) gas combined with an O₂ gas flow in the RF plasma source operating at 350 W. The nitrogen concentration in the epilayer ($\sim 1 \cdot 10^{19}$) is two orders of magnitude higher than in the substrate and Hall coefficients were measured in the van der Pauw configuration for 3 μ A and 15 kG. The key results are detailed in table 5.

Average resistivity	40 $\Omega \cdot \text{cm}$
Hole mobility	2 $\text{cm}^2/\text{V} \cdot \text{s}$
Hole concentration	$9 \cdot 10^{16} \text{ cm}^{-3}$
Photoluminescence	3.315 eV
Peaks	3.3568 eV

Table 5: Characteristics of Homoepitaxial MBE N:ZnO Films⁶⁰

The final N-doping paper from Georgobiani et al.⁶¹ used N ion implantation of RF magnetron sputtered ZnO on SiO₂ followed by annealing in O radicals to achieve p-type ZnO. The authors are careful to point out that p-type materials were only realized for N concentrations above the limit for PL. It was determined that low annealing temperatures result in poor introduction of N into oxygen sites, annealing at 800 ⁰C drives N out of the film. Only films with dosages exceeding $1 \cdot 10^{15} \text{ cm}^{-2}$, no luminescence, and 600 ⁰C anneal resulted in p-type conductivity as determined by the thermal EMF method discussed later in chapter 6. Unfortunately, the lack of data for the thickness of the films

may indicate that the researchers simply verified the p-type character of their Si substrates.

2.4.2 Codoping and Cluster Doping

The use of multiple dopant species has been extensively investigated as a possible method of producing p-type ZnO films. T. Yamamoto generated supercells (4 primitive unit cells) of ZnO and proceeded to evaluate the effects of replacing specific sites within the lattice with various dopant ions.⁶² The proposed method uses acceptor and donors simultaneously because of their strong attractive interactions. In compounds such as ZnO with wurtzite structure where the bonding is primarily ionic (O affinity 3.44 compared to 1.65 for Zn), the Madelung Energy is the main contribution to the binding energy of the lattice. Another way to think about ME is a measure of the long range electrostatic interactions in an ionic crystal structure. Lowering the ME in this fashion is predicted to enhance the incorporation of acceptors when repulsive forces between acceptors are dominated by attraction between donors and acceptors. Additionally, energy levels of the acceptors should be lowered while those of the donors are raised. The author concludes that the best chance for p-type carrier generation occurs when Nitrogen is introduced along with Gallium in a 2:1 ratio. L. Wang et al at NREL in Colorado have recently proposed a method to engineer the bonding configuration around a dopant atom to achieve greatest stability.⁶³ Their calculations involving dopant formation enthalpy reveal that cluster doping can lead to stable forms of p-type ZnO. One pertinent observation involves reduction of the energy needed to dope an Oxygen site with Nitrogen by using Zn rich chemical compositions and atomic rather than molecular N.

However, the increased solubility of dopant atoms does not necessarily increase the stability of the system. The dopant clusters of interest are depicted in table 6.

Dopant cluster	Doping type	ΔH_f (eV)		ΔE_{CRZ} (eV)		ΔE_b (eV)	Number of bonds		
		N ₂	NO	N ₂	NO		Ga-N	Ga-O	Zn-N
N-Ga ₄ ^a	n	-3.46	9.64	11.93	25.03	-15.39 (-15.44)	4	12	0
N-Ga ₂ Zn ^b	n	-2.35	6.38	9.02	17.75	-11.37 (-11.29)	3	9	1
N-Ga ₂ Zn ₂ ^b	n	-1.08	3.27	6.12	10.48	-7.20 (-7.14)	2	6	2
N-G ₃ Zn ₃ ^c	i	0.33	0.31	3.21	3.20	-2.89 (-2.99)	1	3	3
N-Zn ₄ ^d	p	1.46	-2.93	0.31	-4.07	1.15 (1.16)	0	0	4
Ga-O ₄ ^d	n	-1.07	3.29	2.90	7.27	-3.98 (-3.96)	0	4	0
Ga-NO ₃ ^c	i	0.33	0.31	3.21	3.20	-2.89 (-2.99)	1	3	3
Ga-N ₂ O ₂ ^b	p	1.53	-2.87	3.52	-0.87	-2.00 (-2.02)	2	2	6
Ga-N ₃ O ^d	p	2.77	-6.01	3.83	-4.94	-1.07 (-1.05)	3	1	9
Ga-N ₄ ^a	p	4.01	-9.14	4.14	-9.01	-0.13 (-0.08)	4	0	12

^aCluster doping. ^bCodoping. ^cCompensated pair. ^dMonodoping.

Table 6: Cluster Doping Predictions⁶³

In general, their findings emphasize the need to evaluate stability and strength of the bonds present before and after doping to determine the most stable configurations. For example, Al + N or Ga + N are better choices than In + N, Al + P, or Ga + As for p-type ZnO dopants due to bond strength. It remains to be seen whether this method is tractable in the lab or industry mass-production.

The first experimental realization of co-doping came from Joseph et al. at Osaka University.⁶⁴ They deposited ZnO on glass using PLD from Ga-doped targets while an Electron Cyclotron Resonance (ECR) plasma source fed with N₂O supplied the Nitrogen. The authors state that N₂O is more effective than N₂ as a source of Nitrogen. X-ray Photoelectron Spectroscopy (XPS) verified the 2:1 ratio for N and Ga as predicted by Yamamoto. Two of their co-doped p-type samples have low resistivity and a carrier concentration on the order of 10¹⁹ cm⁻³ with low mobility (<1 cm²/V*s). A third sample without Ga shows five orders of magnitude increase in resistivity with a 9-fold decrease

in carrier concentration and a mobility of $\sim 2000 \text{ cm}^2/\text{V}\cdot\text{s}$. Another paper by Joseph et al.⁴¹ reports a p-type ZnO film grown on sapphire with a resistivity of $6 \cdot 10^{-3}$ and a carrier concentration of $1 \cdot 10^{21} \text{ cm}^{-3}$. This sample has an estimated activation energy of 13 meV and shows typical semiconductor behavior. The authors also mention that mobility of the p-type films on sapphire (grain size $\sim 500\text{nm}$) is higher than films deposited on glass (grain size $\sim 100\text{nm}$) due to the difference in grain size. K. Nakamura et al have published two reports detailing the interactions between Ga and N for radical source MBE ZnO films on sapphire.^{65, 66} They observed a non-ZnO phase in XRD measurements that was attributed to the spinel ZnGa_2O_4 , a semiconductor with a band gap of $\sim 5\text{eV}$. Nitrogen alone did not incorporate into films deposited at 600°C but the addition of Ga as a codopant increased the N solubility. Although the films showed I-V characteristics and PL luminescence indicative of p-type material, the authors cast doubt on Hall measurements due to the presence of the spinel phase. Unfortunately, M. Joseph et al do not address this same issue. Solubility limits of Ga and N implanted in ZnO were investigated by Komatsu et al. using Secondary Ion Mass Spectroscopy (SIMS).⁶⁷ Samples were implanted with N, Ga, and N+ Ga before 850°C anneal in O_2 . They report a rather low N solubility of $3.8 \cdot 10^{17} \text{ cm}^{-3}$ and a rather large Ga solubility of $5.8 \cdot 10^{19} \text{ cm}^{-3}$. The addition of both Ga and N increased the N solubility by a factor of 400. The authors are careful to point out that the 2N:1Ga complex predicted to generate p-type behavior was not observed and may be difficult to obtain in thermal equilibrium conditions due to the high Ga mobility/solubility and the low N mobility/solubility in ZnO. From the segregation of ZnGa_2O_4 and N_2 swelling at the surface of the co-implanted ZnO film, the researchers conclude that useful codoping schemes must

suppress the level of Ga and control diffusion of dopant ions. The final p-type paper from Singh et al.⁶⁸ reports on co-doped RF diode sputtered ZnO. GaN was placed over the sintered ZnO target and the sputtering gas consisting of O and N was varied from 0-75% Oxygen. Films deposited with Oxygen percentage 50% or higher showed p-type conduction confirmed by Hall measurements and Seebeck coefficients. This suggests that increasing O partial pressure somehow suppresses native ZnO defects. Resistivity of the films increased with O from 60-75% but the hole concentration remained constant. Transmission spectra of p and n-type ZnO was comparable, but codoped ZnO exhibited a smaller band gap than undoped.

2.5 Diluted Magnetic Semiconducting ZnO

Diluted Magnetic Semiconductors (DMS) have been extensively studied over the past 20 years in the hopes of gaining control over another degree of charge carrier freedom. These advanced electronic devices called spintronics include spin field effect transistors (spin-FETs), Photo-induced Ferromagnets, and Spin-injection devices. In order to realize the next generation of spin devices, fabrication of novel materials with large magnetization and above room temperature Curie temperatures (T_c) must be standardized and reproducible. GaN and ZnO are two such materials predicted to exhibit T_c above room temperature upon doping with transition metals (TM).

2.5.1 Predictions

Several research papers from K. Sato and K. Yoshida⁶⁹⁻⁷² have detailed ab initio calculations for transition metal doped ZnO. The authors employ the Korringa-Kohn-Rostoker (KKR) Green's function method based on the Local Density Approximation (LDA) of the Density Functional Theory (DFT). They generated supercells consisting of two primitive ZnO wurtzite unit cells and proceeded to substitute 2 of the 8 Zn atoms with a TM atom. This substitution leads to an impurity concentration of 25%. Further substitution of N at an O site or Ga at a Zn site increased the carrier concentration of holes or electrons respectively by steps of 12.5%. The total energy for the supercell was calculated for aligned (ferromagnetic state) and opposite (anti-ferromagnetic state) TM magnetic moments. The calculations predict that in the absence of N or Ga dopants to introduce carriers, V, Cr, Fe, Co, and Ni doped ZnO will favor ferromagnetic behavior while Mn should exhibit anti-ferromagnetic behavior. For the TM ions other than Mn, the authors propose that electrons in the partially occupied 3d orbitals are allowed to hop

to neighboring orbitals of TM atoms only if the neighboring TM ions have parallel magnetic moments. This effect, called the double-exchange mechanism, means that the d-electron can successfully lower its kinetic energy by hopping in the ferromagnetic state.

Sato and Yoshida point out that supercells containing Mn with no carrier dopants have a carrier concentration of 0 meaning that substitution of Zn with Mn does not bring any additional carriers. When the researchers introduced mobile holes into the supercell the stabilization of a ferromagnetic state was observed due to the double exchange mechanism mentioned before. However, the introduction of carrier electrons did not result in stable ferromagnetic behavior for Mn:ZnO. The authors explain that hybridization of N-2p with Mn-3d causes electrons to enter the host conduction band rather than the Mn 3d states like the holes do. Hence, only holes efficiently participate in the double exchange mechanism required to stabilize ferromagnetic behavior in Mn:ZnO.

2.5.2 Epitaxial Mn:ZnO

T. Fukumura and Z. Jin have collaborated with other researchers in several papers detailing PLD Mn:ZnO deposited on sapphire.⁷³⁻⁷⁷ The films were several hundred nanometers thick and grown at a temperature of 600 °C. XRD showed only wurtzite structure with no impurity peaks and Electron Probe Microanalysis (EPMA) was utilized to confirm the homogeneous distribution of Mn in the films. The researchers report expansion of both a and c axes of ZnO wurtzite with increasing Mn concentration up to 35% as shown in figure 25.

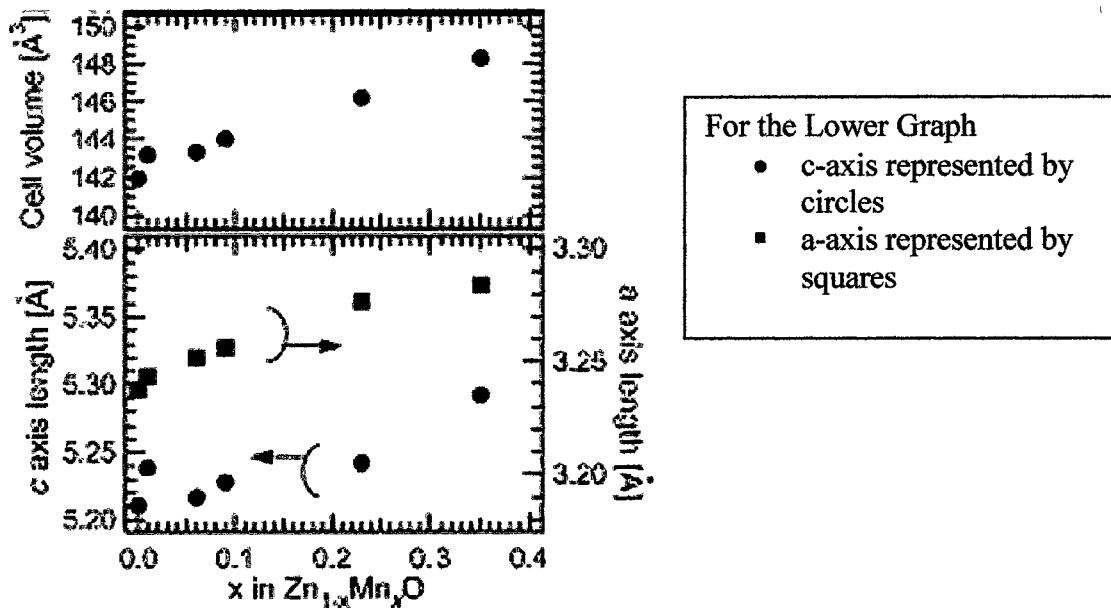
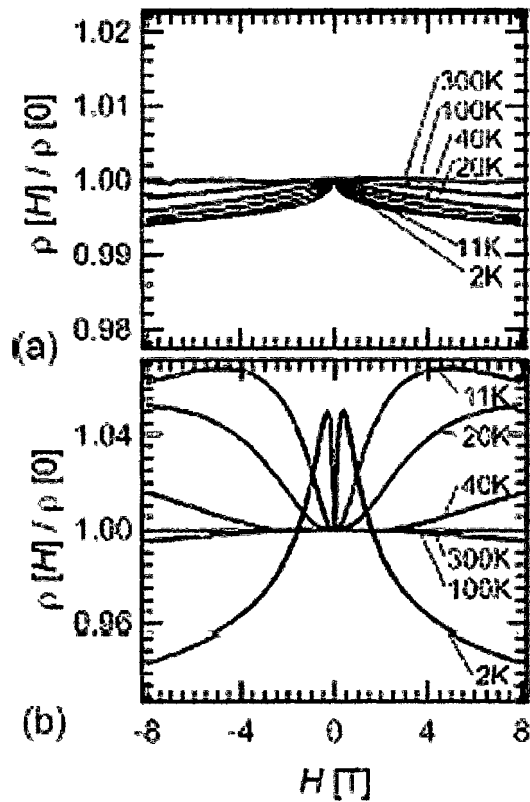


Figure 25: ZnO Lattice Changes as a Function of Mn Concentration⁷³

Also, increasing Mn concentration results in the development of optical midgap absorption near 3eV. In yet another PLD study, the authors introduce 1% Al impurity for increased electron carriers and examine the magnetoresistance (MR) as a function of temperature. They find that a DMS material in the presence of an external magnetic field has a split conduction band corresponding to two different spin orientations of conduction electrons. For low temperature measurements, the electrons redistribute in such a way that they become localized near the TM ions. This results in an increase in resistivity and thus a positive magnetoresistance. However, there are turning points in the MR curves for higher field strengths indicating a competitive process related to weak electron localization that abruptly changes the MR to negative as shown in figure 26.



Note the presence of turning points for Mn doped samples. This shows that for sufficiently large fields the electrons are “freed” from their localized states near the TM ion and begin to participate in conduction. Unfortunately, this only occurs at extremely low temperatures.

Figure 26: MR for Undoped (top) and 19% Mn: Doped ZnO:Al Films⁷³

Jin and Fukumura detail the characteristics of TM doped ZnO by laser MBE. They show the importance of ionic radii and valence state in determining the solubility of various dopants and conclude that Co and Mn are the most soluble with ionic radii of 0.066 and 0.058 respectively closest to that of Zn (0.06nm). Interestingly, the band gap of the Mn doped ZnO increased linearly from 3.32eV for 3% Mn to 3.58 eV for 23% Mn. The MR measurements for this group of films are shown in figure 27.

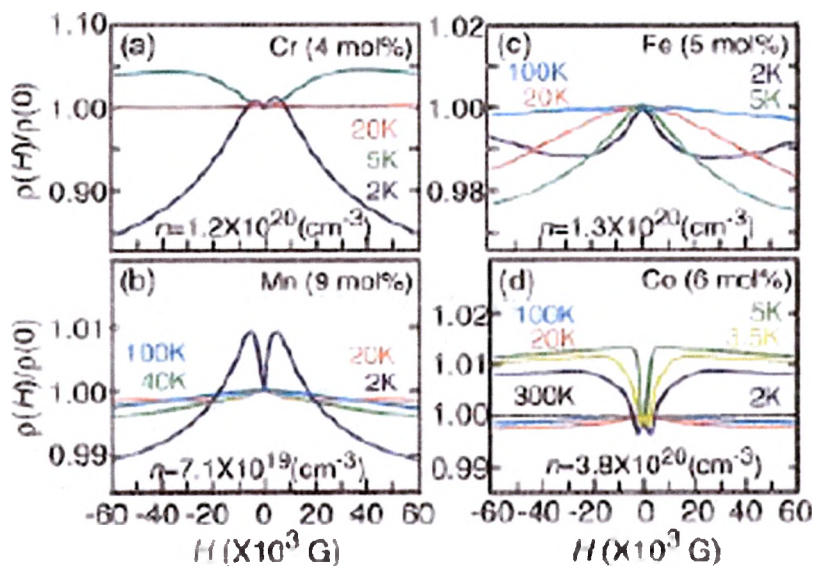


Figure 27: MR for various TM in ZnO prepared by Laser MBE⁷⁷

The researchers used a superconducting quantum interference device (SQUID) to scan their small volume specimens only to report no evidence of ferromagnetism for and TM:ZnO films down to 3K.

G-C Yi. Et al. contradict the previous authors' findings by reporting ferromagnetism in laser MBE Mn:ZnO insulating films.⁷⁸ They also confirmed the change in lattice parameters with increasing Mn concentration using XRD as shown in figure 28.

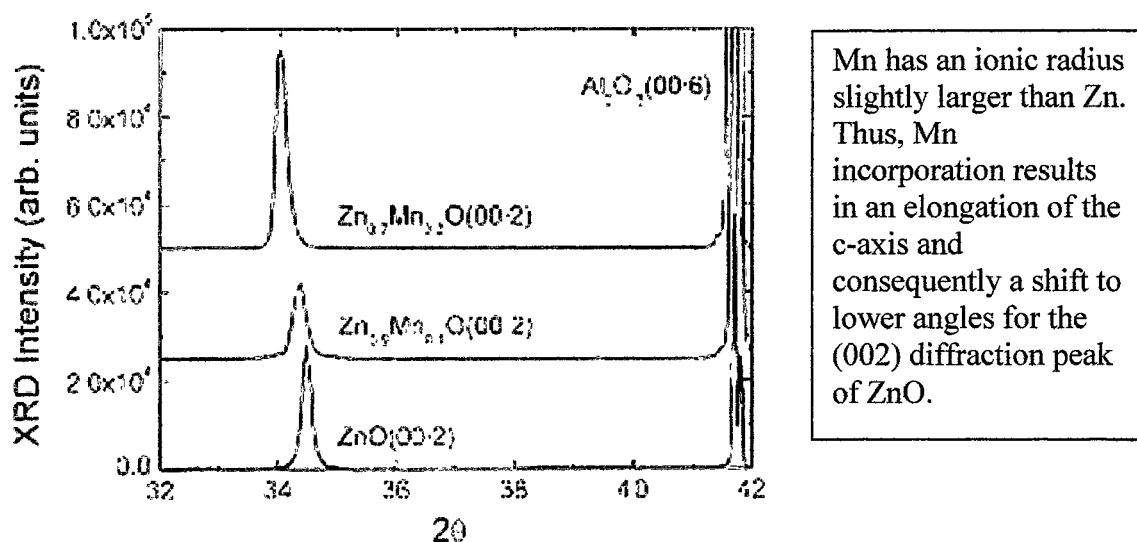


Figure 28: XRD Peak Shift due to Mn doping⁷⁸

The relatively narrow FWHM rocking curves for Mn doped films (0.07°) indicates good crystallinity and compares favorably with the undoped film (0.04°). The hysteresis curve for the film containing 10% Mn (shown in figure 28) indicates a remnant magnetization of 0.9 emu/g with a coercive field of 300 Oe. To keep things in perspective, it is helpful to remember that bulk Fe has a moment of ~ 1700 emu/cm³.

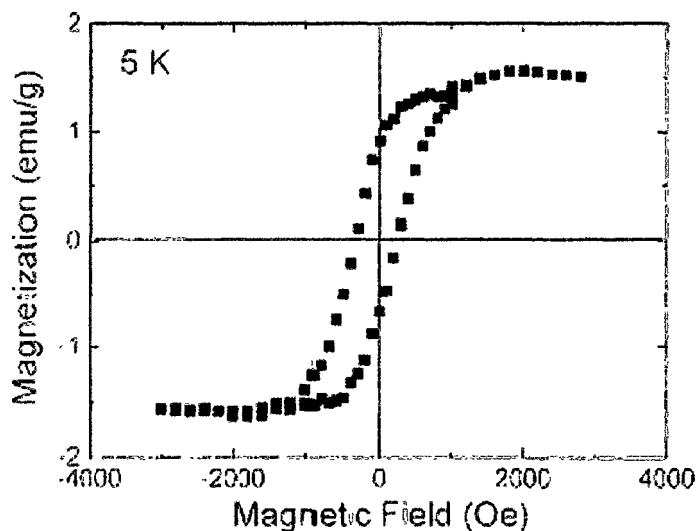


Figure 29: M vs. H Hysteresis Curve for 10%Mn:ZnO Film⁷⁸

The authors conclude that substitutional Mn atoms prefer ferromagnetic ordering below the T_c of 30 and 45 K for the 10% and 30% Mn:ZnO films respectively. While this is a very interesting finding, it has not lived up to the promise of room temperature Curie points for TM doped zinc oxide films. Sharma et al.⁷⁹ provide the light at the end of the tunnel with a study of sintered ceramic and PLD Mn doped ZnO. Mn at concentrations ~2% was found to have an average magnetic moment of 0.16 Bohr magnetons. The researchers conclusively show that low temperature processing leads to room temperature ferromagnetism in Mn:ZnO with the principle data depicted in figures 30 and 31.

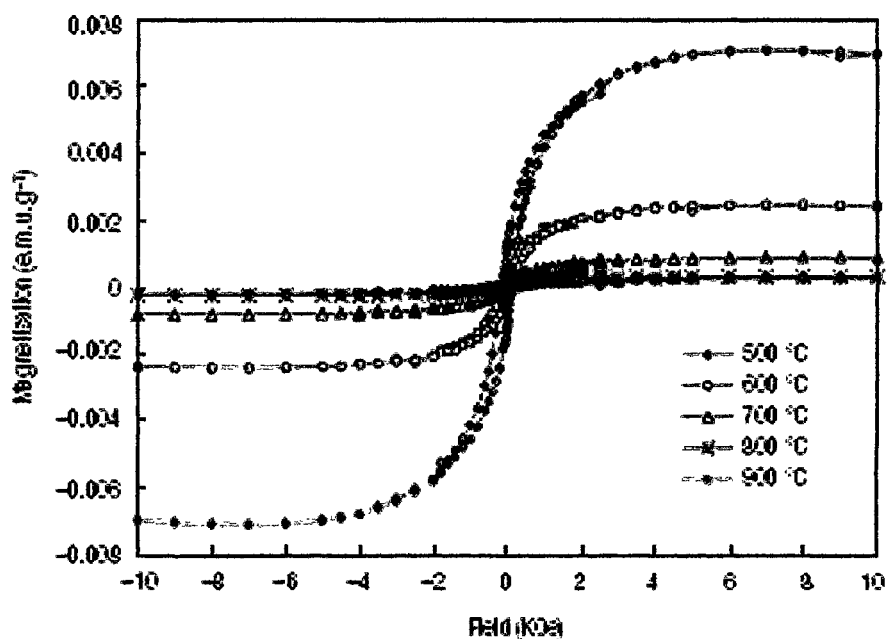


Figure 30: RT SQUID Generated Hysteresis Loops for 2% Mn:ZnO pellets⁷⁹

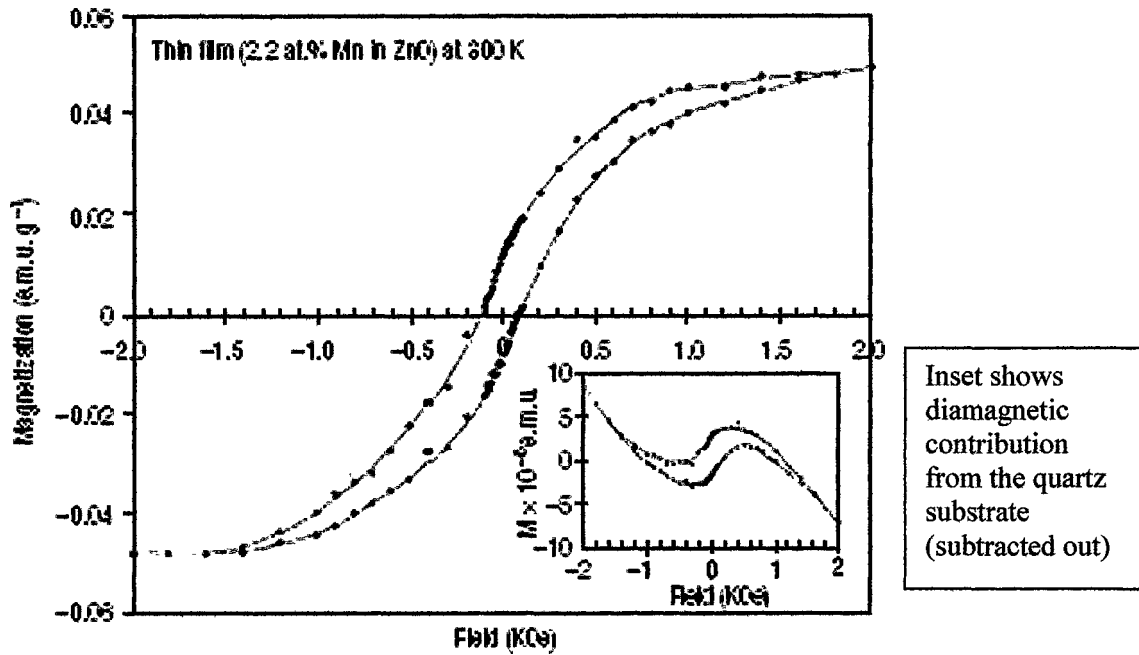


Figure 31: RT Hysteresis Loops for 2.2% PLD Mn:ZnO on Quartz⁷⁹

Sintering the ceramic pellets above 700 °C results in clustering of Mn, promoting anti-ferromagnetic exchange, and destroys room temperature ferromagnetism. The authors claim agreement with theoretical predictions of stable carrier-induced ferromagnetism for <5% Mn:ZnO films.

III. EXPERIMENTAL

3.1 Ion Beam Sputter Deposition

Ion beam sources allow for precise control of both ion flux and momentum while operating at low vacuum to provide protection from background contaminants and impurities.⁸⁰ They are employed extensively for thin film processes including pre-cleaning, etching, and deposition. Highly controlled removal of hydrocarbons and water during pre-cleaning with an ion beam allows for repeatability, improved film morphology, and better adhesion between film and substrate. Ion beam etching provides a uniform consistent etch depth for most materials with an etch rate carefully controlled by ion energy and the reactive chemistry between ion species and target material. Ion beam sputter deposition typically uses two ion beam sources situated in a vacuum system. One source is positioned such that momentum from the ion flux is transferred to a target material with the other source aimed at the substrate itself as depicted in figure 32.

Ion Beam Sputter Deposition System (with ion beam assisted deposition capability)

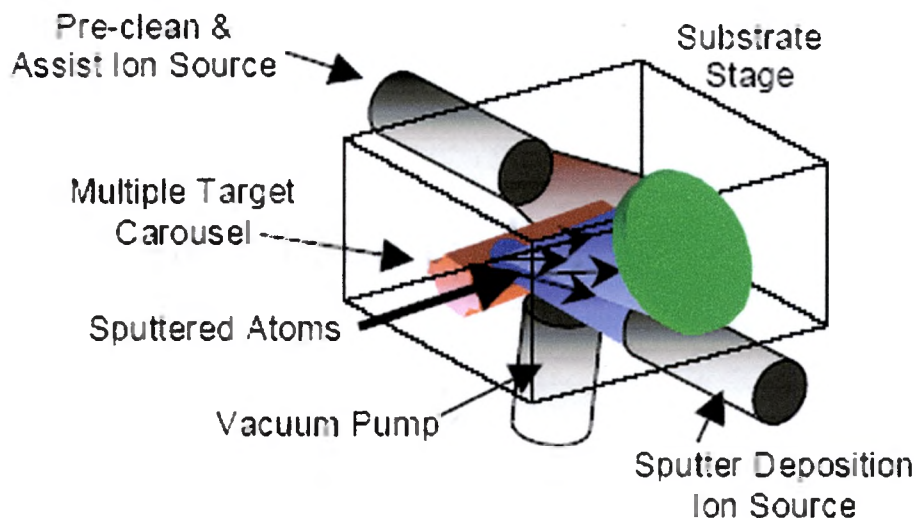


Figure 32: Schematic of a Standard DIBS System⁸⁰

The role of the target source is to sputter away target material to be deposited on the substrate while the assist source is used, usually at lower energy to avoid substrate damage, for cleaning, doping, and relieving stress in the film. The broad beam sources depicted in figure 32 operate by accelerating a beam of inert ions toward a target or substrate material. One of the major advantages of this type of ion source is that its operation is independent of the substrate or target material properties. Ion beam sputtering has many useful applications listed in tables 7 and 8.

Ion Beam Sputter Deposition (IBSD) Applications	
DEVICE / PROCESS	MATERIALS
Advanced Magnetic Heads	NiFe, Ta, Cu, Co, FeMn
Anti-reflection Coatings	MgF ₂ , SiO ₂ , Ta ₂ O ₅ , TiO ₂
Dielectric Films	SiO ₂ , TiO ₂ , AlN, etc.
Encapsulation Films	Si ₃ N ₄ , Al ₂ O ₃
High Reflectance Mirrors	SiO ₂ , Ta ₂ O ₅ , TiO ₂ , Si
Interconnect Films	W, Au, Cu
Laser Facets	Si ₃ N ₄ , SiO ₂ , Al ₂ O ₃ , Si, Ta ₂ O ₅
Narrowband Pass Filters	SiO ₂ , Ta ₂ O ₅ , TiO ₂ , HfO ₂ , Nb ₂ O ₅
Optical Thin Films	Al ₂ O ₃ , Ta ₂ O ₅ , TiO ₂ , SiO ₂
Ring Laser Gyro Mirrors	Multi layer SiO ₂ /TiO ₂
Semiconductor	Si ₃ N ₄ , DLC
Sensors	Composites or Alloys
Superconductors	YBaCuO _x , LaSrTiO _x
Thin Film Heads	NiFe, CrCo
X-ray Optics	W, Cu, Mo, Si, B ₄ C, Ni, C

Table 7: IBSD Applications⁸⁰

Ion Beam Assisted Deposition (IBAD) Applications	
DEVICE / PROCESS	MATERIALS
Anti-reflective Coatings	SiO ₂ , MgF, MgO, TiO ₂ , Ta ₂ O ₅
Decorative Coatings	Cr, TiN, DLC
Diamond Turned Mirrors	Cu, Mo, Dielectrics
Flat Panel Displays	ITO, MgO, ZnO
Hard/Protective Coatings	Al ₂ O ₃ , TiN, CN, BN
Hermetic Coatings on Soft Glass	SiO ₂ , TiO ₂ , Al ₂ O ₃ , MgF ₂
High Reflectance Mirrors	Si, SiO ₂ , TiO ₂ , Ta ₂ O ₅
Infrared Detectors	CdTe, HgCdTe
Infrared Protective A/R Coatings	Diamond-Like Carbon
Laser Facets	SiO ₂ , Si ₃ N ₄ , Ta ₂ O ₅ , Si, Al ₂ O ₃
Metallization	Au, NiCr, Ti, V, Mo
Narrowband Pass Filters	SiO ₂ , Ta ₂ O ₅ , TiO ₂ , HfO ₂ , Nb ₂ O ₅
Optical Coatings	SiO ₂ , TiO ₂ , Al ₂ O ₃ , Ta ₂ O ₅ , HfO ₂ , Nb ₂ O ₅
Plastic Optics	Dielectrics
Solar Cells	In ₂ O ₃ , Sn ₂ O ₃ , a-Si :H, GaAs, TiN, PbS
Solar Thermal Radiation Shields	TiN

Table 8: Dual Ion Beam Sputter (DIBS) Applications⁸⁰

3.2 Radical Assist –Ion Beam Sputtering (RA-IBS) System

The ion beam sputtering system at TSU uses a 3cm Kaufman gridded ion source for the target beam powered by a Commonwealth Scientific Corporation ID 2501 Ion Drive. The source generates ions by bombarding a low pressure gas with electrons. The cathode filament continually emits electrons and is placed in the center of the ionization chamber. The anode is a sheath surrounding the ionization chamber. A permanent magnet is utilized to increase electron ionization efficiency due to an increase in path length. Once the gas species (Ar^+ for our target source) have been generated, they are extracted by a set of electrical grids whose curvature determines the focal length of the ion beam. These grids are used to control both the flux and momentum of the ions bombarding our target material. After the ions pass the outermost grid (accelerator), they encounter the neutralizer filament that ensures mostly neutral species reach the target material to avoid charge buildup. A generalized diagram of a Kaufman source is shown in figure 33.

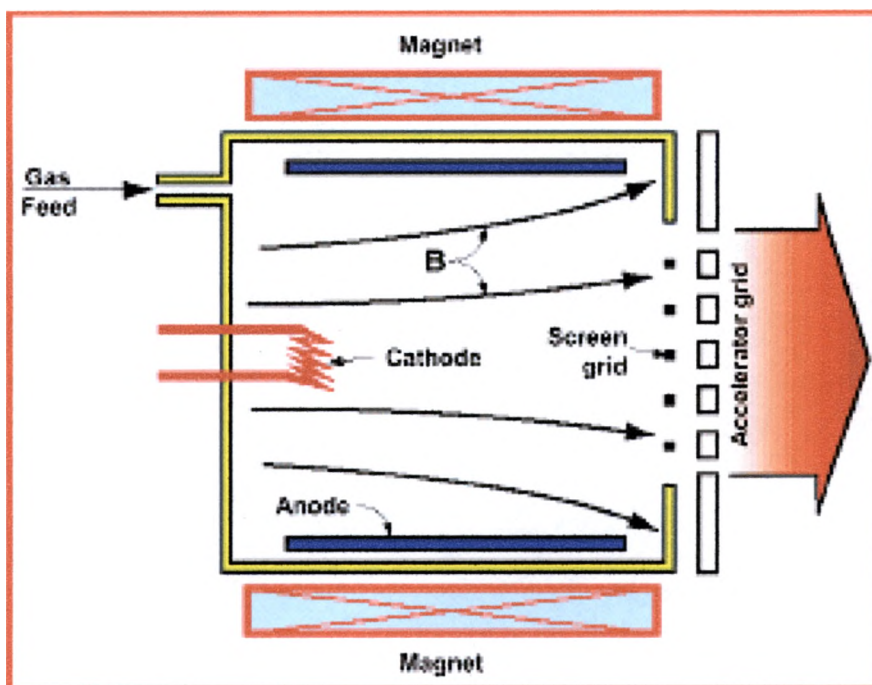


Figure 33: Kaufman Hot Filament Gridded Ion Source⁸¹

Both the cathode and neutralizer filaments are composed of Tungsten-Rhenium wire. The mono-energetic beam focused by the Molybdenum grids bombards one of four 3 inch targets mounted in a rotating indexer approximately 13 cm away. The substrates are mounted on a temperature controlled stage heated by four 1000W bulbs with an upper limit of ~ 700 °C. The sample stage rotates during both heating and deposition to ensure uniformity. The substrate stage can be positioned in the specular and non-specular positions shown in figure 34.

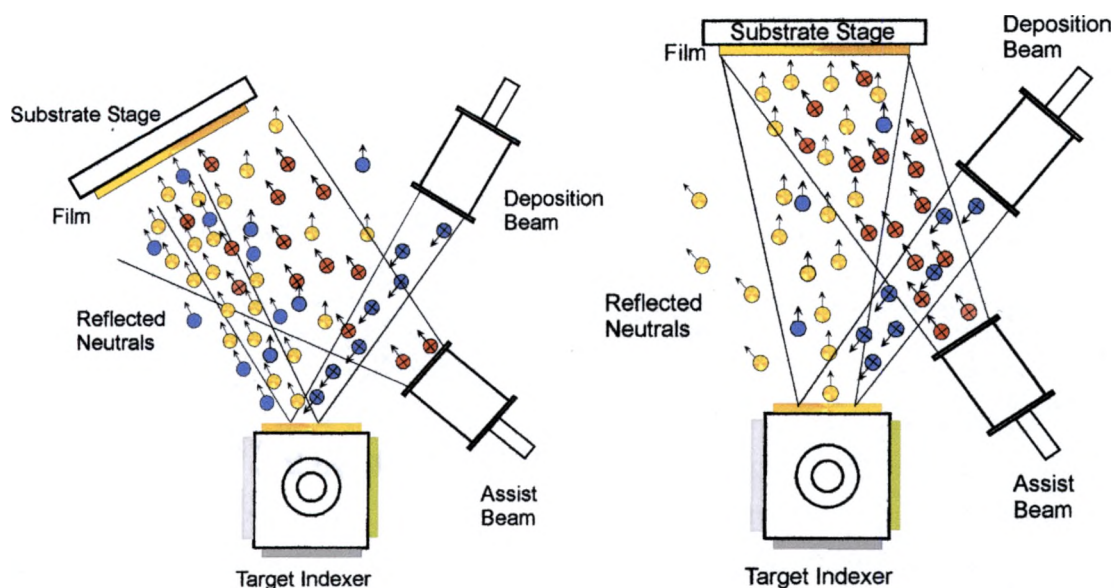


Figure 34: Specular Geometry

Non-specular Geometry [81]

Specular geometry results in substrate bombardment by neutral ions reflected from the target which in turn affects the deposition rate and other growth kinetics.

For this work, all samples were sputtered under the following constant conditions:

- Non-specular position
- Base pressure $\sim 5 \cdot 10^{-7}$ Torr
- Working Pressure $\sim 5 \cdot 10^{-4}$ Torr
- Beam Voltage – 800 V
- Beam Current – 25 mA
- Accelerator Voltage – 120 V
- Accelerator Current ~ 2 mA
- Cathode Voltage ~ 10 V
- Cathode Current ~ 8 A
- Discharge Voltage ~ 45 V
- Discharge Current ~ 1.8 A
- Neutralizer Filament ~ 2.7 A
- Neutralizer Emission – 26 mA
- Argon flow rate – 10 sccm

Our unique system employs an Oxford Applied Research Atomic Radical Source rather than a traditional assist beam. This device delivers low energy atomic species directly to the substrate. When a gas is introduced to the ceramic cavity the application of an inductively coupled RF plasma (generated by the OAR RF source) dissociates the molecules into ions and neutral species. The charged species are contained within the plasma (95% efficiency) while the neutral reactive atoms effuse to the work chamber toward the substrate material. We typically operate the RF source at 300W while minimizing the reflected power with an impedance matching unit. A picture and schematic diagram of the OAR ARS are shown in figures 35 and 36



Figure 35: OAR Atomic Radical Source⁸³

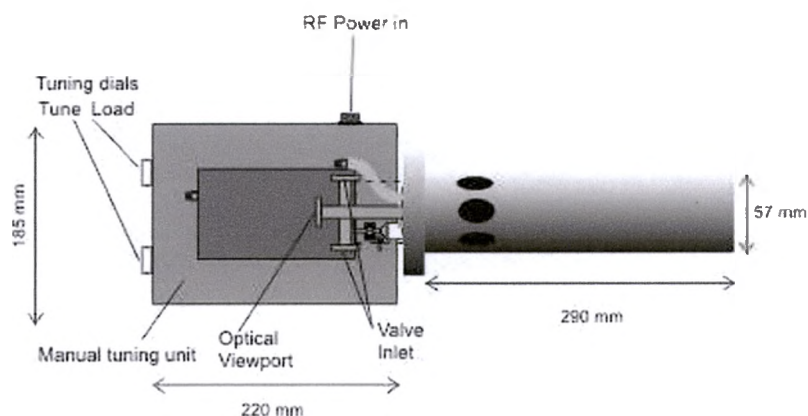


Figure 36: Schematic of OAR Atomic Radical Source⁸³

The substrate stage, target indexer, and ARS are all cooled by a recirculating Neslab HX-75 chiller set to 15 °C during processing. The vacuum system consists of a rough pump (ultimate vacuum $\sim 10^{-1}$ torr), turbomolecular pump (ultimate vacuum $\sim 10^{-5}$ torr) with backing pump, and cryopump with helium compressor (ultimate vacuum $\sim 10^{-7}$ torr). Work chamber pressure is monitored with a Bourdon gauge, thermocouple gauge, and ion gauge for successively lower vacuum ranges. Additionally, the SRS Residual Gas Analyzer (RGA) allows for detection of gas species in the chamber though its performance is somewhat limited due to conductance issues. The relevant electronics, monitors, pressure gauges, vacuum pumps, and other important components are detailed in the appendix.

3.3 Substrate Preparation

In keeping with many of the reports in the literature regarding substrate preparation, we have developed a degreasing protocol as follows:

1. 5 min sonication in Acetone
2. 5 min sonication in Isopropanol
3. 5 min sonication in DI water
4. Dried with N₂ gas at ~30psi
5. Mount sapphire substrates with Ag paste on Stainless Steel plate
6. Heat plate at 150 °C for 10 min in fume hood to set paste and drive off solvent
7. Place SS plate into work chamber
8. Bring chamber to HV regime using Rough Pump and then Turbopump
9. Heat substrate to 300 °C for 30 min using substrate heater
10. Let system achieve base pressure overnight (~15 hrs)

The c-plane sapphire substrates (0001) were purchased from M.T.I. Corporation. The dimensions are 0.5 in X 0.5 in X 0.5mm.

3.4 Experimental Matrices

Phase 1 experimentation resulted in the fabrication of 17 samples in an attempt to optimize the conditions for undoped epitaxial ZnO growth on sapphire. The primary variables, Substrate Preparation, Oxygen Flow During Deposition, Deposition Temperature, and Buffer Layers, are reflected in the Phase 1 experimental matrix shown in table 9.

sample	description	Temp (deg C)	Time (min)	O2 cleaning (sccm)	beam current (mA)	O2 deposition (sccm)
40430	ZnO on Al ₂ O ₃	650	30	3	25	1
40503	ZnO on Al ₂ O ₃	650	30	5	25	3
40506	ZnO on Al ₂ O ₃ molecular	650	30	m5	25	m3
40510	ZnO on LT buffer on Al ₂ O ₃	350--650	5--30	5	25	3
40514	ZnO on MgO on Al ₂ O ₃	650	1--30	5	15--25	0--3
40517	ZnO on Al ₂ O ₃	650	30	5	25	5
40518	ZnO on Al ₂ O ₃	550	30	5	25	5
40519	ZnO on Al ₂ O ₃	450	30	5	25	5
40520	ZnO on HT buffer on Al ₂ O ₃	650--350	5--30	5	25	5
40607	ZnO on LT buffer on Al ₂ O ₃	450--650	5--30	5	25	5
40608	ZnO on Al ₂ O ₃	650	30	5	25	7
40609	ZnO on Al ₂ O ₃	650	30	5	25	9
40611c	ZnO on MgO on Al ₂ O ₃	650	5--30	5	25	5
40611a	ZnO on MgO (100)	650	30	5	25	5
40611b	ZnO on MgO (111)	650	30	5	25	5
40615	ZnO on Al ₂ O ₃	650	30	0	25	5
40708	ZnO on Al ₂ O ₃	650	30	5	25	0

Table 9: Phase 1 (undoped ZnO) Experimental Matrix

Phase 2 experimentation, detailed in table 10, consisted of targeted attempts at producing:

- highly conductive epitaxial n-type ZnO through Ga doping
- p-type epitaxial ZnO through N doping
- Epitaxial ZnO with room temperature ferromagnetic properties via Mn doping

sample	description	Temp (deg C)	Time (min)	O2 cleaning (sccm)	beam current (mA)	O2 deposition (sccm)
40614	ZnO on Al ₂ O ₃	650	30	5	25	5 N ₂
40617	Mn,Ga:ZnO on Al ₂ O ₃	650	30	5	25	5
40618	Mn,Ga,N:ZnO on Al ₂ O ₃	650	30	5	25	5 N ₂
40622	Mn:ZnO on Al ₂ O ₃	400	30	5	25	5
40623	Mn:ZnO on Al ₂ O ₃	650	30	5	25	5
40624	Mn,N:ZnO on Al ₂ O ₃	650	30	5	25	5 N ₂
40629	Ga:ZnO on Al ₂ O ₃	650	30	5	25	5
40701	N, Ga:ZnO on Al ₂ O ₃	650	30	5	25	5 N ₂
40709	Ga:ZnO on ZnO buffer on Al ₂ O ₃	650	30--30	5	25	5--5
40712	N, Ga:ZnO on ZnO buffer on Al ₂ O ₃	650	30--30	5	25	5--5 N ₂

Table 10: Phase 2 (doped ZnO) Experimental Matrix

IV. X-RAY ANALYSIS

4.1 Theory

There are many interesting radiative processes that occur for short wave length photons with energies on the order of keV. X-rays, named so due to their mysterious nature, were first detected by W. K. Roentgen (who later won the Nobel Prize for this discovery) in 1895 during experiments involving electron currents between the terminals of an evacuated gas tube.⁸⁴ M. T. F. von Laue conclusively showed that x-rays have wave properties when in 1912 he diffracted beams of x-rays through crystals whose lattice spacings were on the order of the nanometer wavelength of the incident radiation. While generating x-rays in the sealed tube, it was discovered that increasing the applied voltage led to shorter wavelength photons. Thus was born an invaluable tool for use in medicine, industry, and especially examining the crystal structure of matter.

Diffraction of x-rays by a crystal lattice is due to interference of waves that reflect from parallel crystal planes. Even though every atom in the material scatters incident radiation in all directions, the Bragg condition, depicted in figure 37, singles out a certain direction for the scattered wave which results in a collective constructive interference effect from the atoms that lie in a crystal plane.

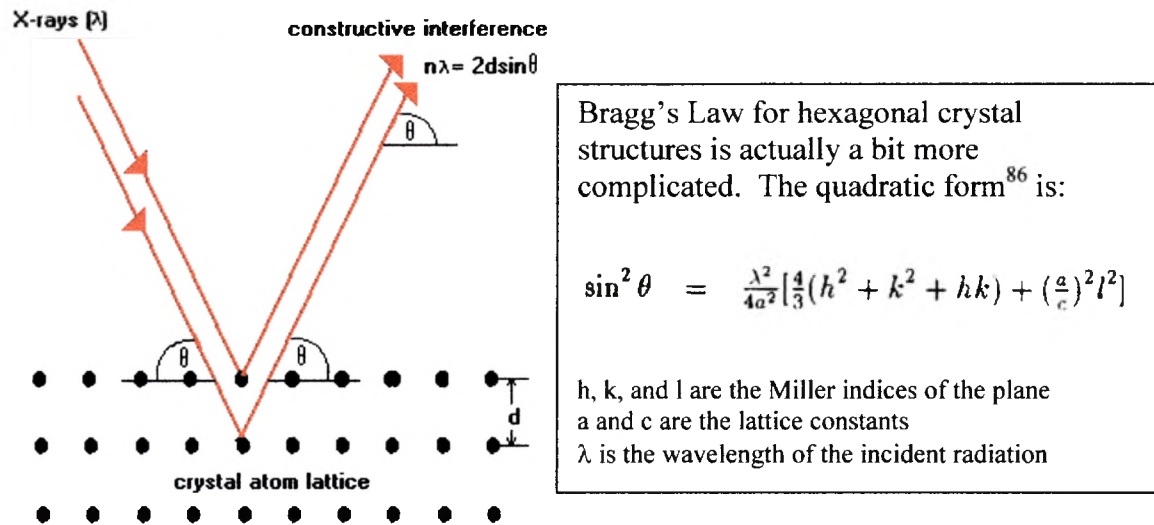


Figure 37: Bragg Condition for X-ray Diffraction⁸⁵

The generation of x-rays typically occurs in a sealed tube where electrons are boiled off a hot filament and accelerated to collide with a metal target. A general diagram of a sealed tube x-ray source is shown in figure 38.

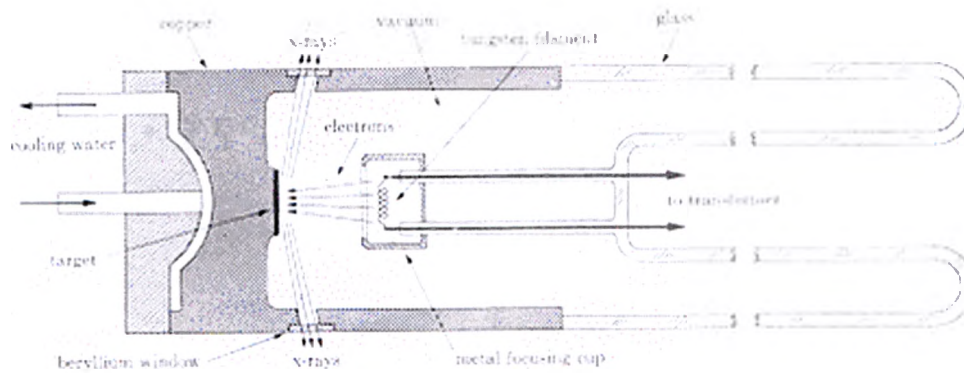
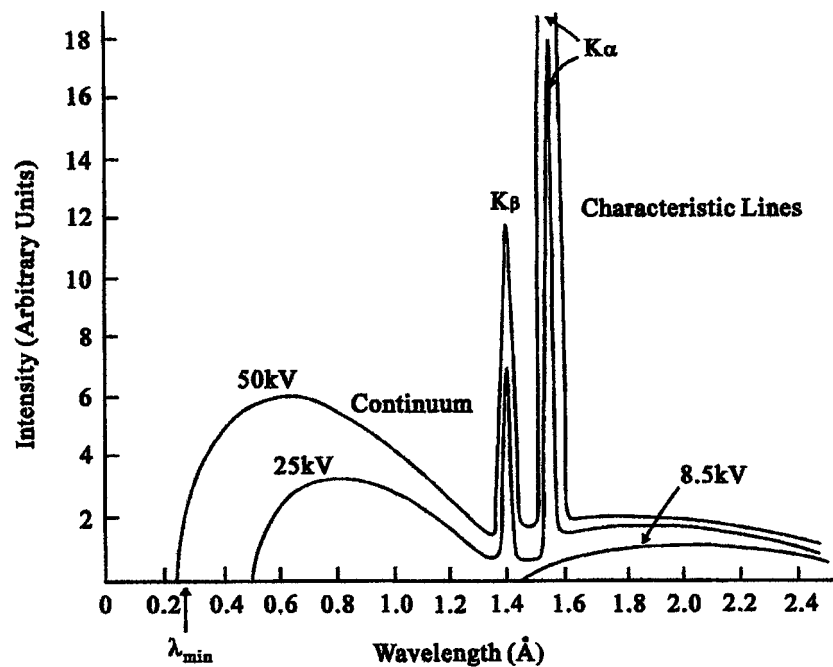


Figure 38: Sealed Tube X-ray Source⁸⁵

The abrupt deceleration results in an energy transfer that mostly heats up the metal but the remainder is emitted in a radiative process. The radiation exhibits a broad continuous

component above a cutoff wavelength as well as a set of discrete emissions as depicted in figure 39.



Spectrum of X-ray emission from a copper target at various excitation voltages

Figure 39: Spectrum of Copper X-ray Source⁸⁵

The broad classical radiation component, also called bremsstrahlung (German for “braking radiation”) results from the rapid deceleration of the electrons upon collision with the metal. The minimum wavelength is understood via de Broglie’s matter wave equation⁸⁴:

$$\lambda_{\min} := \frac{h \cdot c}{e \cdot \phi}$$

Phi is the voltage across the terminals
 $h=6.626 \cdot 10^{-34} \text{ J}\cdot\text{s}$
 $c=2.998 \cdot 10^8 \text{ m/s}$
 $e=1.602 \cdot 10^{-19} \text{ C}$

Hence frequency varies from 0 to a maximum while λ ranges from a minimum to infinity. The discrete lines represent photons whose energy is characteristic of the metal

target. When the incident electrons knock out an inner shell electron near a metal atom, a higher level electron will lose energy in the form of a photon to take its place. It is no small matter that this is direct evidence for the quantization of electronic energy levels in matter. The complicated structure factor, F_{hkl} , for a miller plane depends on the scattering factors of the atoms and their positions within the unit cell. This advanced theory goes beyond the simple Bragg condition to explain variations in intensity between similar peaks as well as the conspicuous absence of some reflections. Some of the basic rules for extinction due to a vanishing structure factor for different crystal types are summarized in table 11.

Symmetry	Extinction Conditions
P	none
C	$hkl; h + k = \text{odd}$
B	$hkl; h + l = \text{odd}$
A	$hkl; k + l = \text{odd}$
I	$hkl; h + k + l = \text{odd}$
F	$hkl; h, k, l \text{ mixed even and odd}$
$2_1 \parallel b$	$0k0: k = \text{odd}$
$c \perp b$	$h0l: l = \text{odd}$

P = primitive lattice
 C = side-centered on c-face (001)
 I = body centered
 F = face centered on all faces

Table 11: Systematic Extinctions Due to Translational Symmetry Elements⁸⁷

The standard geometry for x-ray characterization is the 2Theta-Omega scan pictured in figure 40.

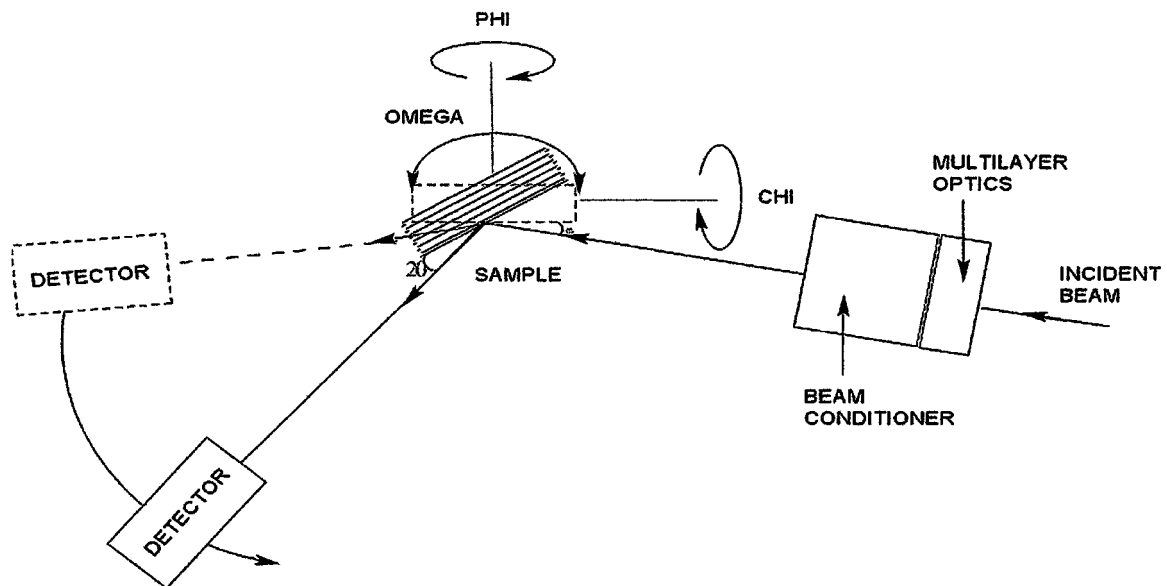


Figure 40: Symmetric 2Theta-Omega X-ray Scan Setup⁸⁸

The general requirement is that for every degree moved by omega (sample) the 2Theta arm (detector) moves by twice that amount. This symmetric scan mode ensures that the angle of incidence and the angle of reflection remain congruent over the range of angles in the scan.

4.2 Bede D1 Diffractometer

X-ray characterization was carried out on a Bede D1 diffractometer at TSU.

Relevant diagrams, pictures, and operating procedures may be found in the appendix.

The x-ray source is a sealed copper tube typically operated at 40kV accelerating potential and 40 mA accelerating current using a Spellman DF3 high voltage power supply. The source is cooled by a Neslab CFT recirculating chiller. The top view of the Bede D1 is shown in figure 40.

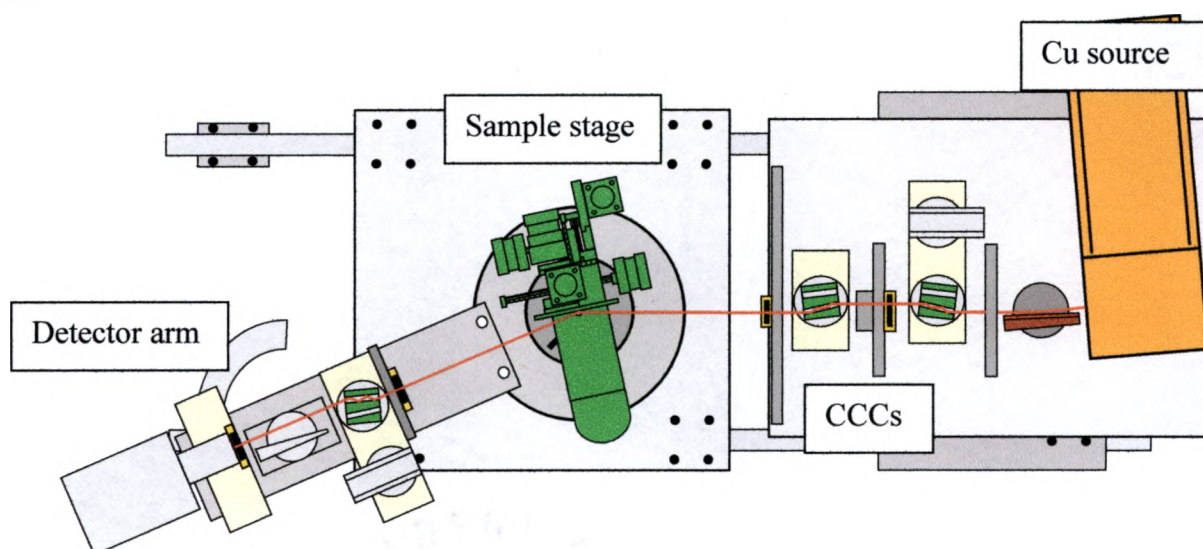


Figure 41: Top-Down View of the Bede D1 Diffractometer⁸⁹

When operating in high resolution mode (HRXRD), intensity is sacrificed in order to ensure that the x-ray beam is monochromatic. As mentioned before, the characteristic x-rays due to electronic transitions occur at many wavelengths but the L to K level transitions ($n=2$ to $n=1$) are the most probable and therefore the most intense. Hyperfine splitting of the energy levels further separates these so called alpha transitions into two discrete wavelengths known as $K\alpha_1$ and $K\alpha_2$ with the latter having roughly $\frac{1}{2}$ the

intensity and a slightly longer wavelength. Silicon Channel Cut Collimating crystals shown in figure 41 filter out all wavelengths of radiation except for $K\alpha_1$ providing the best resolution for crystal analysis.

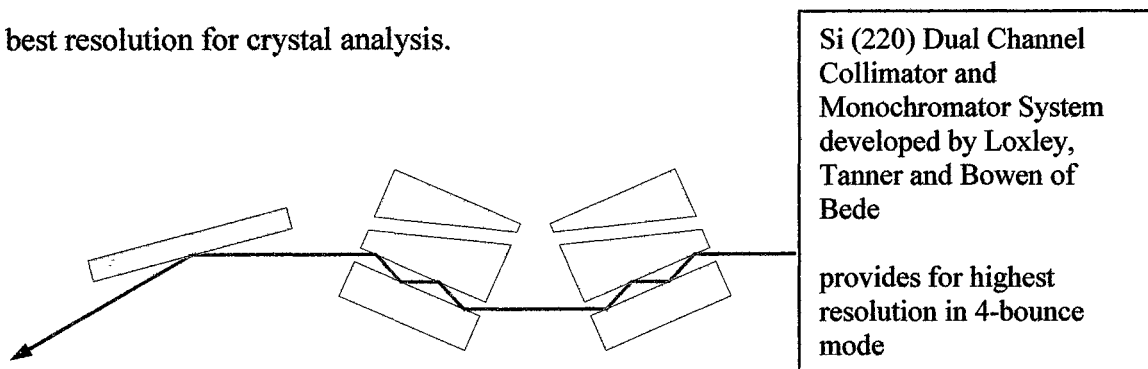


Figure 42: Silicon Dual Channel Collimating Crystals⁸⁹

4.2.1 Types of Scans

The types of scans performed for this work include Omega-2Theta, Omega Rocking Curve, Phi Scans, and X-ray Reflectivity (low angle $\omega-2\theta$). The first scan maintains the Bragg geometry of equal incident and diffracted angle with the motor positions given in arcseconds (3600 arcs per degree). These scans tell us something about the strain, thickness, and crystallinity of the film. The best case scenario for epitaxial thin films would show an extremely narrow central peak flanked by symmetric, persisting, and periodic satellite fringes. Omega rocking curves are a scan of only the omega motor (again in arcseconds) with a fixed 2Theta position. As with the Omega-2Theta scan, a narrow peak is desirable. This type of scan can help determine crystal quality and the degree of mosaicity within the film. The best visualization I can offer for this concept is a mosaic tile floor whose tiles all lie parallel to the ceiling. Mosaicity is the degree to which all the tiles align within the plane of the floor. Phi scans are used to examine the symmetry of crystal planes that are not parallel to the substrate material, so called "asymmetric planes". A typical phi scan rotates the sample through 360 degrees to

examine the symmetry of the plane in question. Ideally, the peaks will all have the same intensity and appear uniformly spaced depending on the symmetry of the plane. Finally, XRR is used to evaluate surface and interface roughness as well as layer thickness. The features of a reflectivity scan are discussed in the next section.

4.2.2 XRR Modeling with REFS

The qualitative features of an XRR scan are briefly detailed in table 12.

SCAN FEATURE	QUALITATIVE INTERPRETATION
Periodicity of fringes	higher frequency indicates thicker film
Amplitude of fringes	Smearred interfaces decrease amplitude
Damping of fringes	Substrate roughness kills the signal
Best-fit slope of signal	Faster decay indicates rougher film

Table 12: XRR Qualitative Features

In order to quantitatively interpret these scans, we use modeling software based on Dynamical Simulation called Reflectivity and Fluorescence Simulation (REFS). This software, a member of the Bede program suite, uses Dynamical Simulation to provide a quantitative indication for the degree of fit between experimental data and a layer model. The user builds a model by adjusting thickness, density, and interface roughness for all layers as well as the incident intensity. The extensive endmember database allows for construction of layers using materials defined by density, lattice parameters, Poisson ratio, and unit cell positions of the atomic species. An example of a “good fit” for one of our ZnO films is shown in figure 43.

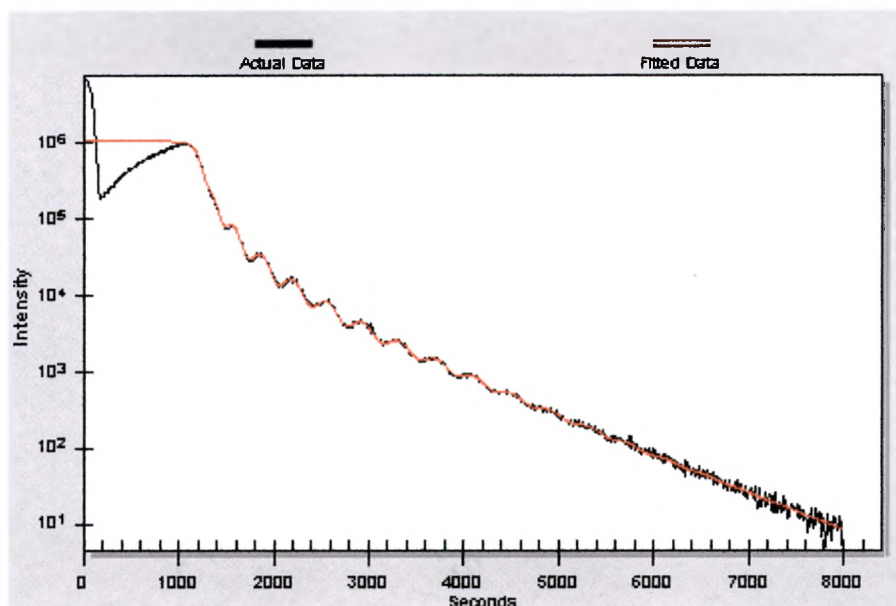


Figure 43: “Good” REFS fit of a ZnO film

The inherent nature of an XRR scan limits information about the crystalline nature of the film but provides much information about the interfaces in the layered film.

4.2.3 HRXRD Modeling with RADS

Yet another program in the Bede suite called RADS (Rocking Curve Analysis by Dynamical Simulation) is used to quantify the fit of layer models to experimental data taken at higher angles than typical XRR. The standard input parameters are similar to REFS but the program is capable of examining much more complicated diffraction to provide information about the crystal structure of the sample. It is rather unfortunate that the most prominent features of our HRXRD scans are the Al₂O₃ (006) and ZnO (002) peaks. Attempts to model a substrate and epilayer with different miller indices resulted in program errors or simulations that never converged. Mr. Kevin Matney from Bede Inc. was very helpful in his attempts to mitigate this problem. We tried “fooling” the software into thinking it was looking at the Al₂O₃ (002) plane by reducing the c lattice parameter in the sapphire endmember data file by a factor of 3. Additionally, he

redefined the atomic positions of the Al and O atoms to match those of a typical wurtzite unit cell. While these tricks resulted in an eventual fit from the oblivious program algorithm, it was widely agreed that the reported data had little scientific value. To give you an idea of the capabilities of RADS, I have included a short section in the appendix detailing analysis of an InGaN Multiple Quantum Well Structure I recently completed in collaboration with researchers at Strathclyde University.

4.3 HRXRD Data

4.3.1 Substrate Cleaning

Reports from the literature all seem to agree that epitaxial growth is most favorable when ZnO is deposited on an O-terminated sapphire surface. This plasma treatment not only removes contaminants, but allows for a reduction in the lattice mismatch at the ZnO/Al₂O₃ interface from 32% to 18%. In order to optimize this plasma treatment, we have conducted film growth for 3 and 5 sccm radical Oxygen, 5 sccm molecular Oxygen (radical source was not on), and a control sample with no plasma treatment.

Figure 44 shows a comparison of the Omega-2Theta symmetric scans of the ZnO (002) lattice plane for several samples. The reader should note that these graphs have been normalized and shifted along the vertical axis for clarity (arbitrary units). The ZnO (002) plane is parallel to the plane of the substrate and hence tells us something about the degree of crystallinity in the c-axis direction. The additional fringes to the left and right of the central peak are called pendellosung or satellite fringes. The presence of such satellite peaks is a tell-tale characteristic of excellent crystal quality much like the multiple spots seen when light diffracts through a finely crafted grating. This means that the repeated lattice parameter, c , for the ZnO (002) plane is extremely regular throughout the epilayer as evidenced by the multiple order constructive interference fringes. An additional feature of these pendellosung fringes is that they are a crude indicator of film thickness. Films with more closely spaced pendellosung fringes compared to others are thicker. Using a program in the Bede suite called Peaksplit, we can estimate the thickness of the layers by noting the separation between the central peak and the n^{th} order

fringe and plugging the appropriate crystal parameters into the database. The symmetry of the fringes about the central peak is indicative of a relaxed structure with little or no strain. Yet another feature of the Omega-2Theta graph is the width of the central peak at half of its maximum value (FWHM). A broad FWHM implies poor crystallinity in the film. However, one must be careful with this interpretation to avoid comparing apples to oranges because the peak broadens for thinner films. Thinner films tend to show increased strain and may have a greater defect density than thicker films. So while we can say qualitatively that a given peak may be narrower than another, it does little good without assertion that the films are of the same order of thickness.

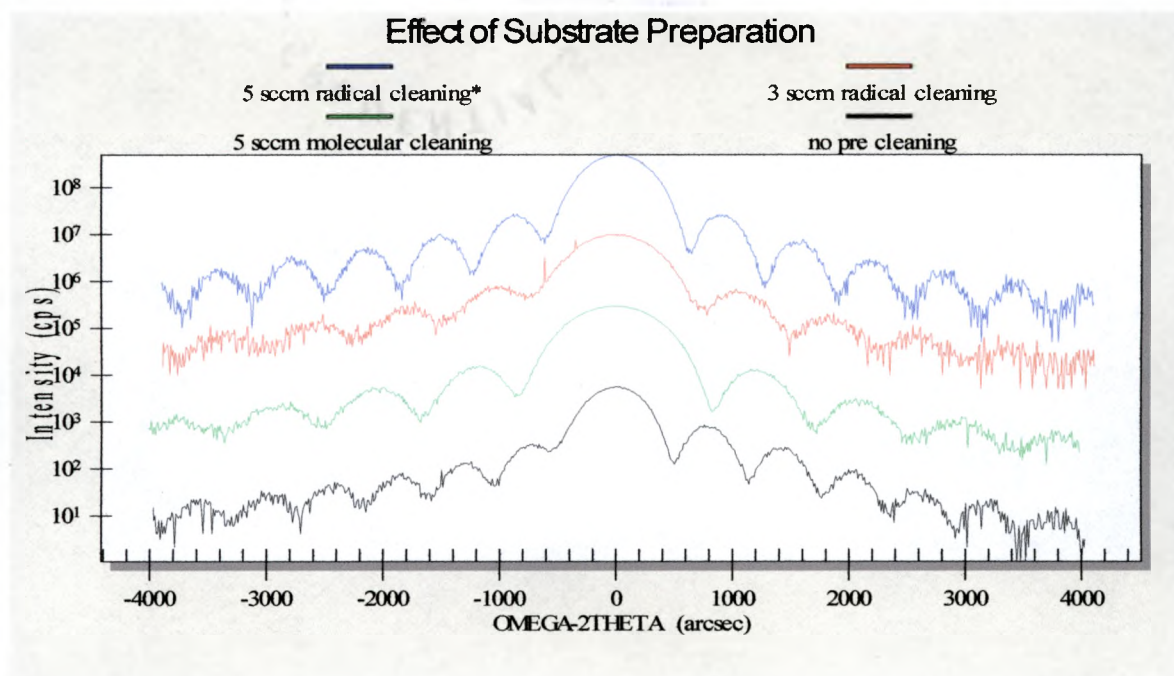


Figure 44: Omega-2Theta scan of ZnO (002) for Different Plasma Treatments

The trend of increasing intensity and symmetry for the satellite peaks indicates that the film exposed to 5sccm oxygen radical cleaning prior to deposition has the superior crystallinity. It is for this reason that we have adopted this level of plasma treatment

along with the degreasing protocol mentioned earlier as part of our optimized process conditions.

The next graph shown in figure 45 is an example of the Omega rocking curve. This type of scan is conducted after optimizing the ZnO (002) peak and then varying the Omega position without moving the detector arm. Once again, these peaks have been normalized and shifted vertically to aid in comparison. As mentioned previously, we can tell something about the crystallinity and the mosaicity of the plane by examining deviations in the Omega position with a fixed detector position. A narrow FWHM is most desirable. One important feature of these scans to point out is that for our ZnO films, we don't observe a standard Gaussian or Lorentzian shaped function that one expects from a polycrystalline sample. Instead, the scan almost seems to be composed of a very narrow peak superimposed on a broad shallow peak. This may be indicative of a layered structure for the film containing both highly crystalline layers as well as porous rough layers. The rough layers are most likely adjacent to the substrate due to the large lattice mismatch between ZnO and sapphire. All data for FWHM is reported for the narrow peak.

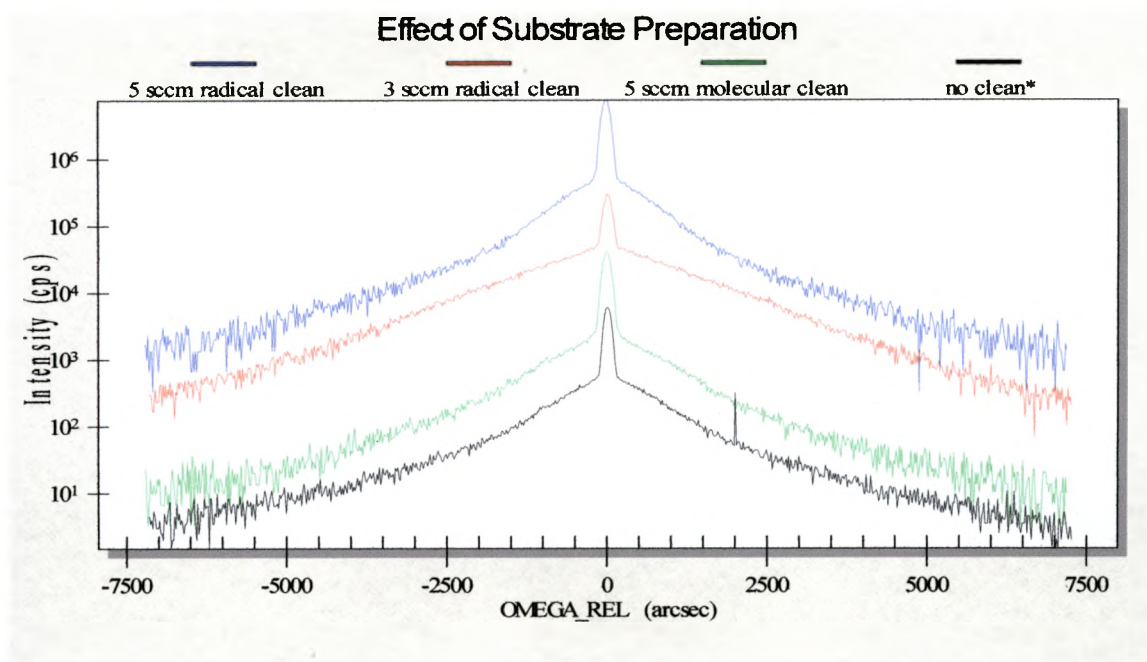


Figure 45: Omega Rocking Curve of ZnO (002) for Different Plasma Treatments

A comparison of the FWHM for these samples shows that the untreated sample has the narrowest peak while the sample treated with 5 sccm O plasma is more intense than the others by >1000 counts per second (cps). While intensity is sometimes a good measure of improved crystallinity, it is difficult to perform all of the scans during a single session. Therefore, the alignment of the X-ray source and detector arm may play a role in the different intensities. However, variations on the order of 1000s of cps are not commonly observed. The values for the FWHM are shown in table 13

Oxygen Plasma Treatment (sccm)	FWHM rocking curve (arcsec)
3	163.1
5	160.8
m5	152
0	143.2

Table 13: FWHM of ZnO (002) for Different Plasma Treatments

From this data, it would appear that the radical cleaning procedure does not benefit the crystallinity or mosaicity. We speculate that this is due to possible damage to the substrate surface during oxygen bombardment. However, we must also ensure an oxygen terminated surface of the substrate to reduce lattice mismatch. To resolve this apparent discrepancy, additional sapphire substrates should be prepared to determine the level of surface roughening during plasma treatment using XRR and AFM. The numerical values for FWHM are not easily interpreted unless one has a standard reference material of known crystalline quality. Figure 46 shows the Omega rocking curve for a bare sapphire substrate.

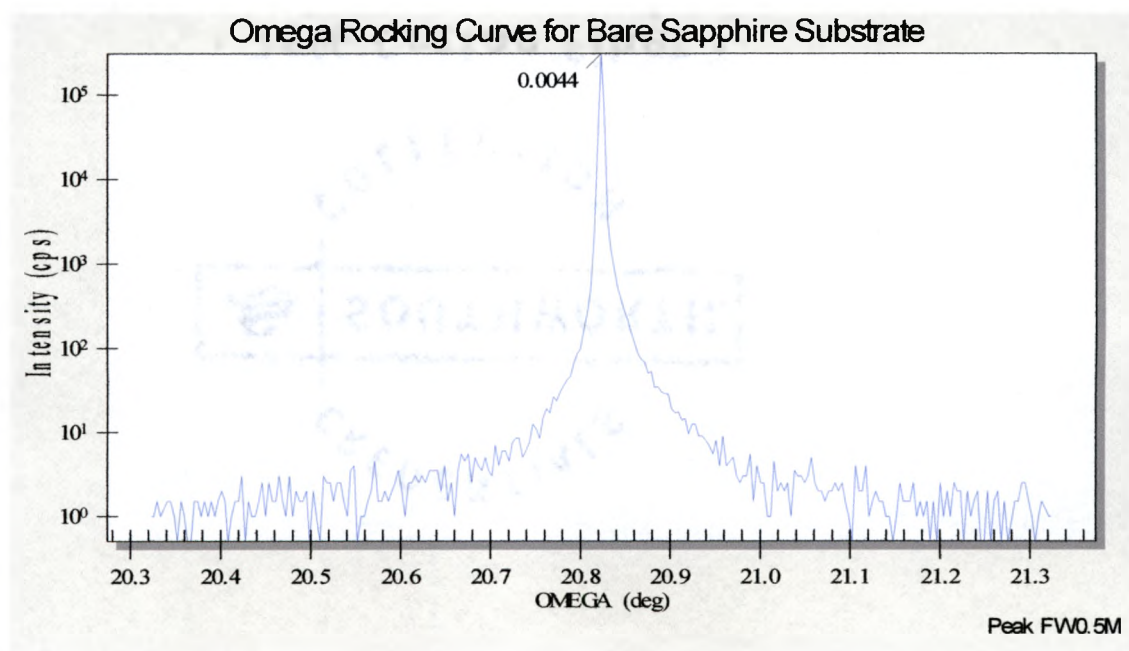


Figure 46: Omega Rocking Curve for Bare Sapphire Substrate

The sapphire substrate is an extremely well ordered crystal. The FWHM value of 15.84 arcseconds is composed of both the peak and instrumental broadening. If we assume negligible broadening for the sapphire crystal, we can employ Scherrer's equation⁹⁰ to calculate crystallite size, t :

$$t = \frac{0.9\lambda}{B \cos \theta_B}$$

λ is the wavelength of the incident radiation
 B is the FWHM of the omega rocking curve
 θ_B is the diffracting angle

Sample	Crystallite Size (angstroms)
Sapphire Substrate	infinite
3 sccm plasma treatment	32.2
5 sccm plasma treatment	32.6
5 sccm molecular treatment	34.5
No oxygen treatment	36.7

Table 14: Approximate Crystallite Size for Different Plasma Treatment

A trend toward larger crystallite size indicates improved epitaxial growth for the untreated sample though the ZnO films all exhibit similar crystallite size compared to the extremely well ordered sapphire substrate. Once again, Oxygen terminated surfaces are the goal of plasma treatment but further investigation may reveal substrate damage as a negative side effect.

In order to evaluate the strain in the system due to lattice and thermal expansion coefficient mismatch between substrate and epilayer, it is important to note the relative position of the ZnO (002) peaks with respect to the sapphire substrate because any shift is a direct indicator of strain along the c-axis. Figure 47 shows that the peaks are shifted by different amounts from the expected Omega position for bulk crystal ZnO (002). These curves were all normalized to the (006) sapphire substrate plane (2Theta=41.68 degrees)

seen here at Omega = 0 and shifted on the vertical axis for clarity.

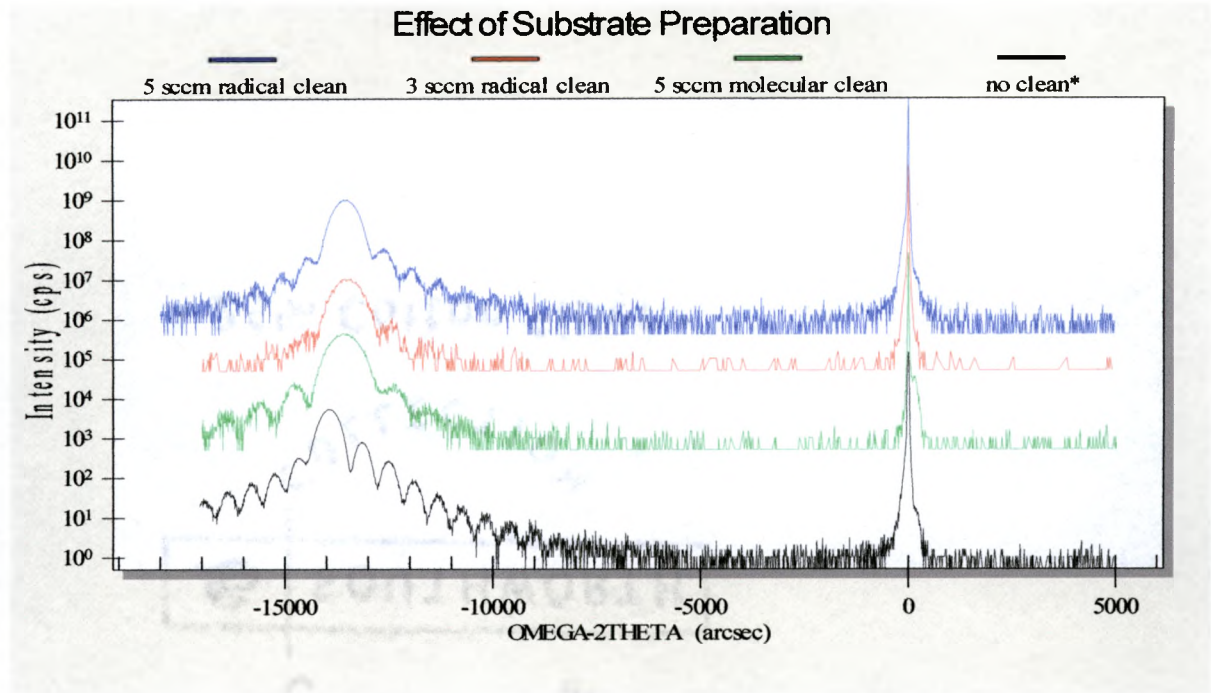


Figure 47: ω - 2θ curves of Al_2O_3 (006) and ZnO (002) for Different Plasma Treatment

The samples show differing amounts of strain⁹¹ calculated using the following formulae:

$$e_{zz} := \frac{c - c_0}{c_0} \quad (\text{average uniform strain along the c-axis})$$

Where c is calculated from the above scans using Bragg's Law and c_0 is taken as 5.2078 angstroms from the bulk value for ZnO crystal⁷

$$e_{xx} := \frac{a - a_0}{a_0} \quad (\text{average uniform strain along the a-axis})$$

With the relationship due to the perpendicular orientation of (002) to the plane of the film we have:

$$e_{zz} := -2 \cdot \left(\frac{C_{13}}{C_{33}} \right) \cdot e_{xx} \quad (\text{in-plane biaxial strain})$$

Where $C_{13}=106.1$ GPa and $C_{33}=209.5$ GPa are the elastic stiffness coefficients¹⁴ for bulk ZnO. We can see from these calculations, shown in table 15, that the untreated film exhibits the greatest residual strain along the c-axis (elongation) and correspondingly the most in plane bi-axial strain (compression). It would also appear that the sample with 3 sccm radical cleaning shows the least strain along the c-axis though it's satellite fringes do not persist as long as the sample cleaned at 5 sccm.

Level of clean (sccm O2)	ZnO (002) 2Theta position	calculated lattice constant c (angstroms)	ave uniform strain along c-axis (residual strain)	In-plane biaxial strain (MPa)
3	34.235	5.235	0.00528	-5.216
5	34.173	5.243	0.00677	-6.687
m5	34.173	5.243	0.00677	-6.687
none	33.933	5.279	0.01368	-13.509

Table 15: Strain for Different Plasma Treatment

The positive values for residual strain indicate elongation of the c-axis while the corresponding negative values for in-plane bi-axial strain show the compression of the in-plane lattice parameter a.

4.3.2 Oxygen Partial Pressure

The effect of Oxygen partial pressure was investigated by varying the flow through the OAR ARS during deposition. We have investigated film growth for 0, 1, 3, 5, 7, and 9 sccm during deposition. Examination of the Omega-2Theta curves (normalized and shifted vertically) shown in figure 45 reveals that there is a "sweet spot" that ensures favorable growth kinetics without introducing strain.

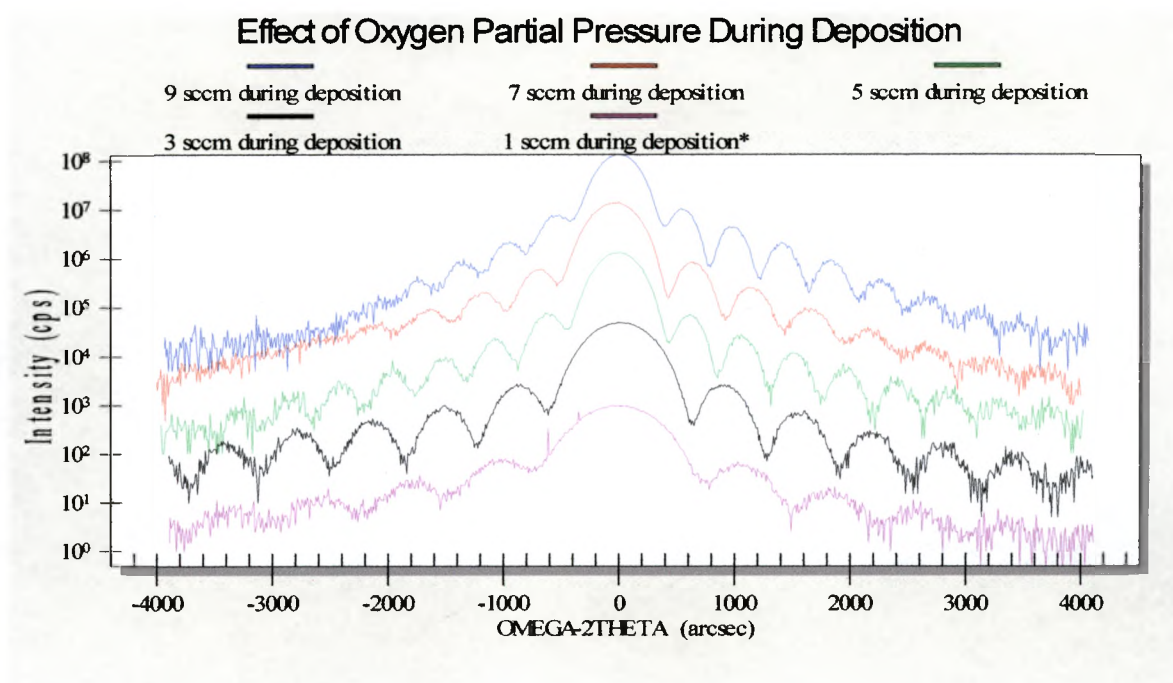


Figure 48: ω - 2θ scan of ZnO (002) for Different O Flow During Deposition

The films deposited with 5, 7, and 9 sccm are 2-3 times more intense than films deposited at lower ambient O pressures. These 3 films show comparable thickness as determined by Peaksplit and XRR (~350 angstroms). It is clear that the film deposited with 5sccm radical oxygen assist has the narrowest FWHM as well as the most symmetric and persistent pendellosung fringes. These observations lead us to define 5 sccm O during deposition as an optimized parameter for intrinsic ZnO film growth.

The next graphic, figure 49, shows the Omega rocking curves (normalized and shifted vertically) for the different O-processed films.

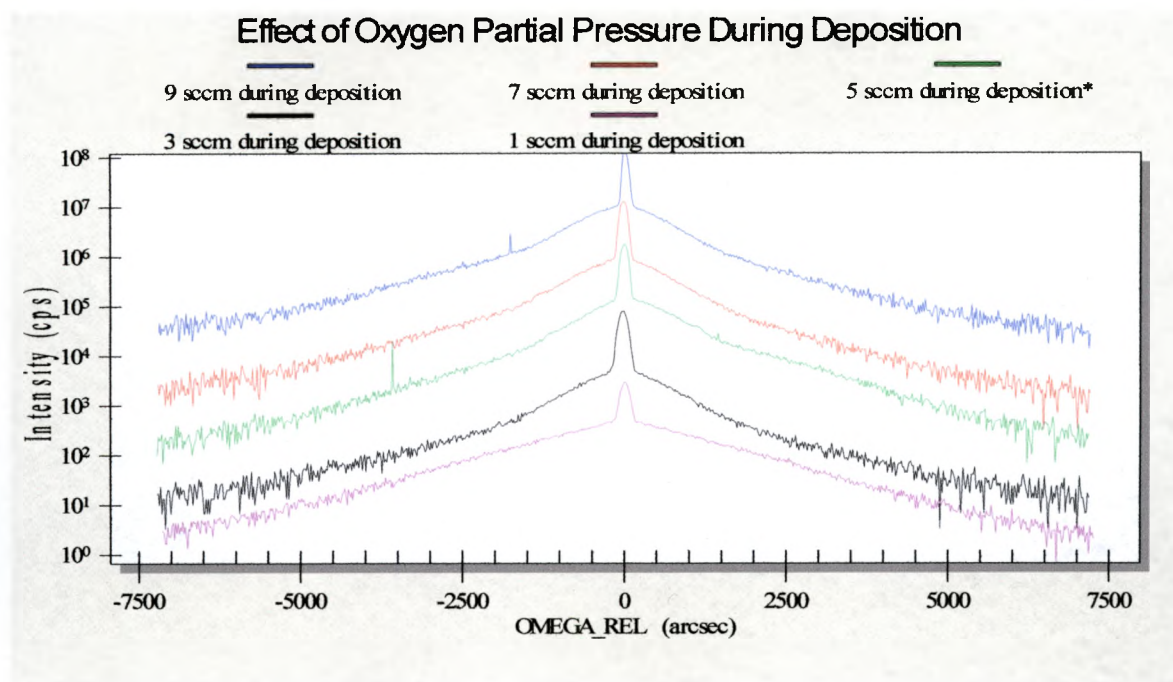


Figure 49: ω -Rocking Curve of ZnO (002) for Different O Flow During Deposition

O ₂ deposition (sccm)	FWHM rocking curve (arcsec)
1	163.1
3	160.8
5	134.7
7	137.1
9	111.3

Table 16: Omega Rocking Curve FWHM for Different O Flow During Deposition

The film deposited at 9sccm O₂ shows the least mosaicity and hence the greatest crystallinity but the asymmetry in its peak is indicative of strain in the film. Also, the peak for the 5 sccm film is >5000 cps higher than the others. Crystallite size for the different O-processed films is shown in table 17.

Sample	Crystallite Size (angstroms)
1 sccm deposition	32.2
3 sccm deposition	32.6
5 sccm deposition	39.1
7 sccm deposition	38.3
9 sccm deposition	47.4

Table 17: Approximate Crystallite Size for Different O Flow During Deposition

The Omega-2Theta comparison, depicted in figure 50, shows the relative position of the ZnO (002) peaks relative to the sapphire (006) substrate peak (normalized and shifted vertically).

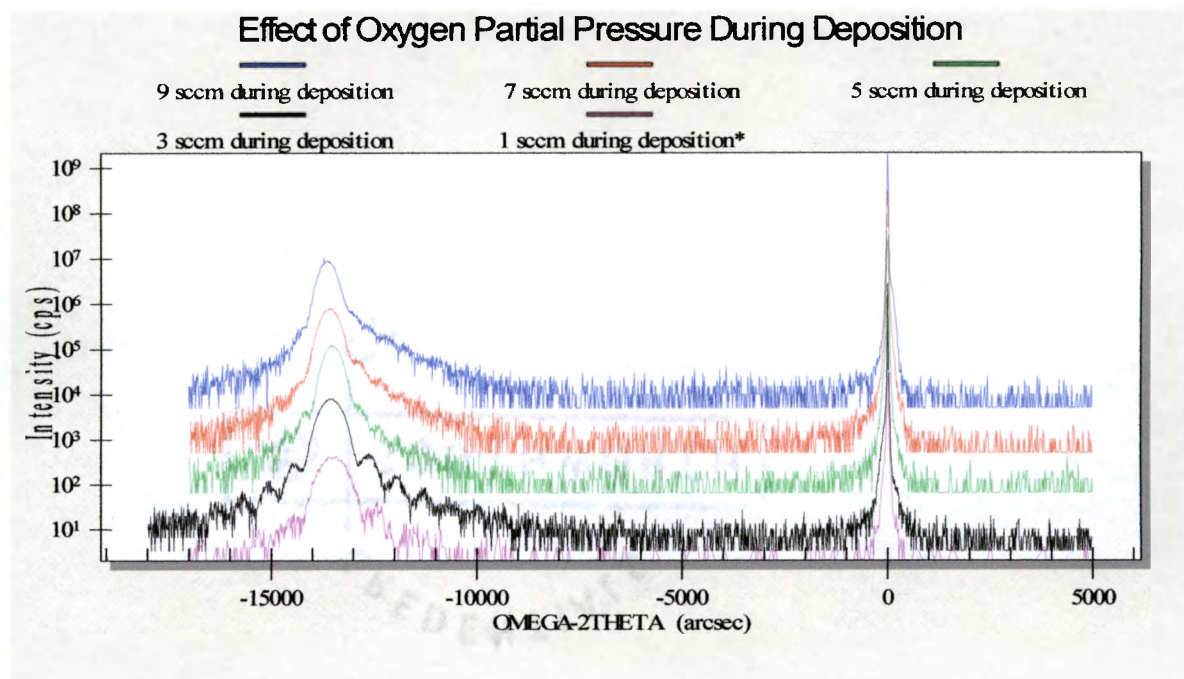


Figure 50: ω - 2θ curves for Different Oxygen Flow During Deposition

Sample (sccm O ₂ during deposition)	ZnO (002) 2Theta position	calculated lattice constant c	ave uniform strain along c-axis (residual strain)	in plane biaxial strain (MPa)
1	34.226	5.235	0.00528	-5.216
3	34.173	5.243	0.00677	-6.687
5	34.161	5.245	0.00714	-7.048
7	34.141	5.248	0.00771	-7.613
9	34.062	5.260	0.00998	-9.849

Table 18: Strain for Different Oxygen Flow During Deposition

Interestingly enough, the sample sputtered with 1 sccm Oxygen shows the least strain for all the films but its fringes are the weakest in the group. Despite this finding, the general trend shows better crystallinity for films processed at higher oxygen flow rates during deposition.

4.3.3 Oxygen Deficient Film

We attempted one last growth for a film that was “oxygen starved” during deposition. This film was cleaned with 5sccm Oxygen radical plasma and deposited at 650 °C for 30 minutes without any process gas. The Omega-2Theta scan for this film is shown in figure 51 along with a film sputtered with 5 sccm radical oxygen during deposition for comparison.

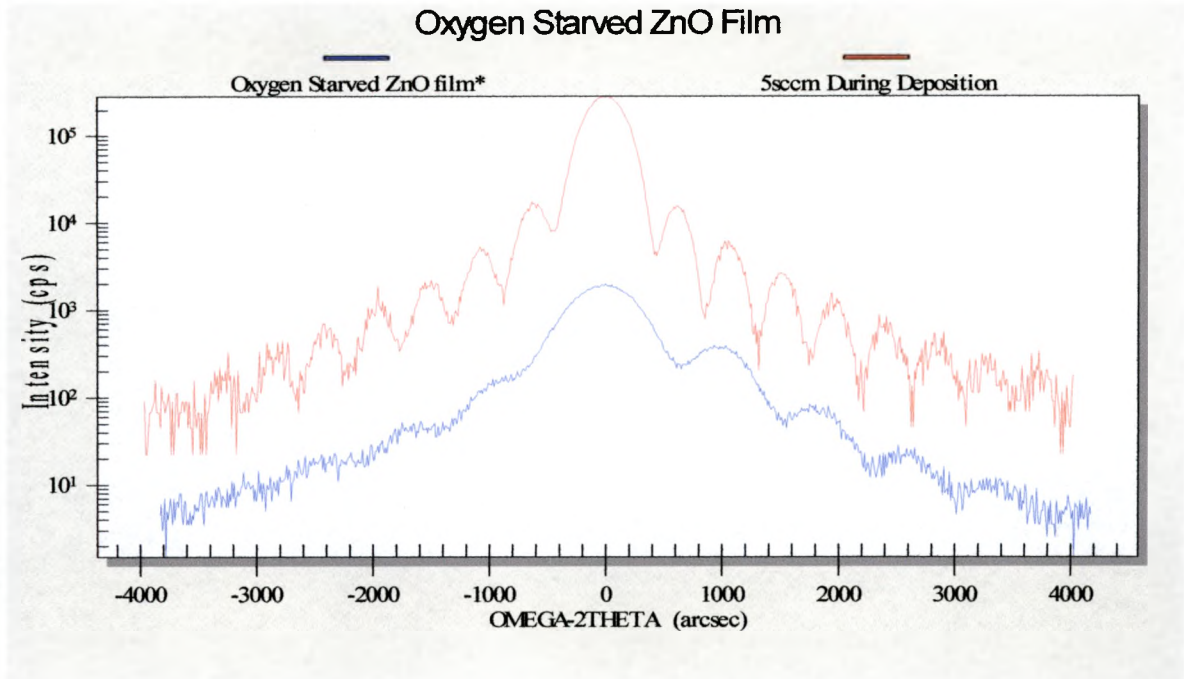


Figure 51: Omega-2Theta scan of ZnO (002) for Oxygen Starved Film

The oxygen deficient film shows very weak satellite peaks whose frequency indicates a much thinner film than one grown in the presence of oxygen. The strain for this film along both the c-axis (tensile) and a-axis (compressive) was exceeded only by that of the film deposited with 9sccm of radial oxygen. Its Omega Rocking curve (not pictured) reveals a FWHM of 157 arcseconds which indicates better crystallinity than films deposited at 1 or 3 sccm Oxygen during deposition but with a comparable crystallite size.

4.3.4 Deposition Temperature

Deposition temperature has profound effects on all aspects of growth kinetics and epilayer properties. We chose to follow the lead of researchers in the literature and use high temperature deposition in order to achieve the best crystal quality. In doing so, we limited our capability to characterize many of our films due to a reduction in the deposition rate. ZnO films were grown at 450, 550, and 650 degrees Celsius (723K, 823K, and 923K respectively) under the previously optimized conditions of 5 sccm

radical cleaning and 5 sccm O during deposition. Figure 52 shows a comparison with the standard modifications to aid interpretation.

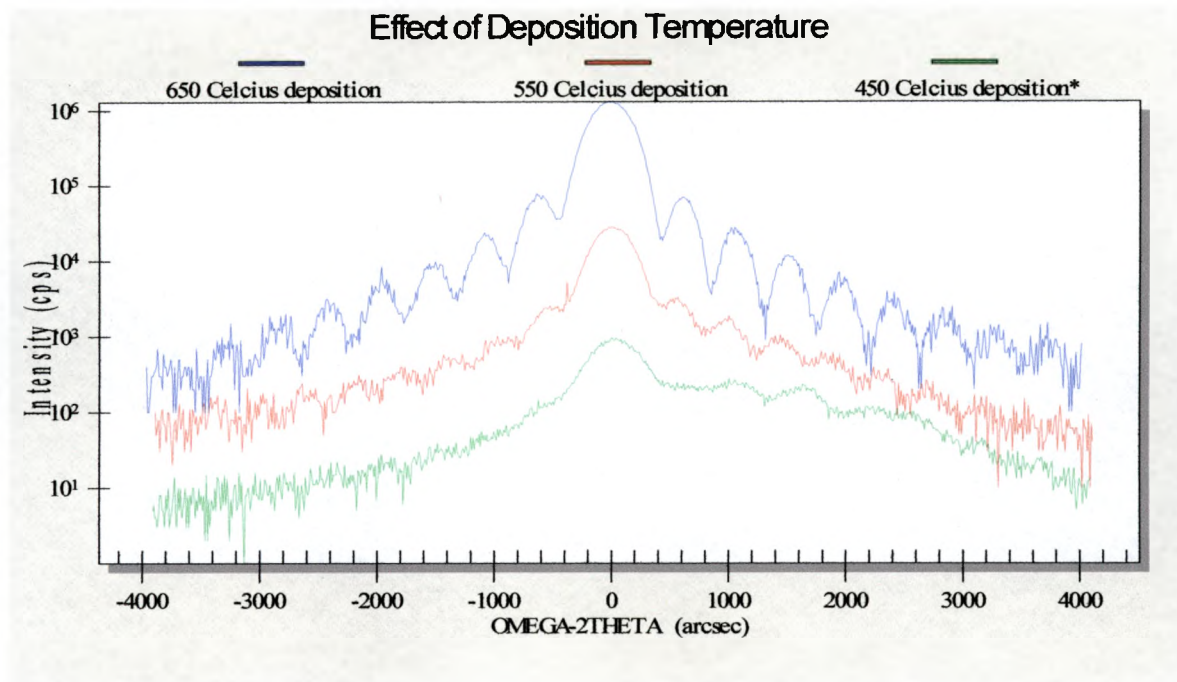


Figure 52: ω - 2θ scans of ZnO (002) for Different Processing Temperatures

Clearly, a higher deposition temperature more favorably maintains the epitaxial growth of ZnO. The film deposited at 650 degrees C is more intense by 10,000 cps than the other two films in addition to exhibiting persistent and symmetric pendellosung fringes.

Figure 53 shows the normalized peaks for the Omega rocking curves of the films. One important note here is that I've left the intensities unmodified so that the reader can appreciate (especially in log scale) the radical difference in intensity as a function of temperature.

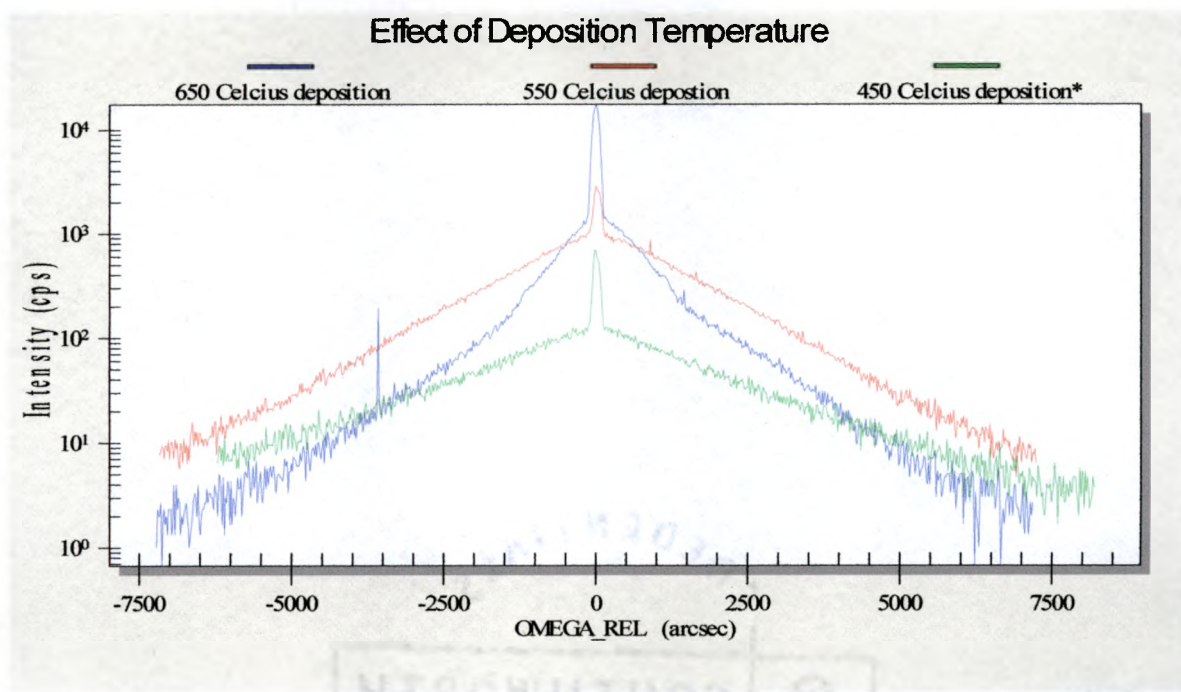


Figure 53: ω -Rocking Curve of ZnO (002) for Different Processing Temperatures

The FWHM of the central peak for the 650 film and the 450 film are very close (~ 135 arcseconds). This may mean that once the growth transitioned to 3D island nucleation, the two films exhibited similar crystallinity. However, from the data one can easily see that the secondary shallow peak for the 450 film is much broader, indicating poorer crystallinity and mosaicity in the bulk of the film. Crystallite size was calculated for the different films shown in table 19.

Sample	Crystallite Size (angstroms)
650 $^{\circ}$ C Deposition	39.1
550 $^{\circ}$ C Deposition	30.6
450 $^{\circ}$ C Deposition	39.1

Table 19: Crystallite Size for Different Process Temperatures

Figure 54 shows a drastic shift toward lower angle for the ZnO (002) peak due to elongation of the c-axis.

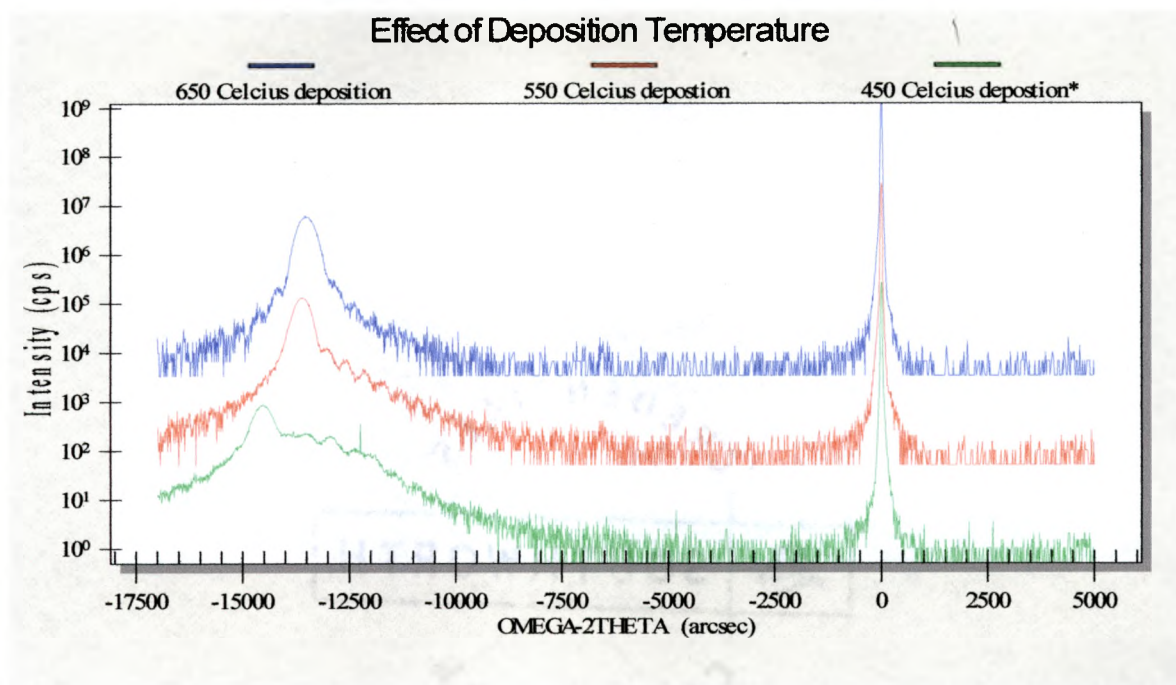


Figure 54: ω - 2θ curves for Different Processing Temperatures

The strain in the system is evident from the loss of symmetry in the satellite fringes as well as the progressive shift toward lower angle. The strain calculations are shown in table 20 below.

Sample	ZnO (002) 2Theta position	calculated lattice constant c	ave uniform strain along c- axis (residual strain)	in plane biaxial strain (MPa)
650	34.161	5.245	0.00714	-7.048
550	34.126	5.250	0.00813	-8.022
450	33.621	5.327	0.0228	-22 530

Table 20: Strain for Different Processing Temperatures

As expected, the film processed at higher temperature shows the least strain.

4.3.5 Buffer Layers

Introduction of a buffer layer is a common tactic used to coerce a film to grow epitaxially along a specific direction. We have explored the use of ZnO (homoepitaxial) and MgO (heteroepitaxial) buffer layers on sapphire.

Figure 55 shows the normalized and shifted Omega-2Theta curves for three different attempts at using ZnO as a buffer layer. Low temperature (LT) buffer layers were deposited at 350 and 450 degrees Celsius followed by the standard 30 min deposition of ZnO at 650 degrees Celsius with 5sccm Oxygen radical process gas. In order to follow up on a suggestion from the literature, we have also attempted to deposit a high temperature (HT) buffer layer at 650 °C followed by a 30 minute sputter at 350 °C.

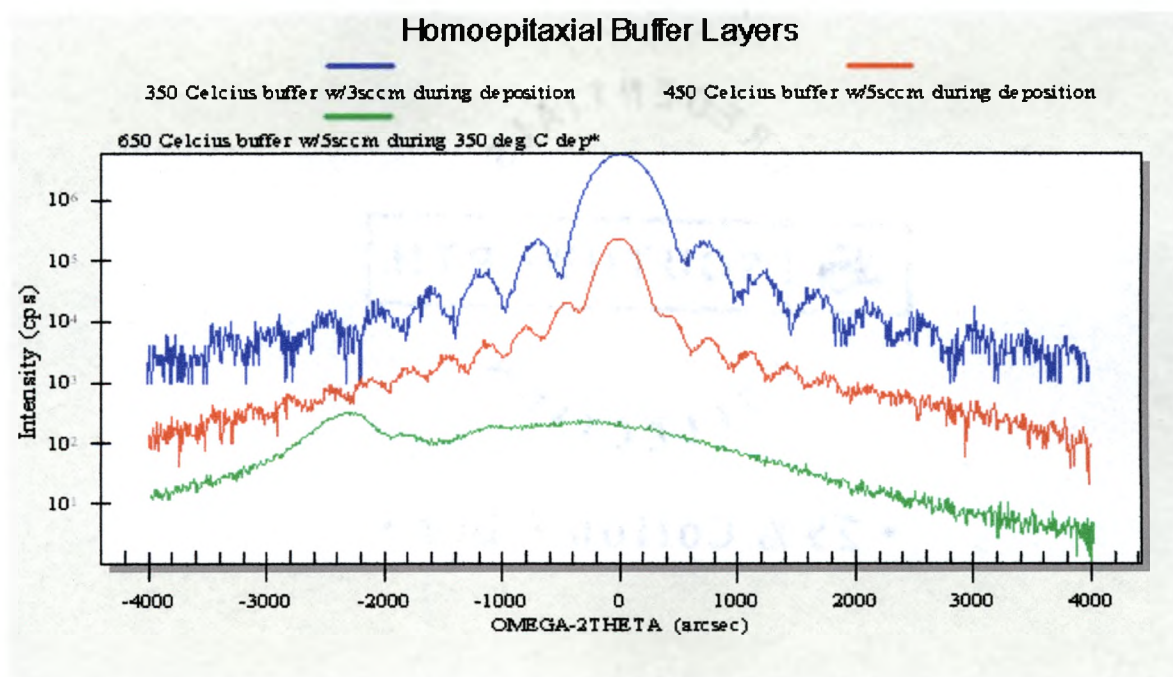


Figure 55: ω - 2θ scans of ZnO (002) for Different Homoepitaxial Buffer Layers

The LT buffer layers are clearly superior to the HT buffer layer. The buffer deposition at 450 exhibits less symmetric pendellosung fringes but their increased frequency is

indicative of a thicker film. Figure 56 shows a normalized set of Omega rocking curves with actual intensity units.

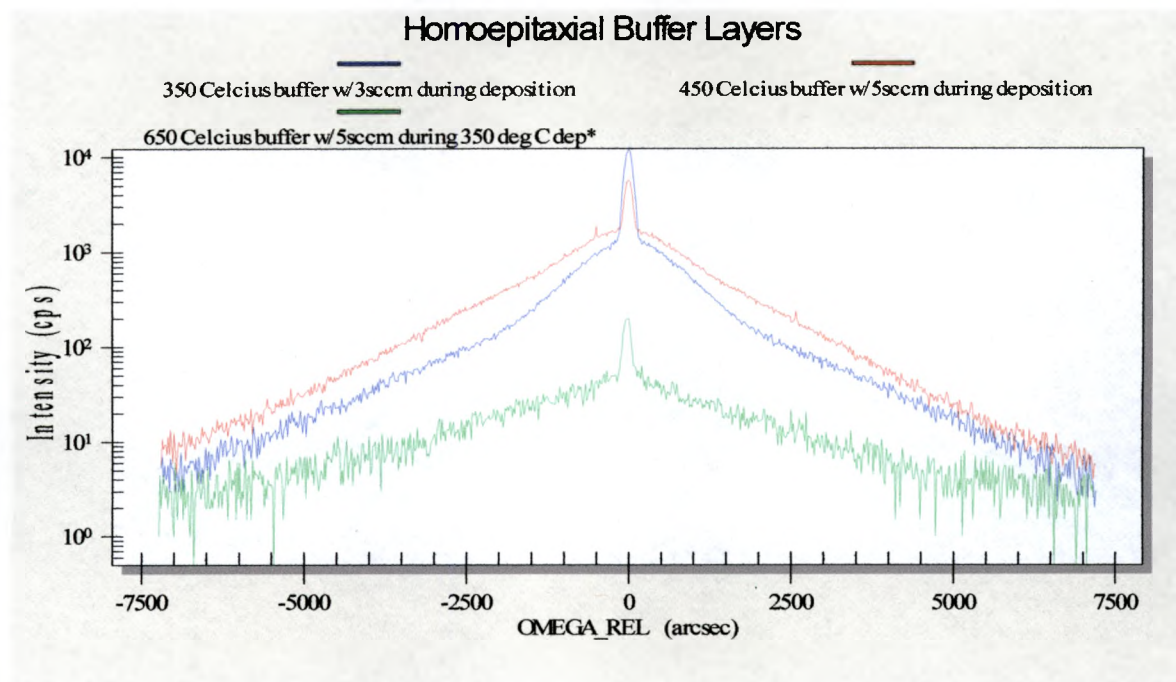


Figure 56: ω -Rocking Curves for Different Homoepitaxial Buffer Layers

It would appear that the lower temperature buffer layer actually results in improved crystallinity for the film as evidenced by the narrower and more intense central peak. The crystallite sizes for these samples are very near those for ZnO films without buffer layers (32-34 angstroms). The profiles of the broad components for the 350 and 450 °C buffer layers also suggest that well ordered layers are better defined for the lower temperature buffer layer sample. This could be explained in terms of the strain relaxation mechanism that a buffer layer provides. Buffer layers of ZnO deposited on Al₂O₃ at low temperatures should be rough and porous. This allows them to absorb much of the strain due to lattice mismatch at the interface. The eventual relaxation of the buffer layer reduces the strain and results in a higher defect density. When the second ZnO deposition encounters this surface, it sees a much more favorable template for epitaxial

growth and proceeds to grow in 2D mode with little or no strain. It is possible that a buffer layer deposited at 450 degrees does not provide a comparable template because it forms a more ordered crystalline layer that cannot fully relax to relieve lattice mismatch induced strain.

Strain calculations are made possible by noting the positions of the ZnO (002) peaks relative to the sapphire substrate as shown in figure 57.

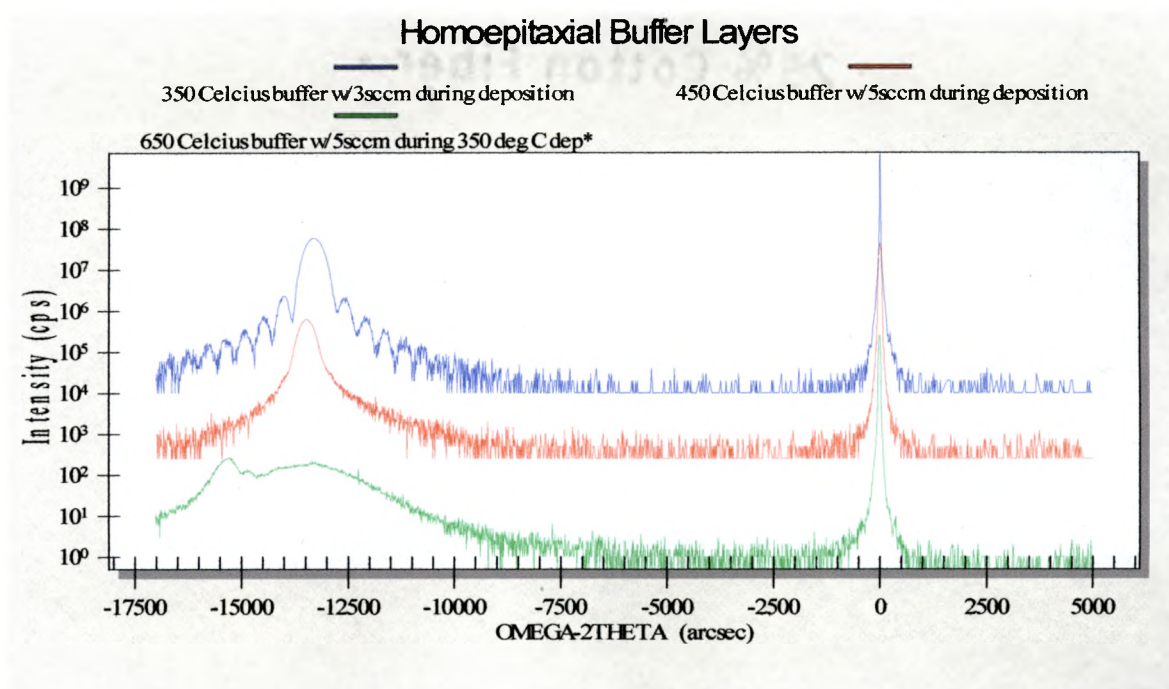


Figure 57: ω - 2θ curves for Different Homoepitaxial Buffer Layers

Sample	ZnO (002) 2Theta position	calculated lattice constant c	ave uniform strain along c- axis (residual strain)	in plane biaxial strain (MPa)
350 LT	34.278	5.228	0.00380	-3.749
650 HT	33.182	5.395	0.0360	-35.50
450 LT	34.203	5.239	0.00593	-5.857

Table 21: Strain for Different Homoepitaxial Buffer Layers

As predicted, the 350 LT buffer layer exhibits the least strain because the initial rough layer helps alleviate lattice mismatch and allows the subsequent epilayer to improve both adherence and nucleation. There is also the clear presence of symmetric and persistent satellite peaks for the 350 compared to the 450 LT buffer samples.

The use of MgO as a heteroepitaxial buffer layer did not improve the crystallinity of our ZnO films. The first attempt employed a buffer layer of Mg on an Oxygen terminated Al_2O_3 surface. The Mg target was sputtered at 15 mA beam current for one minute at 650°C . The subsequent ZnO layer was then deposited for 30 minutes at 25 mA with 3 sccm Oxygen flowing through the OAR ARS. Henceforth, I shall refer to this sample as MgO buffer 1. The second attempt, MgO buffer 2, consisted of a 5 min sputter of the Mg target at 25 mA with 5 sccm radical Oxygen at 650°C followed by a standard ZnO deposition (30 min, 5 sccm O, 25 mA, 650°C). The Omega-2Theta curves (normalized and vertically shifted) for these samples are shown in figure 58.

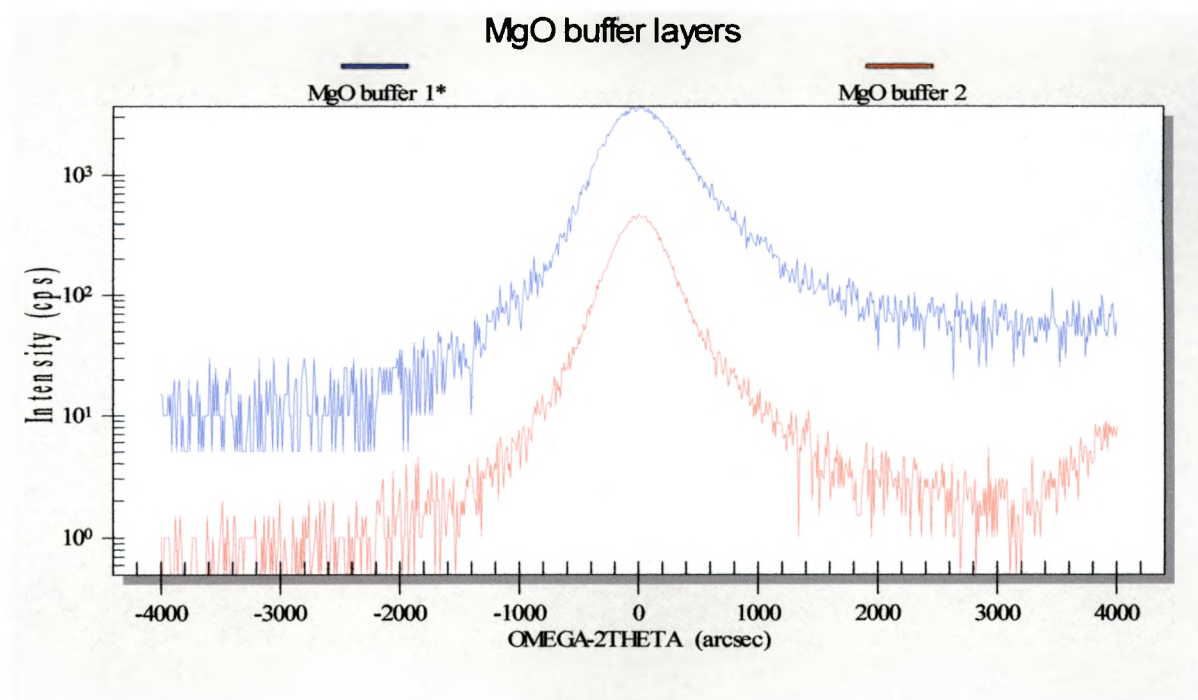


Figure 58: Omega-2Theta scans of MgO buffer layered ZnO (002)

The sample previously designated MgO buffer 2 shows a narrower FWHM indicative of greater thickness, but neither film comes close to the quality of the other undoped ZnO samples. The omega rocking curves for both samples show no central peak and have FWHM on the order of degrees. This extremely broad rocking curve results in a calculated crystallite size on the order of 1 angstrom which is not physically meaningful. The Omega-2Theta curves shown in figure 59 (normalized to Al_2O_3 (006) and vertically shifted for clarity) allow for the calculation of film strain.

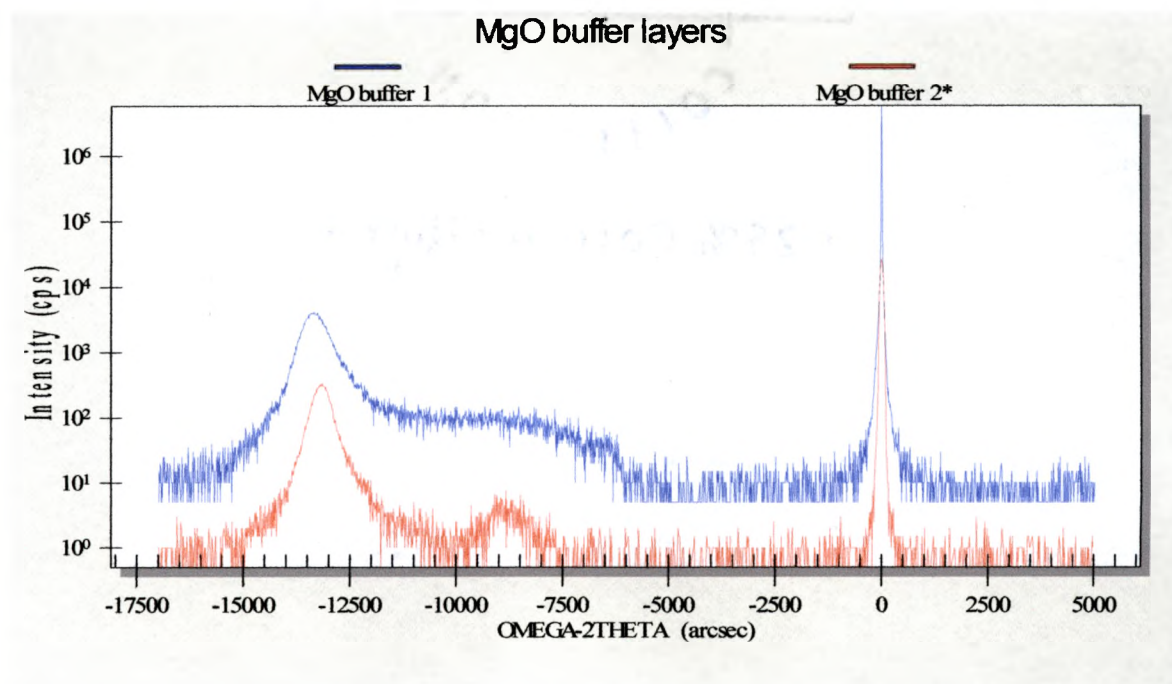


Figure 59: Omega-2Theta Curves for MgO Buffer Layer Samples

Sample	ZnO (002) 2Theta position	calculated lattice constant c	ave uniform strain along c- axis (residual strain)	In plane biaxial strain (MPa)
MgO buffer 1	34.26722222	5.22914103	0.00409747	-4.045334626
MgO buffer 2	34.37555556	5.213156564	0.00102814	-1.015057953

Table 22: Strain for MgO Buffer Layer Films

Strangely enough, the MgO buffer 2 film shows the least strain for any of the Phase 1 (undoped films). One can see the emergence of a strained MgO (111) peak near 36.7 degrees. The minimized strain is an interesting result, but the lack of satellite peaks and the unimpressive Omega Rocking Curve FWHM (1-2 degrees) lead me to believe that the reports of MgO buffer layers in the literature are somewhat incomplete. In order to verify the usefulness of an MgO buffer, we also deposited ZnO on MgO (100) and MgO (111) substrates. The 2Theta-Omega scans for these different substrates are shown in figure 60.

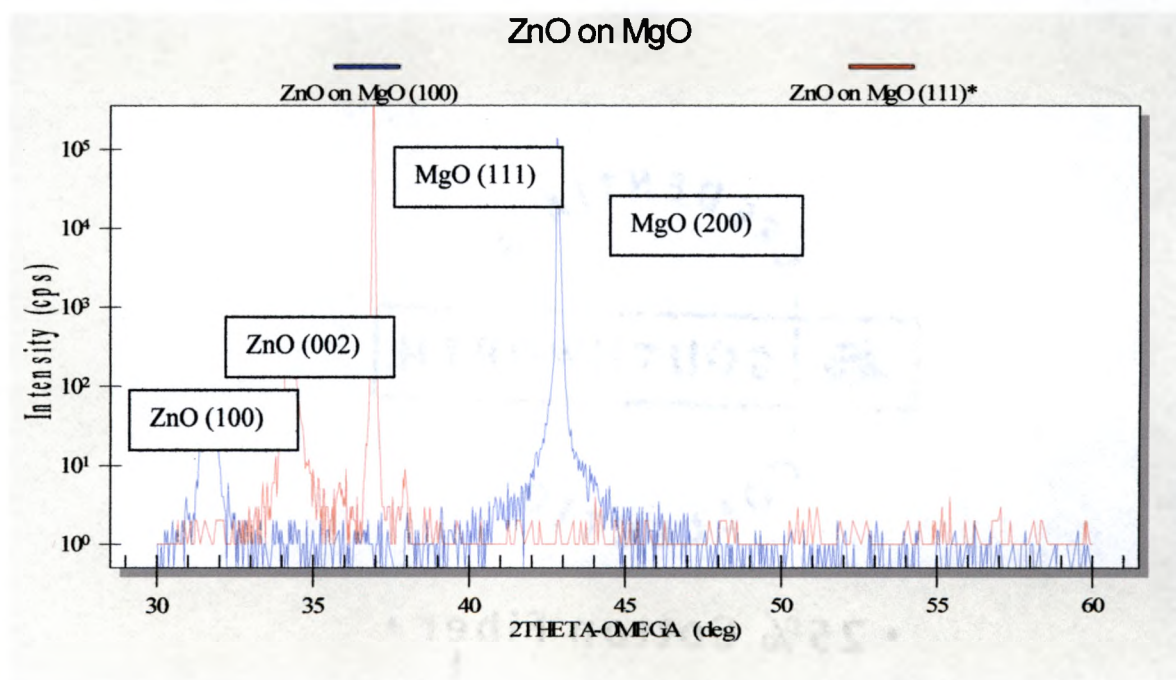


Figure 60: 2Theta-Omega scan of ZnO on MgO

The positions and identification of substrate and epilayer peaks reveals the lattice matching between ZnO and MgO. When ZnO is sputtered onto the MgO (h00) template, the subsequent film growth is oriented in the 100 direction. If MgO (111) is used as a substrate, the resulting ZnO film grows along the familiar (002) direction. While this is all very interesting, the promise of excellent film quality through the use MgO buffer

layers has not been realized. The lack of satellite fringes, relatively low peak intensity, and large FWHM do not inspire any hope for optimization of ZnO processing via this particular heteroepitaxial buffer layer. Perhaps there is some degree of anneal required after deposition of the buffer layer but before epilayer growth to activate or “wet” the sapphire surface. Yet another possibility is a mixed phase $Mg_xZn_{(1-x)}O$ phase at the interface responsible for the decrease in strain that has yet to be identified. Attempts have been made to contact the corresponding authors of research detailing the use of such buffer layers but there was no response before the finalization of this document.

4.3.6 N-type and P-type ZnO

Initial attempts at producing doped ZnO met with resistance due to the difficulty of introducing an interstitial species into Zn or O sites within the lattice. The optimized processing conditions for undoped ZnO did not produce highly crystalline films. We have concluded that a buffer layer is necessary to promote epitaxial growth of doped ZnO films because the n and p type attempts without a buffer layer were extremely thin and showed no signs of crystallinity. We feel that this is due to complicated reaction kinetics at the substrate surface. Instead of ZnO aligning itself with the sapphire Oxygen sublattice, competing reactions with Ga and/or N inhibit domain matching epitaxy. Consequently, a buffer layer should make the formation of doped epilayers much more favorable. One simply cannot expect nature to accommodate such a drastic change in growth kinetics (due to the introduction of additional atomic species) at the substrate interface without providing a better template in the form of a ZnO buffer layer. The buffer layer consisted of ZnO deposited on the surface of 5sccm Oxygen plasma treated sapphire for 30 minutes at 25mA, 650 °C, and 5sccm radical oxygen process gas. The

film designated “Ga:ZnO” was grown under the same conditions as the buffer layer using a target that contained 1.5%(atomic) Ga_2O_3 . Hereafter we shall refer to the film grown from the Ga-doped ZnO target under standard conditions with 3sccm O and 2sccm N radical process gases as “Ga/N:ZnO”. Figure 61 shows the Omega-2Theta curves for our best attempts at n-type (Ga doped) and p-type (Ga/N Codoped) films along with the buffer layer for comparison.

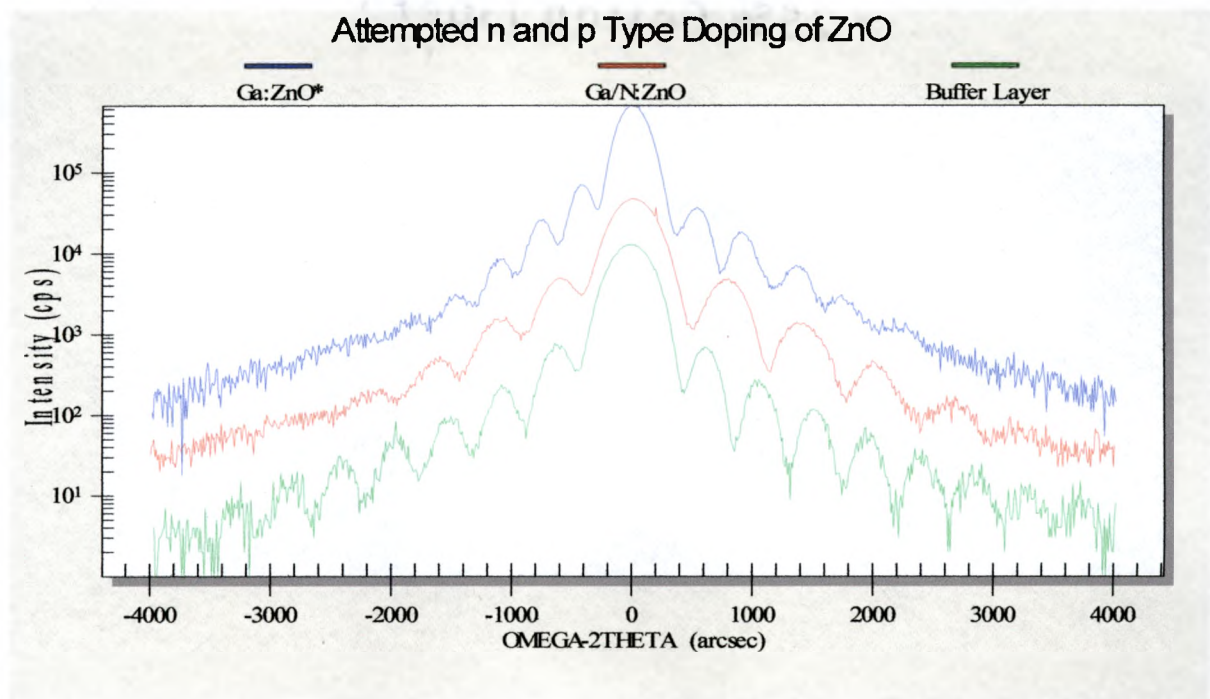


Figure 61: Omega-2Theta Curves of ZnO (002) for Ga:ZnO and Ga/N:ZnO

Both doped films exhibit pendellosung fringes indicating that there is regularity in the c-axis lattice parameter. The spacing of the fringes for the Ga:ZnO film exhibit a greater frequency implying that the film is thicker than the buffer layer but the decay of the fringes tells me that the top layer has a more strain and possible greater defect density than the buffer layer. The Ga/N: ZnO film also shows satellite peaks but the frequency matches those of the buffer layer. This means that the top layer we tried to grow is extremely thin due to more complicated growth kinetics.

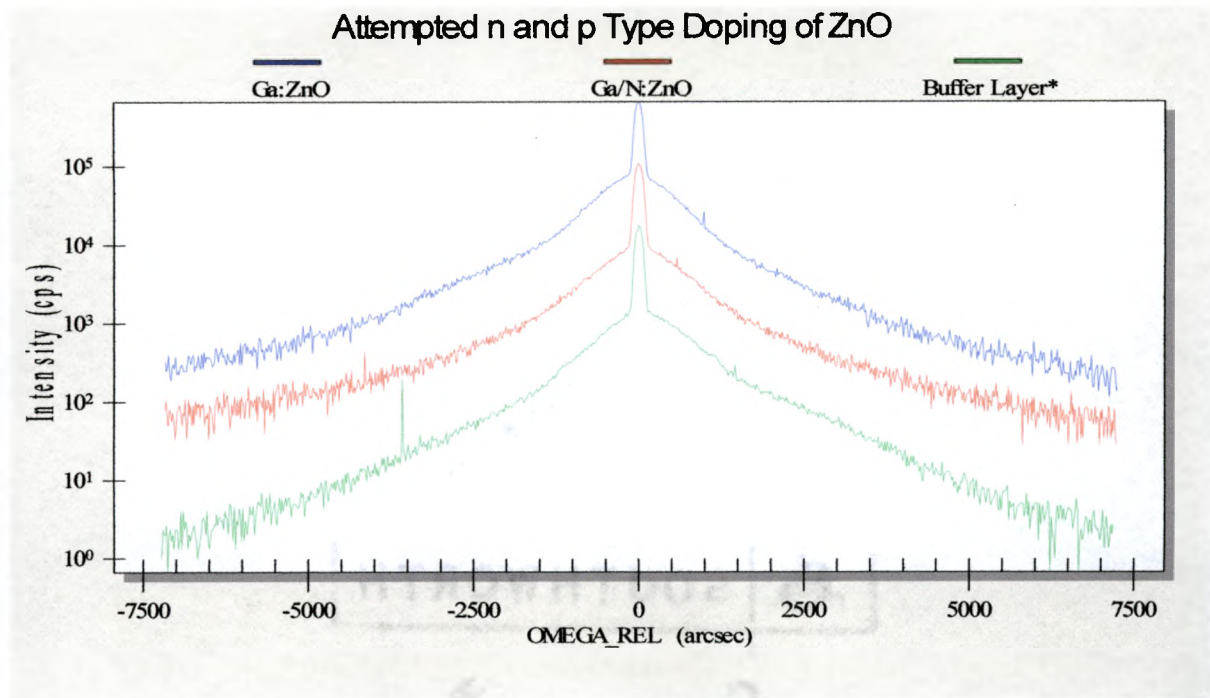


Figure 62: Omega Rocking Curves of ZnO (002) for Ga:ZnO and Ga/N:ZnO

The Ga:ZnO film shows essentially the same degree of crystallinity as the buffer layer with only a slight increase (3.1") in the FWHM of the Omega rocking curve. This implies that the buffer layer provided an excellent template for doped ZnO film growth. Further analysis of thicker films with SIMS or XRF will reveal the stoichiometry of the doped layer. The FWHM of the Ga/N:ZnO film is 151". This slight broadening corresponds to a decrease in the crystallite size from 39.1 to 34.7 angstroms.

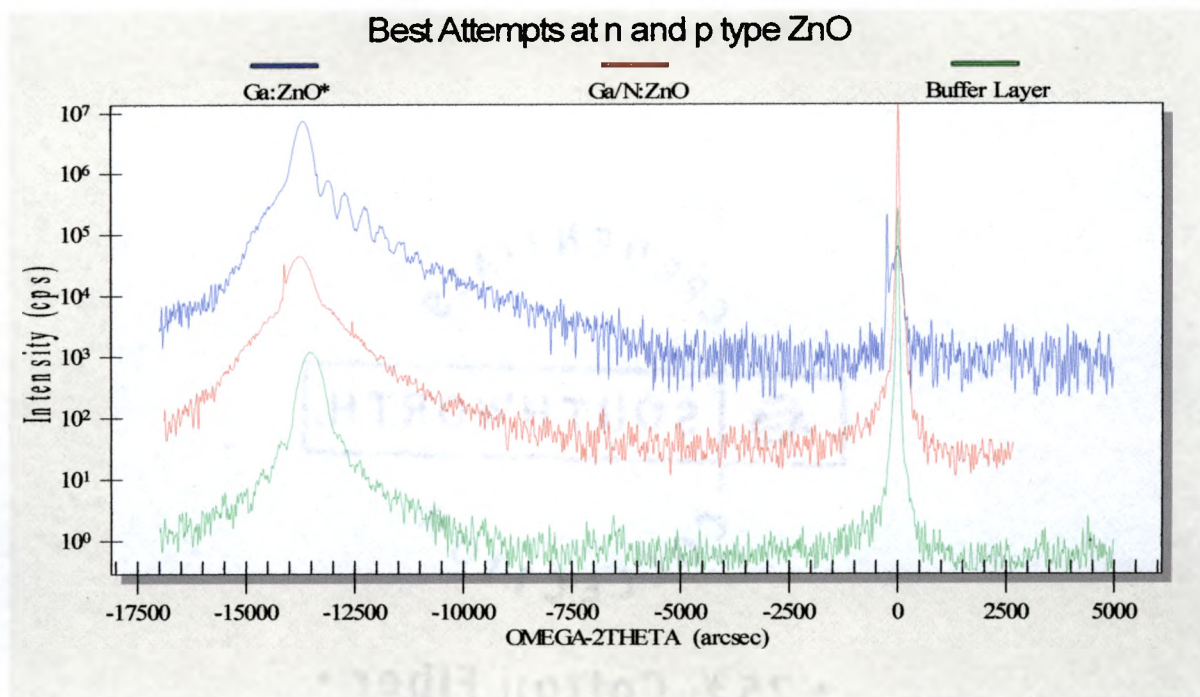


Figure 63: Omega-2Theta Curves for Ga:ZnO and Ga/N:ZnO

Sample	ZnO (002) 2Theta position	calculated lattice constant c	ave uniform strain along c- axis (residual strain)	In plane biaxial strain (MPa)
Ga ZnO	34.079	5.257	0.00948	-9.360
Ga/N:ZnO	34.034	5.264	0.0108	-10.623

Table 23: Strain for Best Attempts at n and p Type ZnO

Introducing dopant species into the ZnO crystal lattice intensifies the tensile stress along the c-axis and compressive stress along the a-axis compared to the undoped films.

Further manipulation of the buffer layer may mitigate this effect.

4.3.7 Mn Doped ZnO

We fabricated 5 samples of Mn doped ZnO in hopes of attaining films that exhibited room temperature ferromagnetic behavior. The films were sputtered using targets containing 23.5% (atomic) MnO. Predictions in the literature suggest that the double exchange mechanism necessary for ferromagnetic Transition Metal (TM) doped

ZnO only manifests itself when there are sufficient carriers available to mediate the spin symmetry of the TM ions in the crystal lattice. With this premise in mind, we sputtered films with Ga and N as dopants to increase the carrier density. The reader should note the following designations:

Sample Designation	Target Material	Process Gas
Mn:ZnO (400 °C dep)	ZnO/MnO _(23.5)	5 sccm Oxygen Radicals
Mn:ZnO (650 °C dep)	ZnO/MnO _(23.5)	5 sccm Oxygen Radicals
Mn/N:ZnO	ZnO/MnO _(23.5)	5 sccm Nitrogen Radicals
Mn/Ga:ZnO	ZnO/MnO _(23.5) /Ga ₂ O _{3(1.5)}	5 sccm Oxygen Radicals
Mn/N/Ga:ZnO	ZnO/MnO _(23.5) /Ga ₂ O _{3(1.5)}	5 sccm Nitrogen Radicals

Table 24: Sample Designations for Mn Doped ZnO Films

None of these samples showed any indication of pendellosung fringes and only Mn/N/Ga:ZnO, Mn/Ga:ZnO, and Mn:ZnO (650 °C dep) exhibited Omega Rocking curve FWHM comparable to the undoped ZnO films. The Omega-2Theta curves for the Mn doped films are shown in figure 64 followed by strain calculations in table 25.

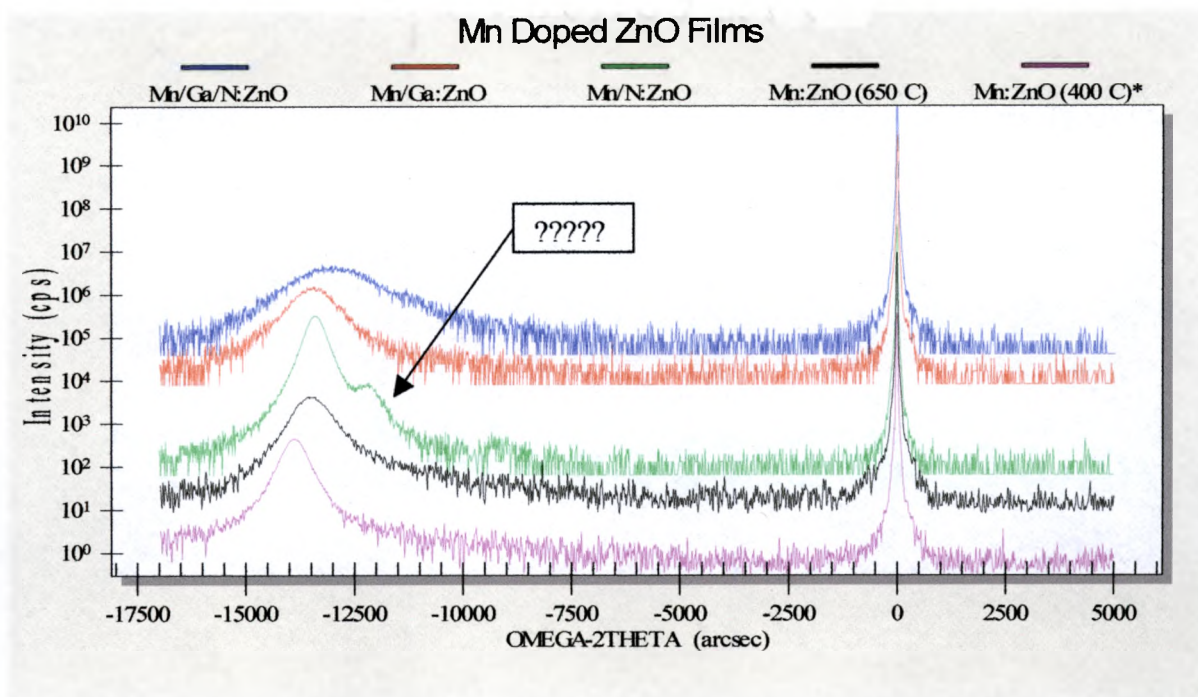


Figure 64: Omega-2Theta Curves for Mn Doped ZnO Films

Sample	ZnO (002) 2Theta position	calculated lattice constant c	ave uniform strain along c-axis (residual strain)	In plane biaxial strain (MPa)
Mn/N/Ga:ZnO	34.319	5.222	0.00263	-2.598
Mn/Ga:ZnO	34.204	5.238	0.00589	-5.810
Mn/N:ZnO	34.237	5.234	0.00495	-4.888
Mn:ZnO (650 °C)	34.152	5.246	0.00739	-7.299
Mn:ZnO (400 °C)	33.975	5.273	0.0125	-12.32

Table 25: Strain for Mn Doped ZnO Films

The conspicuous peak near $2\theta = 35^\circ$ present in the Mn/N:ZnO (shown in green) film may be a strained Manganese Nitride phase. The only hexagonal form I could find exists as Mn_6N_2 (quite an oddball) with a diffraction peak for the (110) plane near $2\theta = 36^\circ$.

Another possible identity is a cubic Zinc Nitride phase. The (321) plane for this material shows a diffraction angle of $2\theta = 34.3^\circ$. Neither of these two systems seems

thermodynamically feasible so further analysis of the peak is required to determine its

identity. In any case, it is a most unwelcome guest as we were trying to create epitaxial Mn doped ZnO.

4.4 Phi Scans

When scanning a Miller plane that is not parallel to the substrate, one must consider that a rotation of the crystal in the plane of the substrate may be necessary to produce the required Bragg condition for diffraction. A scan over a full 360 degrees in the plane of the substrate, also called a phi scan, results in a series of reflections at specific intervals due to the symmetry of the crystal. Conducting this type of scan is somewhat difficult because the intensity of asymmetric peaks is typically rather low, the peaks are not easily located, and the scans take several hours to complete. The procedures for calculating the expected position of an asymmetric peak and performing a phi scan are detailed in the appendix. For figures 65 and 66 (smoothed and shifted vertically for clarity), I have used phi scanning to show the relationship between the (012) plane of sapphire and the (012) plane of ZnO. The orientation of the substrate and epilayer result in striking graphical representations of the 3-fold symmetry for the sapphire plane and 6-fold symmetry of the ZnO plane. Their regular spacing and position relative to one another are one of the most convincing arguments I can provide for the epitaxial nature of these films. It is also important to note that this symmetry is maintained whether or not the sapphire surface was exposed to Oxygen Radical Plasma prior to deposition.

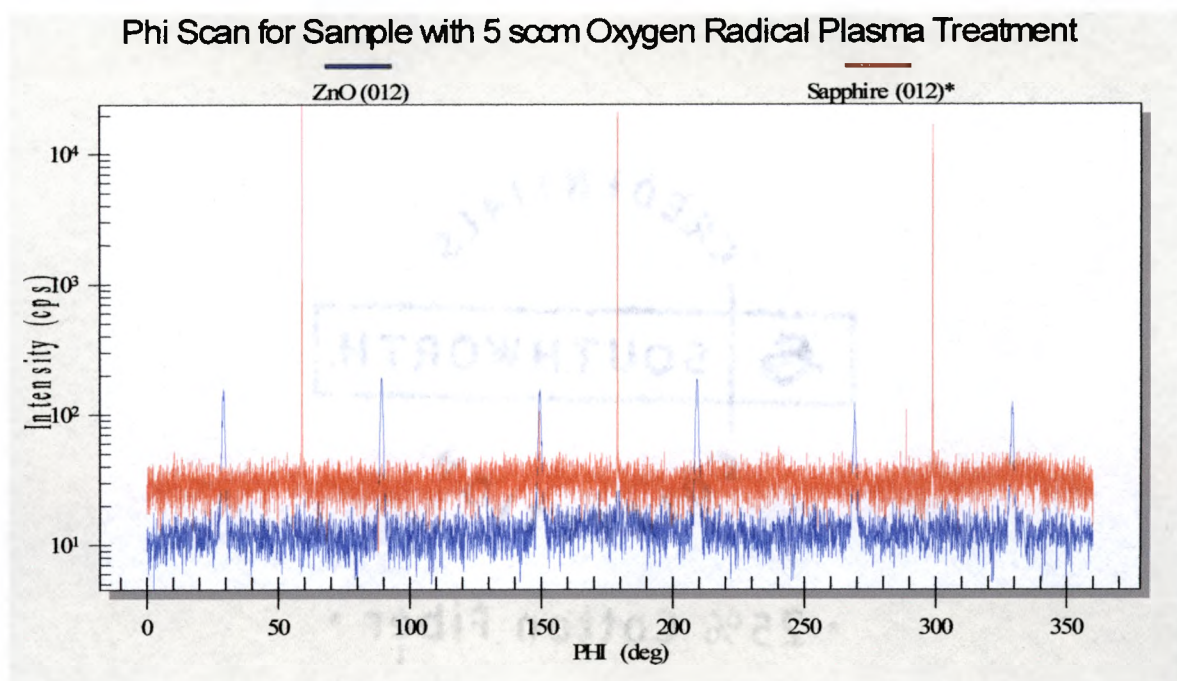


Figure 65: Phi Scan for Sample Exposed to 5 sccm O Radical Plasma Treatment

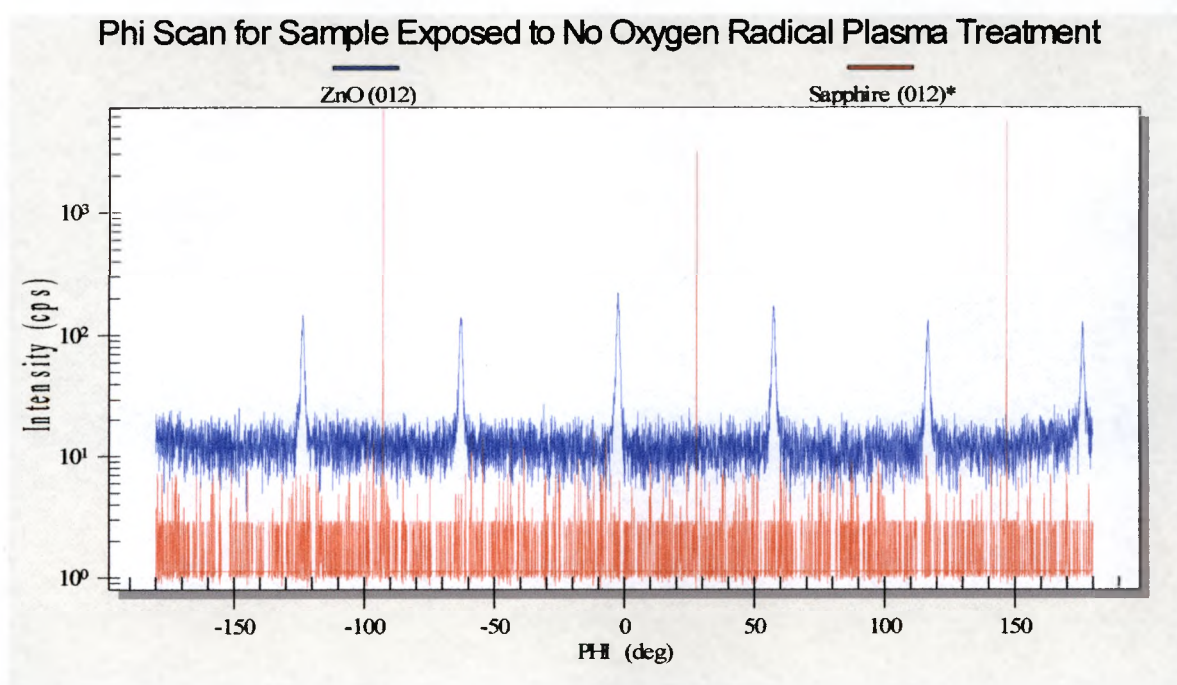


Figure 66: Phi Scan for Sample Exposed to No O Radical Plasma Treatment

4.5 Reflectivity (XRR) Data

Reflectivity scans were performed at shallow angles of an Omega-2Theta scan from 0 to 8000 arcseconds. The data was then modeled using REFS version 3.5b. The most obvious and simplest model to try would consist of a single layer of ZnO on sapphire. For the following discussion, I have considered the sample 040430: 3sccm plasma treatment, 1 sccm O during deposition, 650 °C. The single layer model produced the fit shown in figure 67.

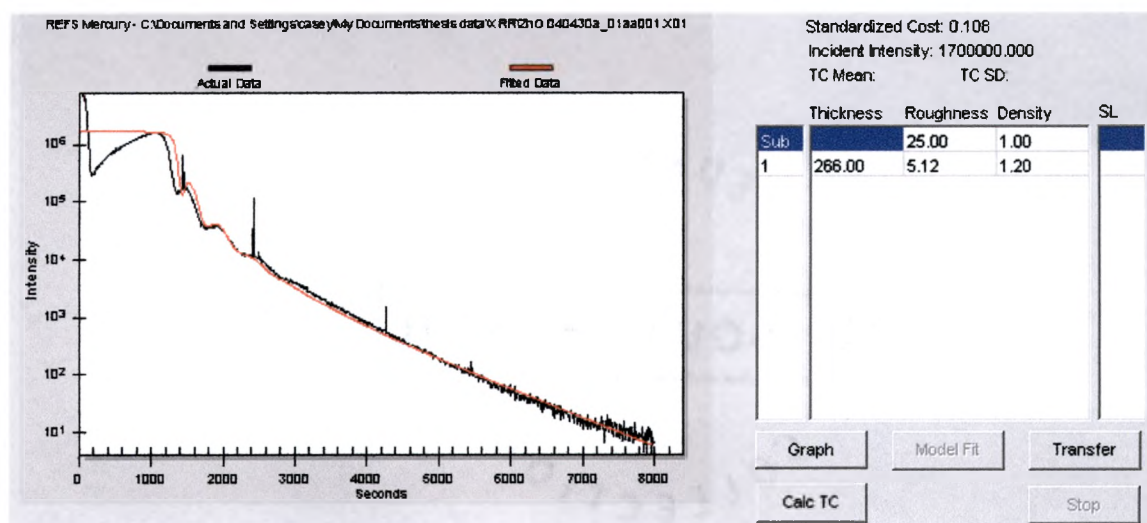


Figure 67: Single Layer Model Fit for REFS v3.5b

Unfortunately, this model did not converge very well as evidenced by the Standardized Cost (a measurement for goodness of fit in arbitrary units) and it also suggests that the ZnO layer is 20% more dense than the bulk. This implies that the film is extremely Zn rich though the stoichiometry of our ceramic target renders this possibility unlikely. Perhaps there is some sort of variation at the substrate interface that we are not taking into account? The follow up model consists of 2 layers and is shown in figure 68.

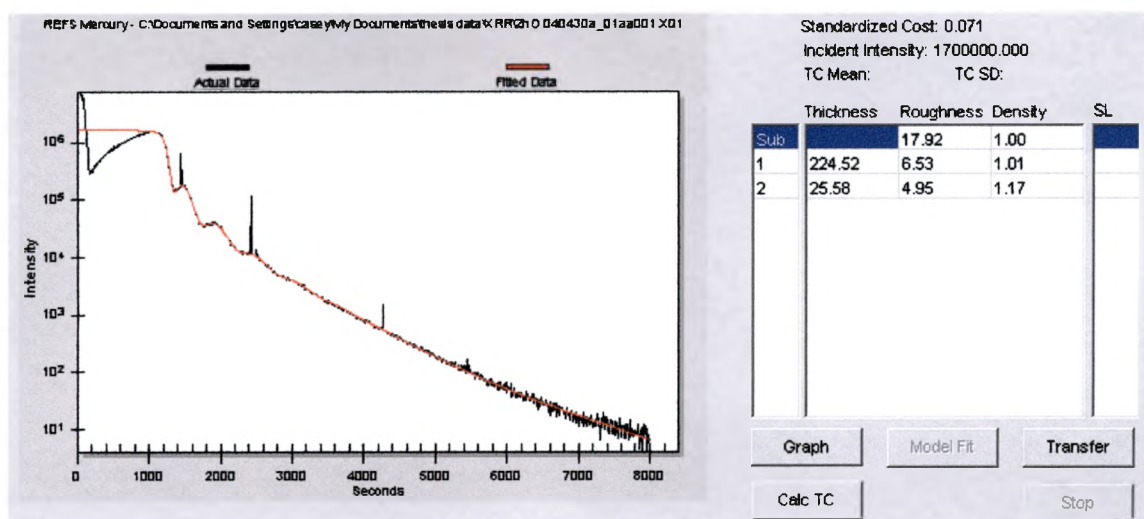


Figure 68: Double Layer Model Fit for REFS v3.5b

This model produces a much better fit, but now it suggests that a very thin dense layer resides at the surface. I can think of no physical justification for an extremely Zn rich or contaminated layer at the surface. Hence, I tried examining the system with a 3-layer model only to have it report the presence of an identical dense surface layer. It then occurred to me that there may be some interdiffusion occurring at the sapphire substrate interface. There have been suggestions, albeit at much higher temperatures, regarding the possible formation of the spinel Ghanite ($ZnAl_2O_4$) at the sapphire/ZnO interface. Perhaps the flux of energetic Ar atoms reflected from the target, appreciable numbers of radical oxygen species, and high vacuum contributed to the formation of such a phase. However, a model including this possibility did not eliminate the presence of the dense surface layer. In desperation, I contacted a representative at Bede Incorporated, Kevin Matney, to seek his advice. He suggested that because the sample had been exposed to atmosphere when removed from the sputtering chamber, there may be a very thin layer of moisture and other airborne contaminants on the surface. The subsequent low density top layer model is shown in figure 69.

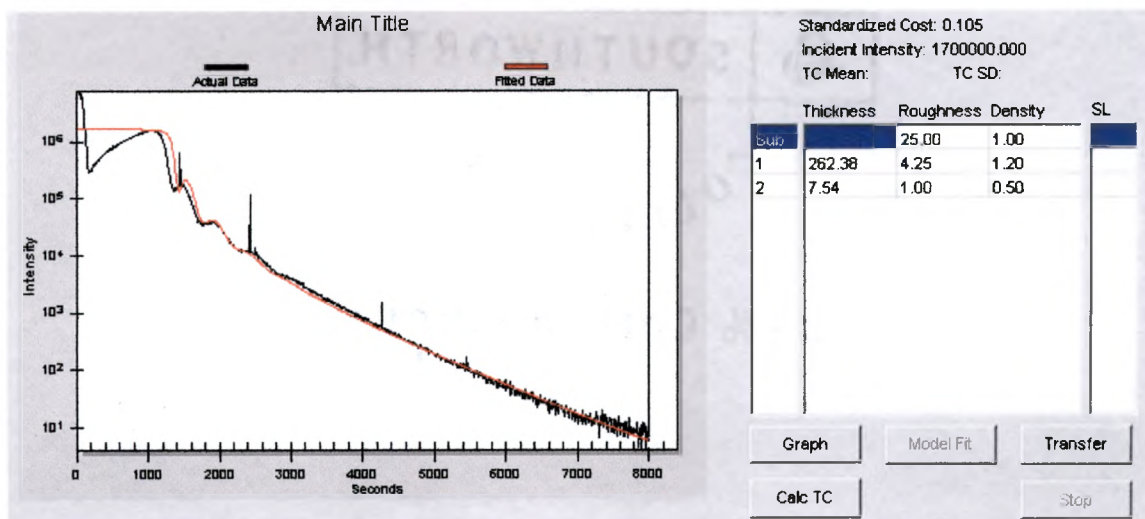


Figure 69: Low Density Top Layer as Suggested by Researchers at Bede Inc.

This fit is clearly inferior and still implies a high density ZnO layer very far from stoichiometric conditions. The resolution of this frustrating situation came about when Kevin Matney made available the newest version of REFS. The following graphs were analyzed using the same data set for the aforementioned sample. The single layer model fit generated by the newer version of REFS is shown in figure 69.

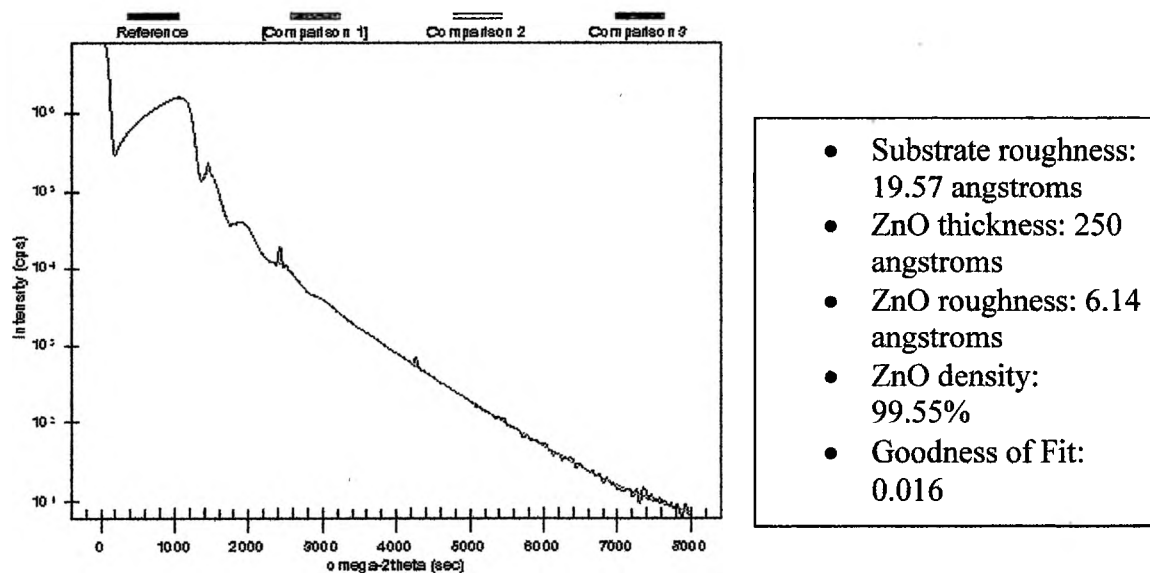


Figure 70: Single Layer Model Generated by REFS Version 4

This software package allows the user to model data starting from the critical angle (~1000 arcseconds), smooth the data set, and include instrumentation effects. Moreover, the REFS software is faster and much more versatile owing to an improved algorithm. One important note is the radical reduction in the Goodness of Fit parameter from 0.106 (v3.5b) to 0.016 (v4). I have also attempted a 2 layer model for this film using REFS version 4 shown in figure 71.

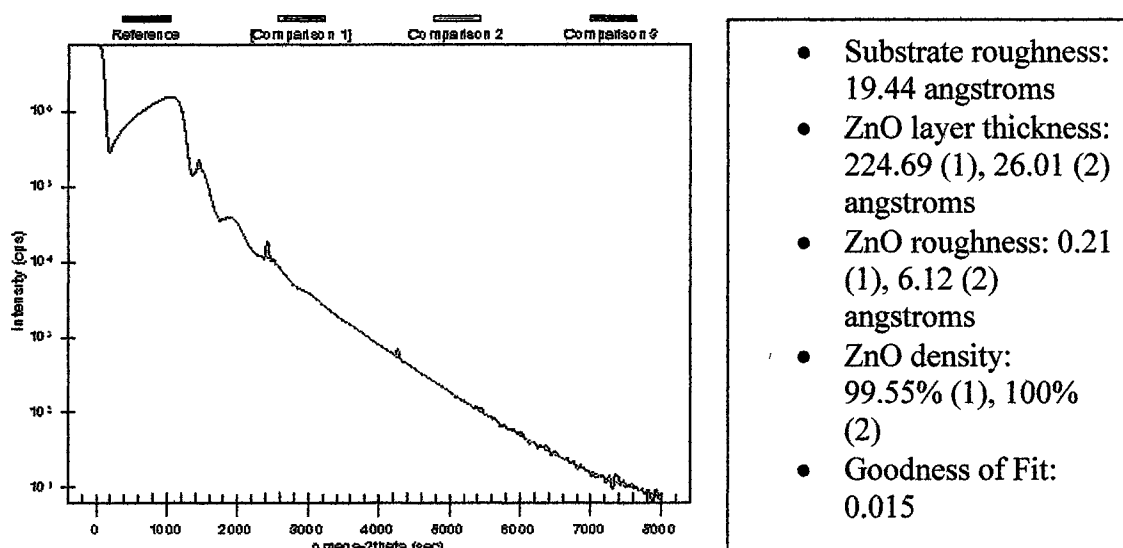


Figure 71: 2 Layer model generated by REFS Version 4

While the 2 layer model produced similar film characteristics and a slightly better fit, I am still more inclined to go with the single layer model. I have more faith in this simpler data fit because, as my thesis advisor reminded me, scientific conclusions requiring the fewest assumptions are the most valid in accordance with Occam's razor. The following combination of graphs and tables show a comparison of the XRR scans followed by a brief summary of the results returned by REFS version 4 modeling software. All XRR graphs have been shifted vertically for clarity.

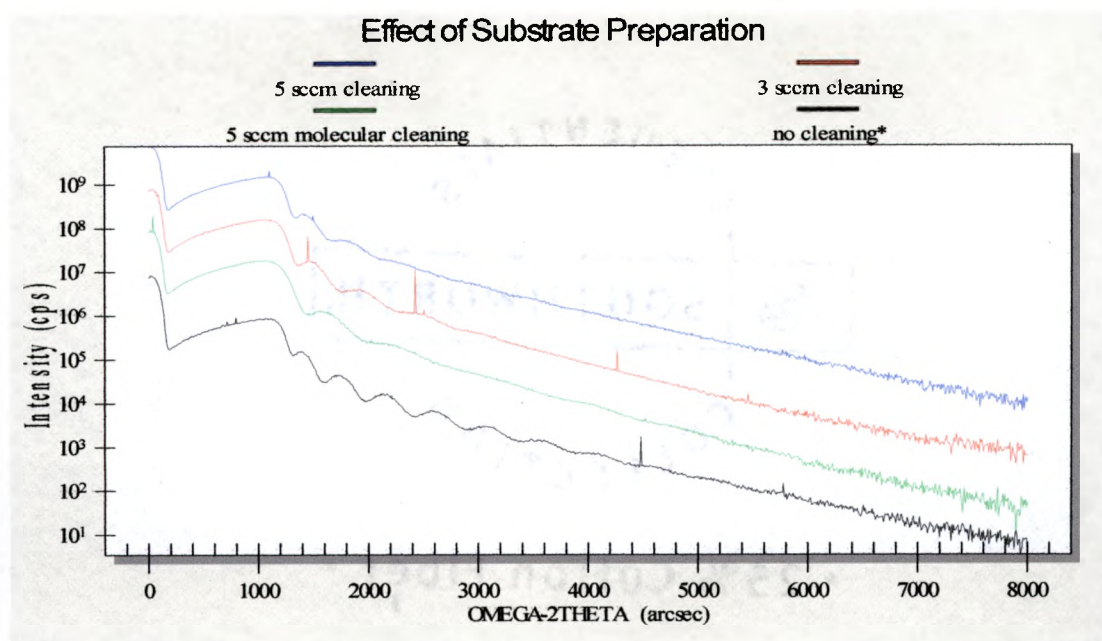


Figure 72: Effect of Substrate Preparation by Oxygen Radical Plasma

Sample (sccm plasma treatment)	Substrate roughness (Å)	ZnO Thickness (Å)	ZnO Roughness (Å)	ZnO Density (%)	Goodness of Fit (arbitrary units)
5	28.31	263.86	5.09	96.39	0.029
3	19.57	250.73	6.14	99.55	0.016
5-molecular	21.31	200.11	6.42	99.54	0.021
None	12.04	303.77	4.90	98.59	0.03

Table 26: REFS Model Properties for Different Substrate Preparation

The film with no plasma treatment actually shows the greatest deposition rate and smoothest interfaces. The low value for substrate roughness reported for the sample without plasma treatment prior to deposition reinforces the need to study the possibility of substrate damage due to oxygen treatment.

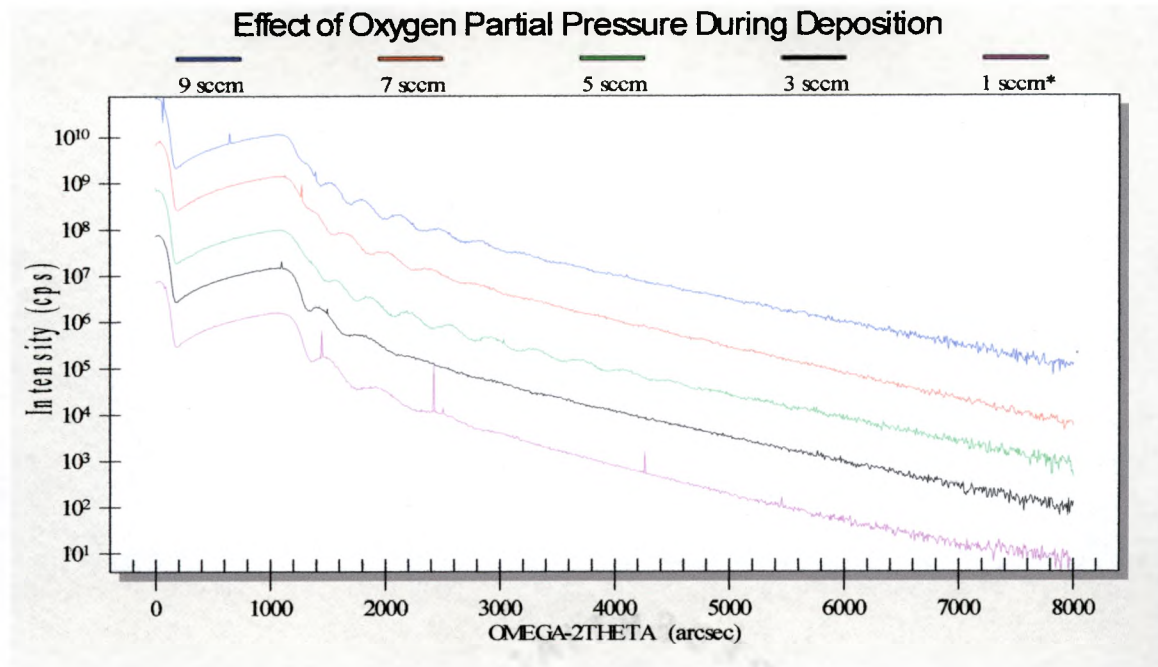


Figure 73: Effect of Oxygen Flow Rate During Deposition

Sample (sccm O during deposition)	Substrate roughness (Å)	ZnO Thickness (Å)	ZnO Roughness (Å)	ZnO Density (%)	Goodness of Fit (arbitrary units)
9	14.58	394.56	4.62	92.74	0.028
7	23.35	328.47	5.49	96.64	0.029
5	10.07	381.82	4.79	94.14	0.03
3	28.31	263.86	5.09	96.39	0.029
1	19.57	250.73	6.14	99.55	0.016
0	13.20	221.38	3.54	97.32	0.03

Table 27: REFS Model Properties for Different O Flow During Deposition

Firstly, note the variation in substrate surface roughness for films that were all treated with 5 sccm plasma prior to deposition (except 1 sccm film). This anomaly has yet to be resolved, but growth kinetics may be playing a critical role. The identity of species sputtered from the target material by the Kauffman source is something of a mystery.

The 800 eV Argon atoms have plenty of energy to break apart the ZnO bond so we suspect that the mean free path length in our evacuated chamber allows individual atoms of Zn and O to reach the substrate surface. The flux of additional O radical species from the atomic source may play an important role in the assembly of the initial 2D monolayers. These radical species gently sputter the substrate surface, aid decomposition of poorly aligned structures (along with thermal energy), and provide ready and willing chemical partners for the Zn adatoms. The clear optimized value for O flow rate to minimize roughness at all interfaces is 5 sccm during growth. The films deposited at higher O flow rates seem to achieve greater overall thickness. We expected to see a decrease in the deposition rate as the oxygen partial pressure increased, but the thickness reported for the film grown with 9 sccm O is actually the largest for this set of samples. Unfortunately, the mass flow controller that governs the delivery of Oxygen to the OAR ARS has a maximum value of 10 sccm so we were unable to further investigate this effect or find a turning point for which the deposition rate begins to decrease dramatically.

Substrate temperature effects were easily interpreted from HRXRD. We now examine how the roughness and interfaces depend on temperature using figure 74.

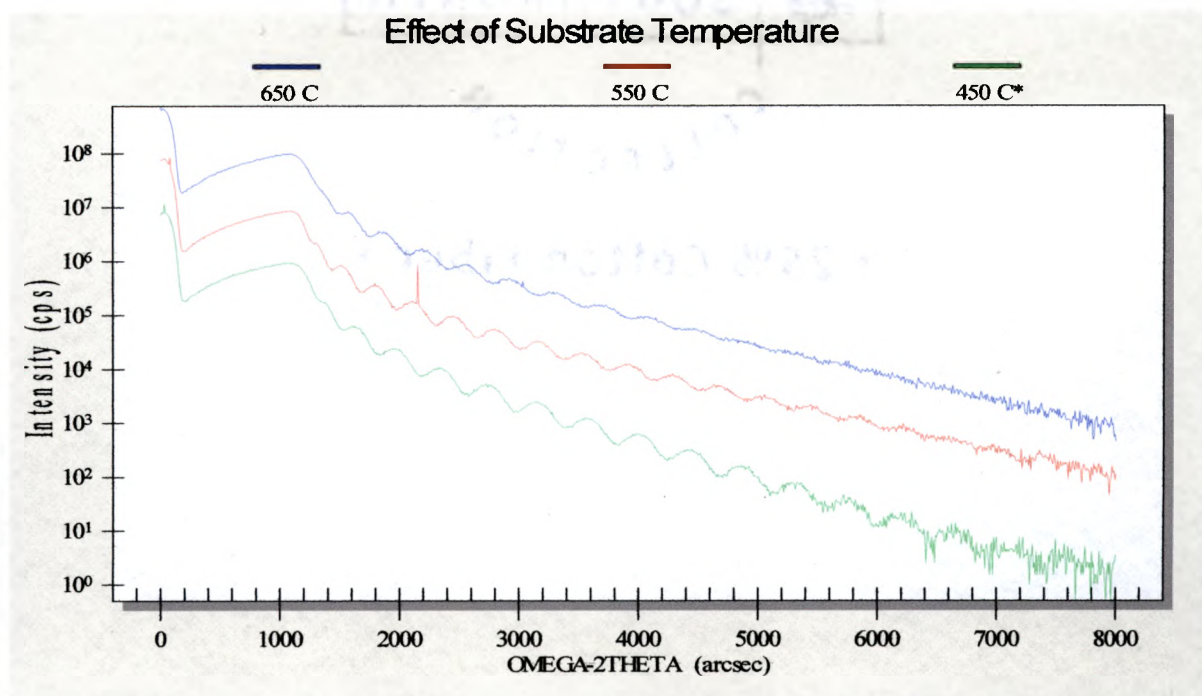


Figure 74: Effect of Deposition Temperature

Sample Deposition Temperature (Celsius)	Substrate roughness (A)	ZnO Thickness (A)	ZnO Roughness (A)	ZnO Density (%)	Goodness of Fit (arbitrary units)
650	10.07	381.82	4.79	94.14	0.03
550	6.86	401.67	4.33	92.42	0.04
450	7.21	351.50	6.82	100	0.033

Table 28: REFS Model Properties for Different Deposition Temperatures

The deposition rate appears to reach a maximum for a deposition temperature of 550 °C. Also, the roughness at the substrate interface decreases with temperature while the ZnO roughness increases. This lends support to reports from the literature claiming that a LT buffer helps alleviate lattice mismatch while higher deposition rates result in excellent

crystalline quality.

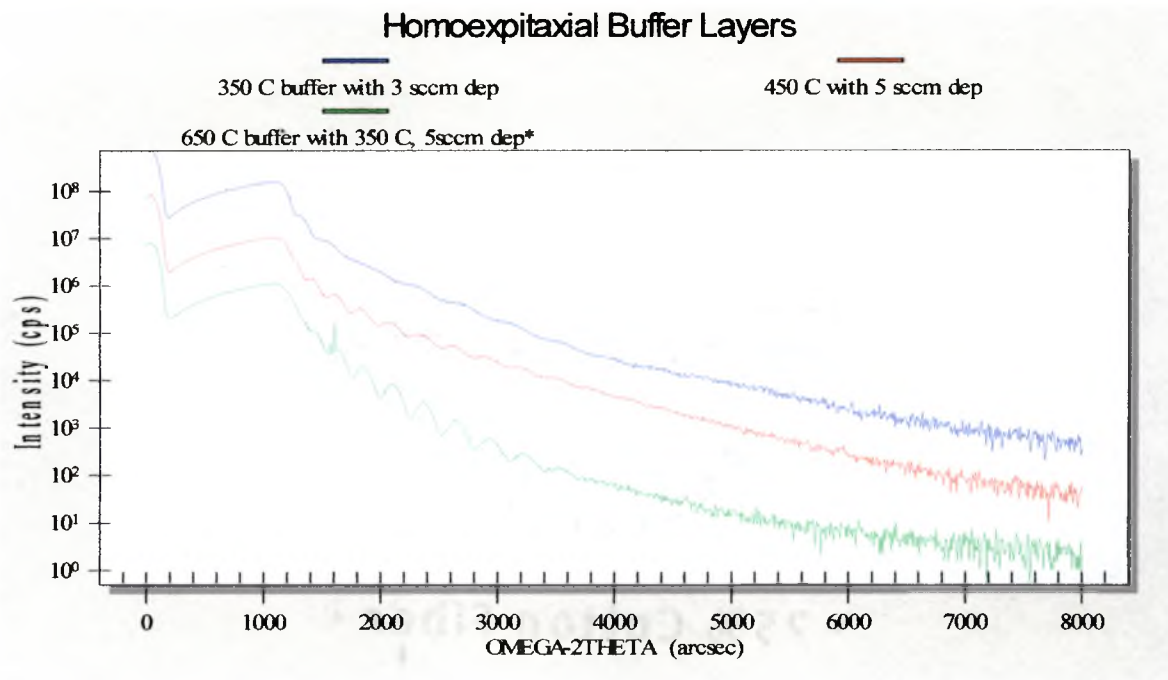


Figure 75: Effect of Homoepitaxial Buffer Layer

Sample	Substrate roughness (A)	ZnO Thickness (A)	ZnO Roughness (A)	ZnO Density (%)	Goodness of Fit
350 LT*	29.62	405 (total)	n/a	n/a	
450 LT	14.07	505.90	6.48	100	0.022
650 HT	4.63	501.17	16.87	100	0.053

Table 29: REFS Model Properties for Different Homoepitaxial Buffer Layers

As expected, the HT buffer shows a relatively smooth interface that transitions to a rough film that was deposited at 350 °C. The 450 °C LT buffer layer show the opposite trend with a rough interface next to the substrate transitioning to a smoother epitaxial film that was deposited at higher temperature. Even using the new modeling software, I could not fit the data for the 350 LT buffer layer using a simple one layer model. The best fit actually occurs for 2 layers but I doubt the validity of such a system unless there was

some undetected change in our fabrication process. The model predicts a low density top layer that could be indicative of overexposure to oxygen plasma after ZnO deposition ceased. The model shows a similar trend of a rough layer at the interface transitioning to a smooth epilayer of ZnO. The full modeling report may be found in the appendix.

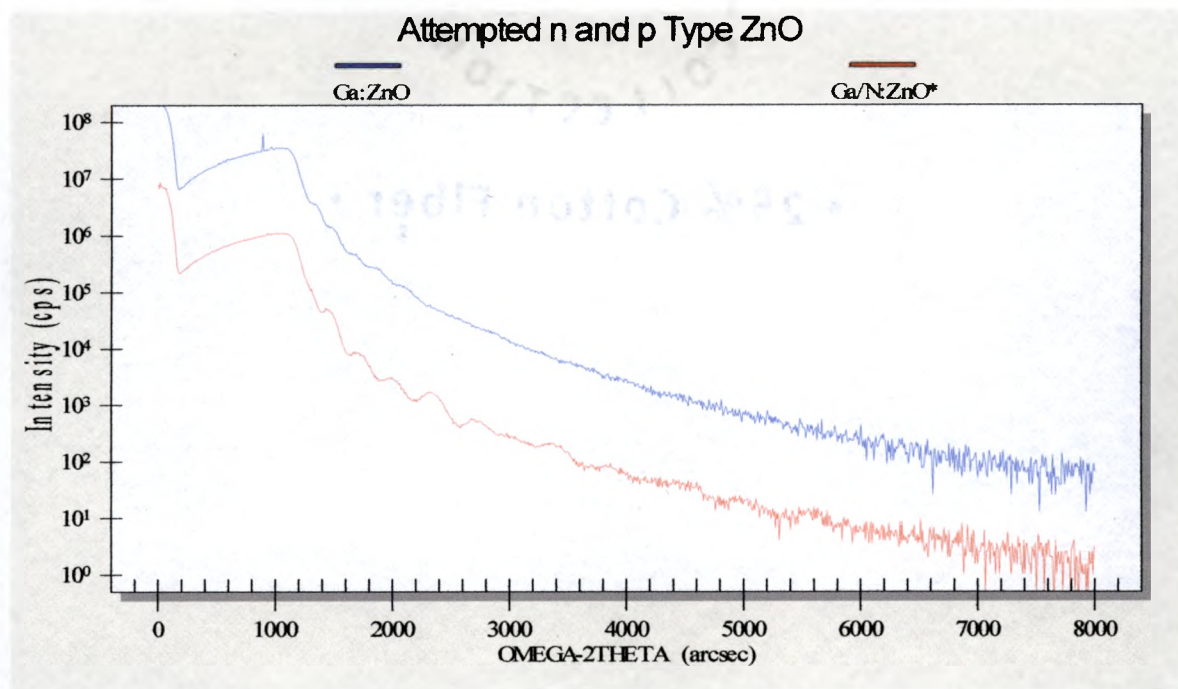


Figure 76: XRR of Ga:ZnO and Ga/N:ZnO

Modeling of these XRR scans was unsuccessful for a range of different models. Further investigation with XPS to determine the species present in the top 20 angstroms might enable me to create more exotic species to use as layer materials in the modeling software.

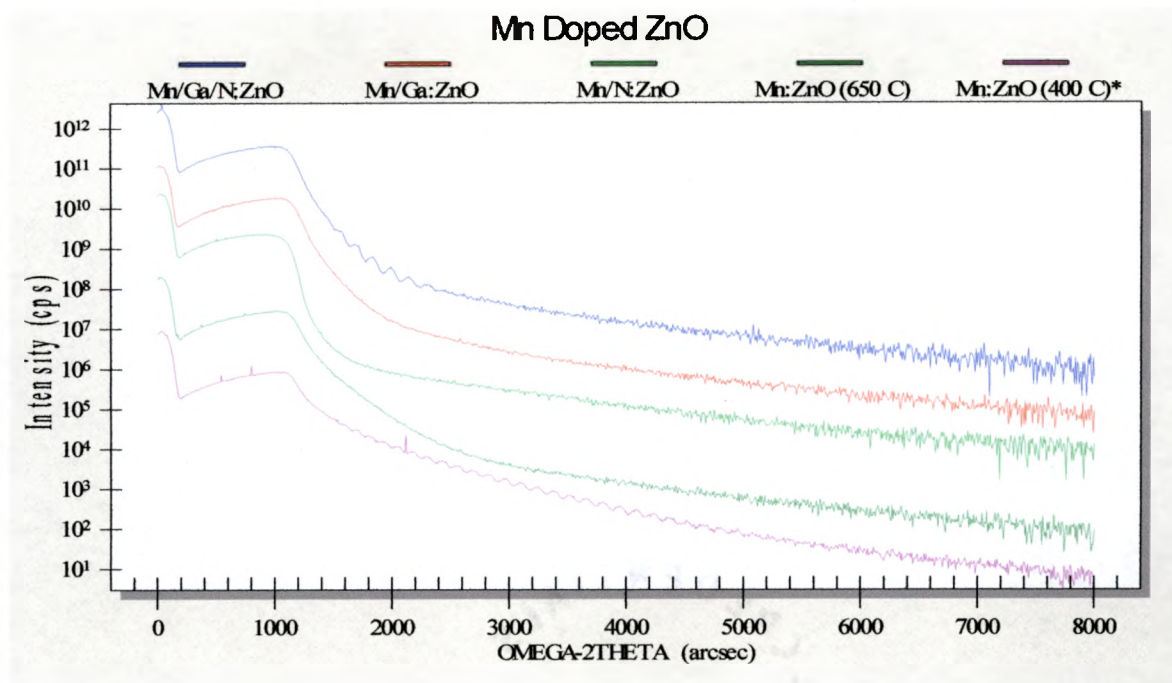


Figure 77: XRR of Mn Doped ZnO

Unfortunately, these films appear to be extremely rough with blurred interfaces. The only scans I was able to model are shown below in table 30.

Sample	Substrate roughness (Å)	ZnO Thickness (Å)	ZnO Roughness (Å)	ZnO Density (%)	Goodness of Fit (arbitrary units)
Mn/Ga/N:ZnO	0.1	837	31.53	96.23	0.069
Mn:ZnO (400 C)	10.51	1077	6.62	98.86	0.049

Table 30: REFS Model Properties for Mn Doped ZnO

These fits are circumspect in terms of the interface properties, but the thickness matches the qualitative interpretation (high frequency fringes) of the XRR scans. This tells us that the deposition process for a target containing MnO shows a much higher deposition rate.

V. ATOMIC FORCE MICROSCOPY ANALYSIS

5.1 Theory

Atomic Force Microscopy utilizes attractive and repulsive forces between a sample and an atomically sharp tip usually made of silicon to measure surface profiles. The tip is attached to a cantilever arm that oscillates when voltage is applied to a piezo transducer. The harmonic motion is damped by various forces depending on the proximity to the surface of the sample as shown in figure 78.

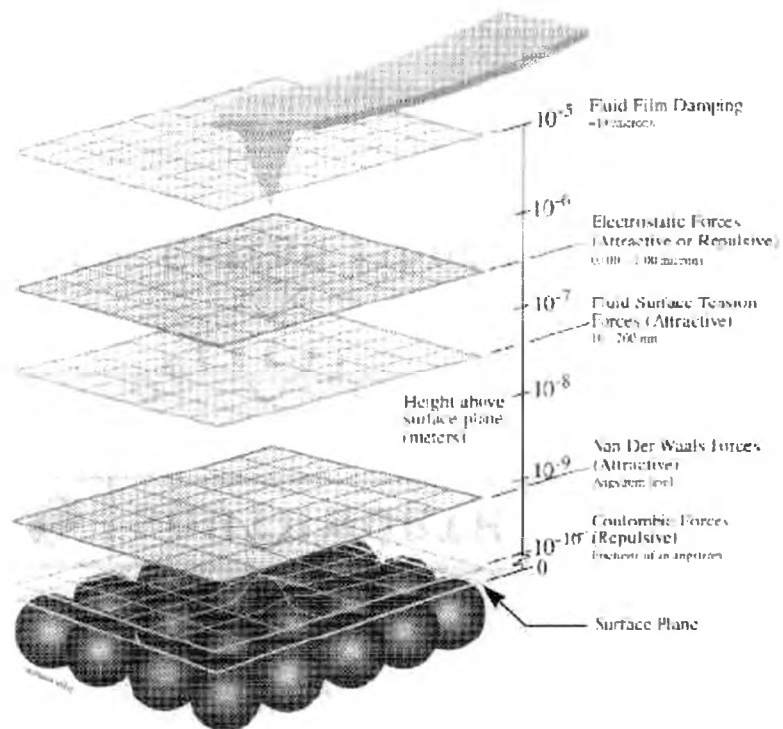


Figure 78: Damping Forces for Different Distances Between Sample and Tip⁹²

The deflection of the cantilever arm is measurable with resolution on the order of picometers by angular deflection of a reflected laser beam. The laser beam strikes position sensitive photodiodes usually arranged side by side or in quadrants. The calibrated relationship between the voltage applied to the transducer and detected laser signal for a known sample is utilized to determine the deflection of the cantilever arm and thus the surface morphology of an unknown. A typical AFM apparatus is shown in figures 79 and 80.

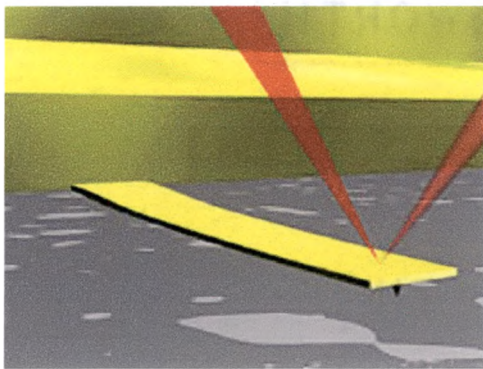


Figure 79: Sample AFM Cantilever⁹³

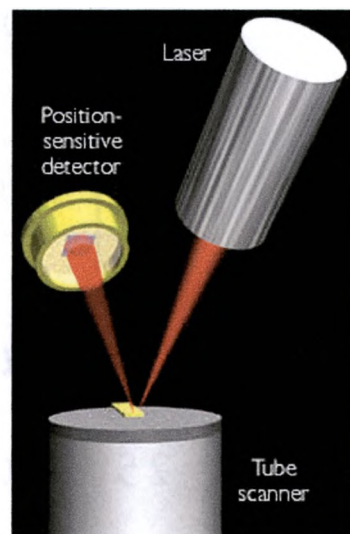


Figure 80: Photodiode Configuration⁹³

5.2 Apparatus

The AFM measurements performed by Eric Botello from Dr. Heather Galloway's research group here at TSU were taken on a Park Scientific Instruments Autoprobe CP system. The cantilever and tip are fabricated from polysilicon and coated with gold to facilitate laser reflection from the surface of the cantilever to the photodiode. The general shape of the cantilever arm is best described as a flying V with a Si tip positioned at the vertex perpendicular to the plane of the V. The scans were performed by rastering the tip (contact mode) across the plane of the sample from left to right and then from right to left in the x-direction. This line scan was repeated for successive steps in the y-direction resulting in a profile of the surface. Scans were conducted on each sample for areas of $100 \mu\text{m}^2$ (10X10), $9 \mu\text{m}^2$ (3X3), and $1 \mu\text{m}^2$ (1X1). These images were analyzed using a software package that levels the scan to account for sample tilt and averages surface features to create a histogram of surface roughness. This data is returned to the user in the form of rms roughness, average roughness, and peak to valley separation.

5.3 AFM Data

Initial investigations of the surface profile for a few films were rather disappointing. I was hoping to see some sort of hexagonal grains near the surface suggested by other researchers, but all surfaces appeared smooth and featureless. In any case, it became clear rather quickly that the size of the scan affects the roughness values. The general trend of decreasing surface roughness for a 10X10, 3X3 and 1X1 scan of one of our best samples is detailed in table 31.

Scan Size (microns)	Rms (angstroms)	Ave roughness (angstroms)
10X10	17.1, 13.6	4, 3.21
3X3	3.19, 3.12	2.49, 2.42
1X1	2.27	1.75

Table 31: AFM Data for Optimized Undoped ZnO Sample

The 3D graphical representations of these scans are shown in figures 81-83.

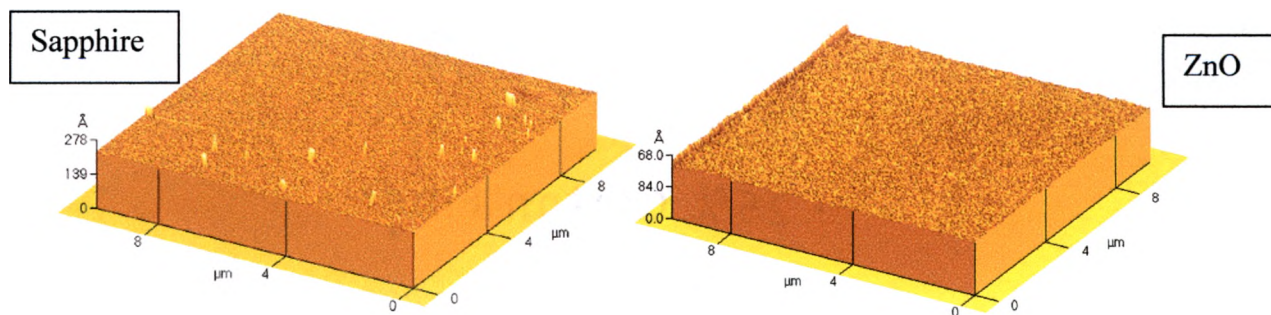


Figure 81: As Received Sapphire Substrate and Optimized Sample (10X10).

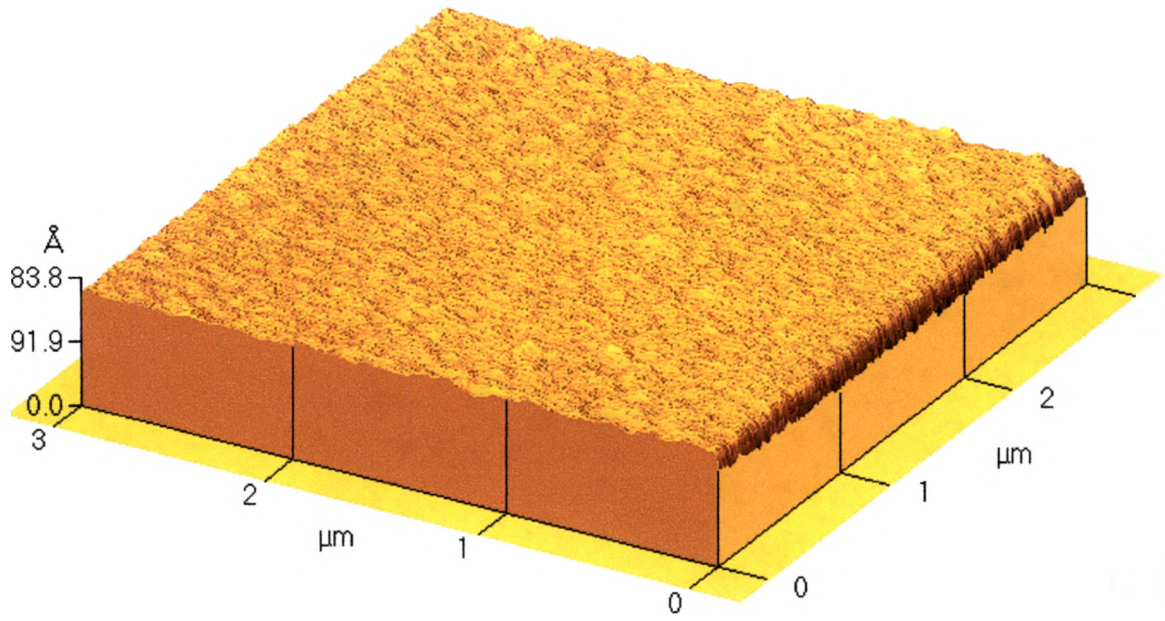


Figure 82: Optimized Sample (3X3).

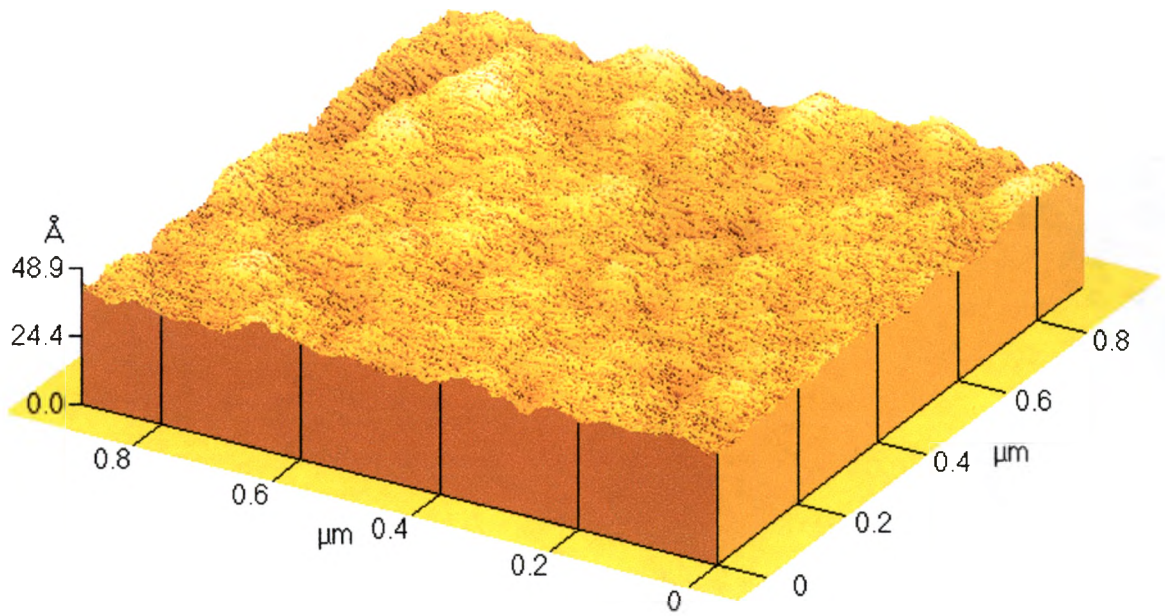


Figure 83: Optimized Sample (1X1)

If the growth and nucleation theories are correct, we may be seeing evidence of 3D island nucleation at the surface of this sample. Further analysis of films deposited at different temperatures will be conducted to evaluate growth kinetics as a function of temperature.

VI. ELECTRICAL PROPERTIES ANALYSIS

6.1 Hot Probe Experiment (Thermal EMF)

This rather simple but elegant technique, depicted in figure 84, uses a heated probe connected to the positive terminal of a sensitive ammeter and a cold (room temperature) probe attached to the negative terminal placed across a semiconductor to determine its carrier type. For example, if the material is n-type, excess electrons transition to the conduction band in the vicinity of the hot probe. The resulting potential difference sets up an electric field which forces the electrons to flow toward the cold probe.

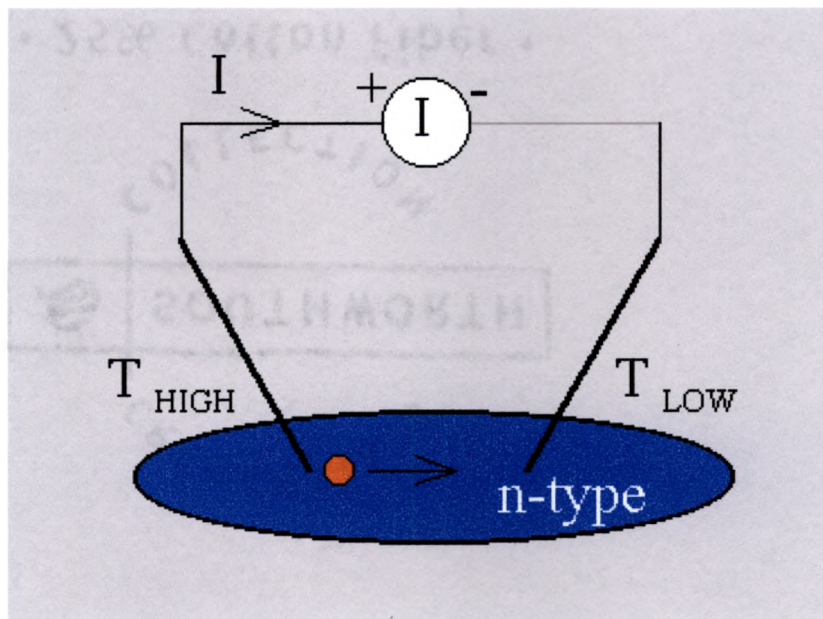


Figure 84: Hot Probe Experimental Setup⁹⁴

The carriers move from the hot probe to the cold probe resulting in a positive reading for n-type material (electron current) and a negative reading for p-type material (hole current). The substantial electric field in the semiconductor results in drift current dominating any diffusion current in the material. If one assumes that the Fermi level of the semiconductor remains constant throughout the material and that the semiconductor does not become degenerate or intrinsic in the applied temperature range, then the current can also be explained by a shift in the conduction and valence band energies. The application of thermal energy causes a local increase in the density of states and an increase in the conduction and valence band energies as depicted in figure 85.

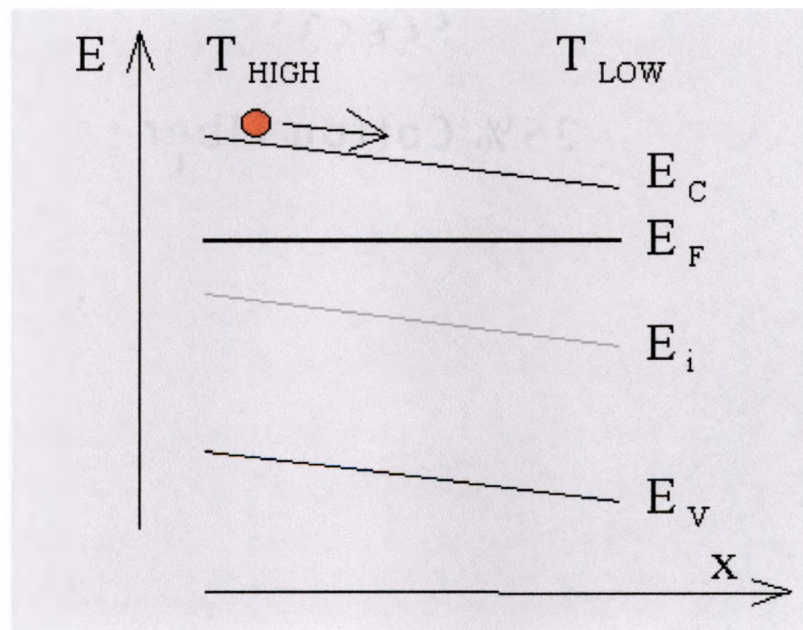


Figure 85: Band Shifting Due to the Application of a Thermal Gradient⁹⁴

This gradient results in an electric field that causes both holes and electron to move toward the cold probe. Our setup, shown in the appendix, consists of an HP 4140A picoammeter with a baseline of $\sim 1 \cdot 10^{-9}$ A and two soldering irons serving as the hot and

cold probes. One frustrating problem with this setup is a leakage current from the local AC circuit through the soldering iron heater. This feedback results in a current of 1×10^{-4} A eliminated only after the iron is detached from the heater. Immediately after detaching the iron from the heater base, we examined two polished silicon wafers that were p and n doped with Boron and Antimony respectively. The hot probe was placed in contact with the wafer 1 cm from the cold probe. The average currents were -0.3×10^{-6} A and 0.5×10^{-5} A for the p-type and n-type wafers respectively. The currents degraded after a few minutes as the thermal energy from the hot probe dissipated. Consequently, the hot probe was reheated to its maximum temperature (~ 700 K) between each sample. Hot probe analysis was performed on all samples using the same setup. The results are shown in table32.

Sample	Current (nA)	Doping type (p, n, i)
p-type wafer	-300	P
n-type wafer	5000	N
Sapphire	2	I
40430	600	N
40503	90	N
40506	100	N
40510	600	N
40514	30	N
40517	30	N
40518	10	I
40519	-0.5	I
40520	2.6	I
40607	10	I
40608	120	N
40609	30	N
40611c	-0.3	I
40611a	24	I
40611b	3	I
40615	50	N
40708	100	N

Please refer to the experimental matrices found in chapter 3 for specific characteristics of the samples. The cutoff level for determining carrier type was arbitrarily chosen as 30 nA.

(i = indeterminate carrier type)

Sample	Current (nA)	Doping Type (p, n, i)
40614	15	I
40617	-0.3	I
40618	1	I
40622	-1	I
40623	-1	I
40624	100	N
40629	25	I
40701	2.2	I
40709	60	N
40712	7.5	I

Table 32: Thermal EMF Results for ZnO Films

6.2 I-V Characteristics

Investigation of the I-V characteristics of several ZnO films showing a response for the Thermal EMF experiment was carried out using an HP 4145A Semiconductor Parameter Analyzer. The contact probe apparatus is shown in the appendix. Current was measured at room temperature and 373K as a function of applied potential difference ranging from 0-30 V. It is important to note that the positioning of the probes was not precise. When the samples were heated, the probes were lifted from the surface and translated back to the same position after temperature ramping. Invariably, the distance between the probes and the pressure applied to the sample were affected by this procedure. In order to mitigate this problem, I positioned the probes at the edge of visibility for the 10X microscope objective (~ 3mm spot size) and increased the applied pressure until the tips began to slide over the film surface. Several current measurements were taken at each temperature to ensure repeatability. A bare sapphire substrate showed no conductivity at room temperature which is appropriate for an insulator with a large band gap. The I-V curves for an undoped sample (ZnO 040515 – 5 sccm radical Oxygen cleaning, no Oxygen during 650 °C deposition) are shown in figure 86.

I-V Curves for Undoped ZnO at Different Temperatures

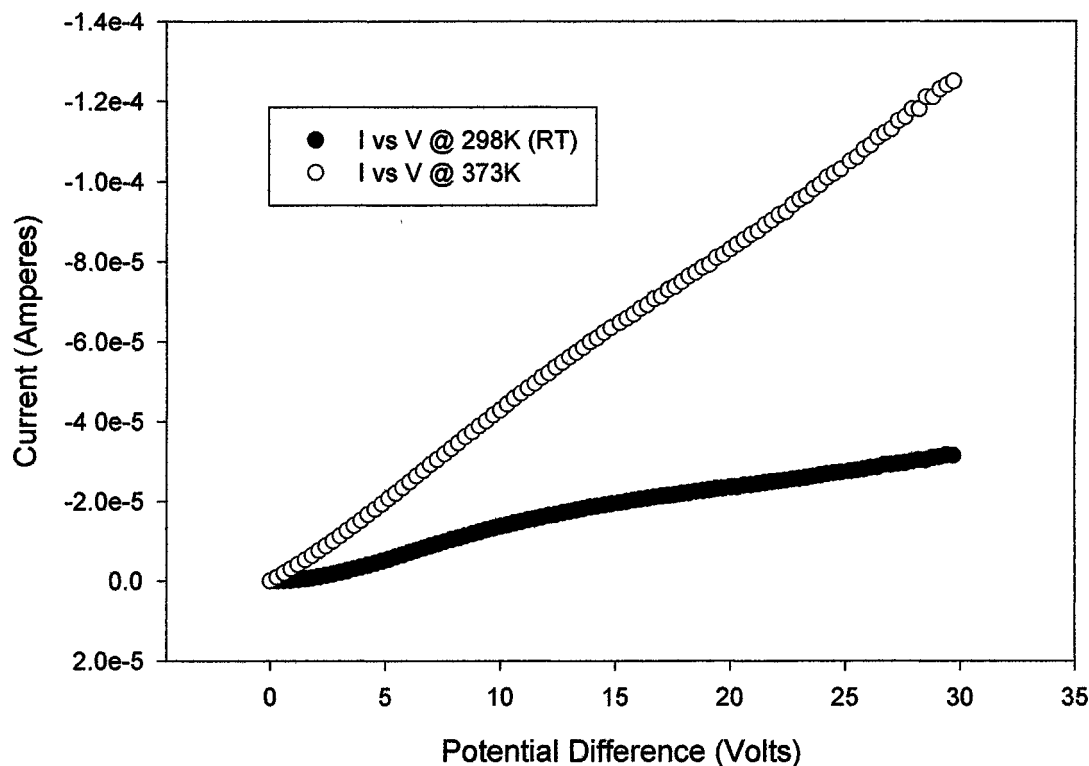


Figure 86: I vs. V for an undoped ZnO film at room temperature and 373K

Upon increasing the temperature by 75K, the current increased from 20 to 120 microamperes. As discussed in the introduction, this is a good indication of semiconductor behavior because additional thermal energy results in an increased carrier concentration in the conduction band. Yet another sample with a large response to Thermal EMF testing is shown in figure 87.

I-V for Undoped ZnO with Buffer Layer at Different Temperatures

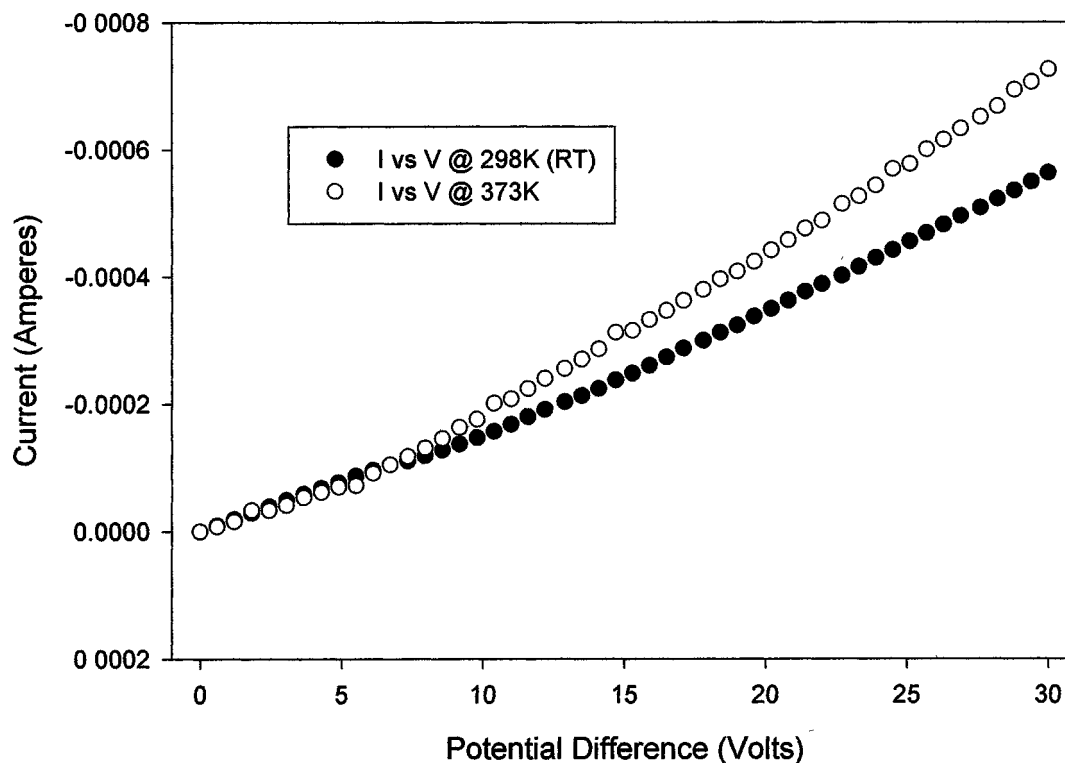


Figure 87: I-V curves for ZnO 040510 (LT buffer layer).

Here, we see a change from 0.5 to 0.7 milliamperes. This sample is much more conductive than the sample without plasma treatment though both films were undoped. This may indicate a higher density of native defects that act as donors. The final set of data, shown in figure 88, highlights the response for our best attempts at n and p type ZnO.

I-V Curves for Attempted n and p Type ZnO

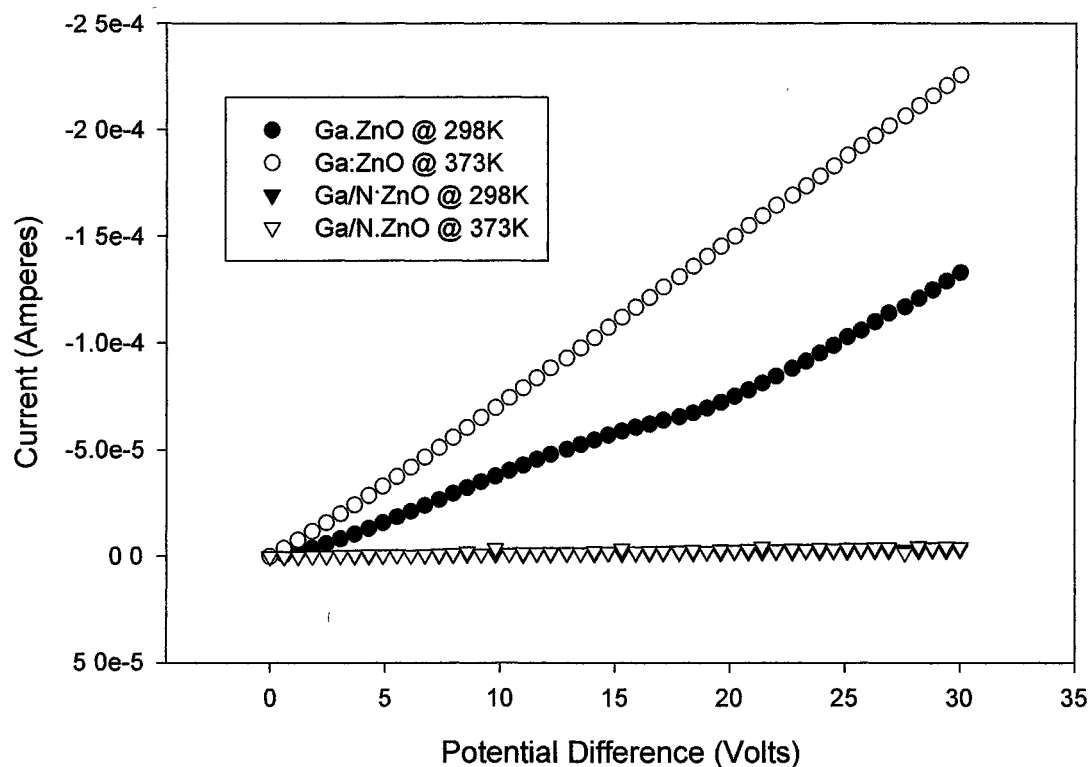


Figure 88: I-V curves for Attempted n and p Type ZnO

The n-type film (Ga:ZnO) shows current on the order of miliamperes with an increase of ~ 10 mA for a temperature change of 75 degrees. I'm sad to report that the p-type attempt (Ga/N:ZnO) failed to show any conductivity.

Another interesting phenomenon that we observed was the excitation of carriers upon irradiation with a Hg lamp. As shown in figure 89, the current increased when the sample was exposed to the UV light.

Optical Excitation of Carriers in Undoped ZnO at 373K

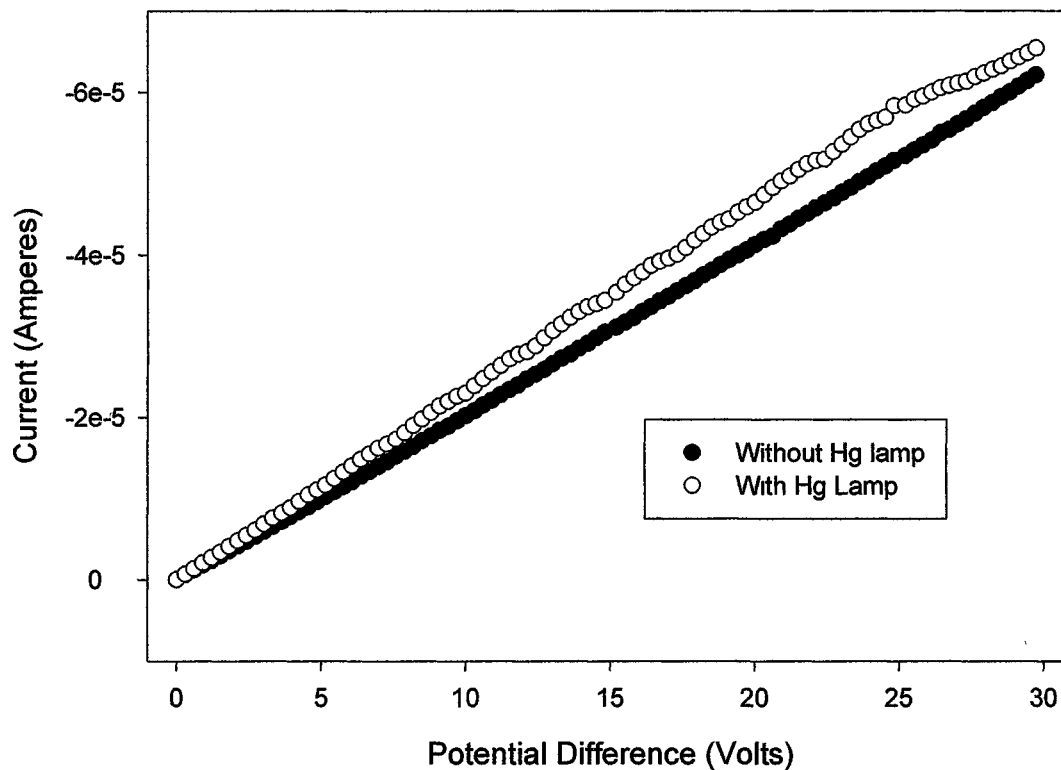


Figure 89: I vs. V Under U-V Irradiation from a Hg Lamp

The band gap for bulk ZnO lies in the UV range of the electromagnetic spectrum. When a photon of the appropriate energy strikes the samples, electrons absorb this energy to jump the gap. Increased carrier concentration in the conduction band leads to lower resistivity and higher current. The difference in the current could be increased if we were able to tune the radiation from the Hg lamp to match the optical band gap of the film.

6.3 Hall Effect Measurement

Edwin H. Hall first observed⁹⁵ a small transverse voltage across a current-carrying thin metal strip immersed in a magnetic field in 1879. This phenomenon provides a way to ascertain the carrier density and mobility in a material. The fundamental physics behind the Hall voltage measurement is the Lorentz Force. A charge moving in a magnetic field feels a force proportional to the vector product of v and B . For the experimental setup shown in figure 90, this results in a charge buildup along one side of the semiconductor (force is along the y direction).

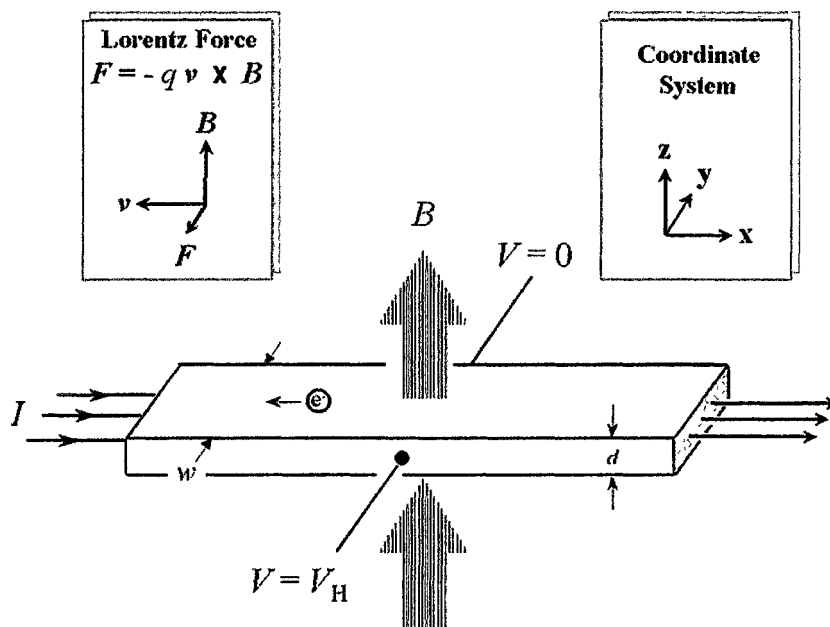


Figure 90: Hall Effect⁹⁵

This transverse voltage V_H is equal to the product of the current in the x direction times the applied magnetic field divided by the sheet carrier density. In order to determine the sheet resistance and carrier density, one employs the widely used van der Pauw technique. The sheet resistance is determined by measuring the resistance between a set of four terminals on the sample as shown in figure 91.

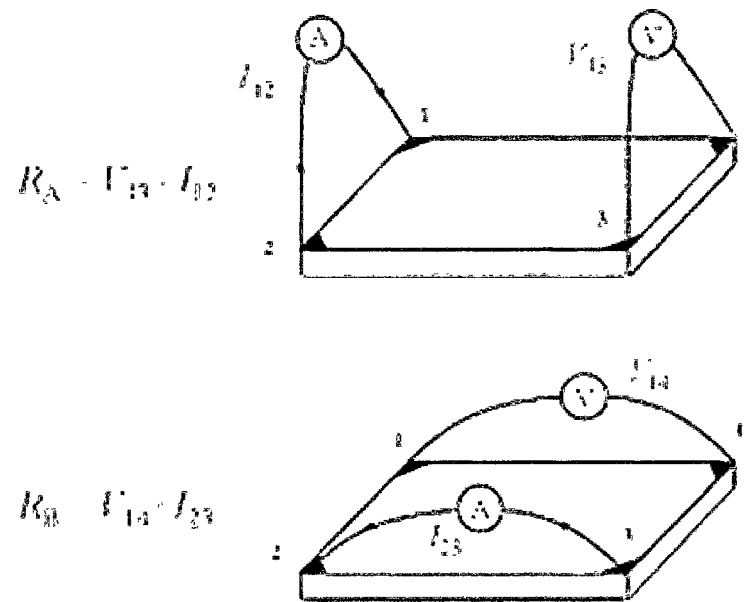


Figure 91: Van der Pauw Configuration for Determining Sheet Resistance⁹⁵

The characteristic resistances R_A and R_B are used to numerically determine the sheet resistance R_S using the following formula⁹⁵:

$$\exp(-\pi R_A / R_S) + \exp(-\pi R_B / R_S) = 1$$

The Hall voltage and carrier density can be determined by measuring a series of voltages for a constant current through opposing points in a constant applied magnetic field as depicted in figure 92.

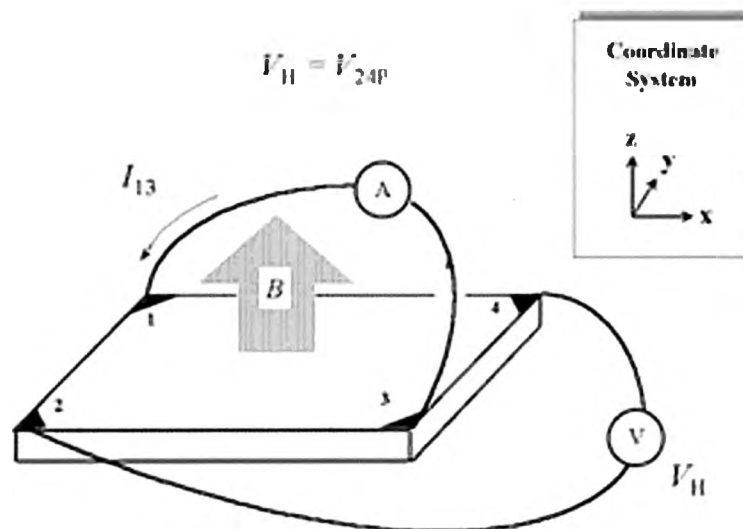


Figure 92: Setup for Determining Hall Voltage and Carrier Mobility⁹⁵

During these measurements, one must ensure that contacts exhibit ohmic behavior, uniform temperature is maintained, and photovoltaic effects are suppressed. Intentionally doped samples will require the application of ohmic contacts at the corners for Hall effect analysis. We plan to develop a patterning process that makes use of a mask over the center of the sample to deposit ohmic contacts with the DIBS and evaporator instruments. For our preliminary work, we plan to use Indium solder on the 4 corners of our samples. Hall measurements will be performed from 10-298K for varying field strengths.

VII. VIBRATING SAMPLE MAGNETOMETER ANALYSIS

7.1 Theory

Vibrating Sample Magnetometers are used extensively to characterize a wide range of magnetic materials. A standard setup is shown in figure 93.

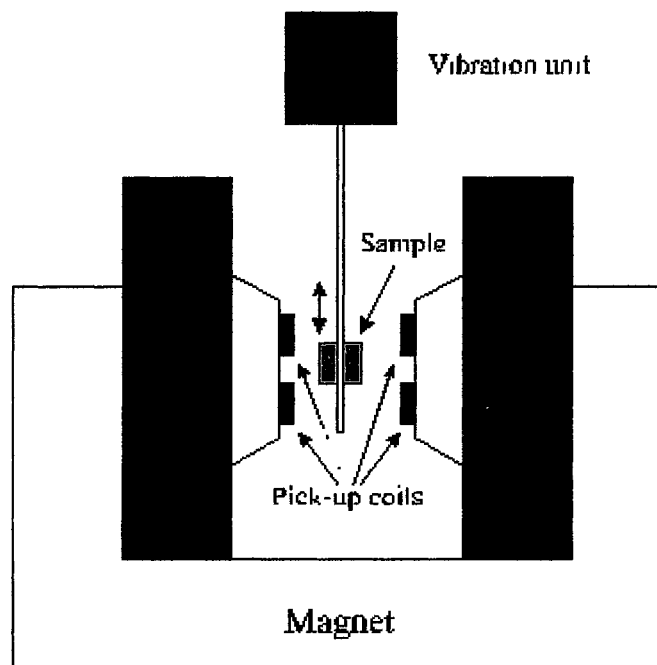


Figure 93: Standard Components of a VSM⁹⁶

The sample is attached to an oscillating mechanism and positioned between two large electromagnets in a DC field. When the magnetic field through the detection coils changes due to the vibration of the sample, they generate a voltage in accordance with

Lenz's law. This voltage signal is converted to display a graph of the magnetization M as a function of the applied field B . A sample of this type of graph called a hysteresis loop (from the Greek: to lag or delay), depicted in figure 94, contains information about the remanent magnetization, saturation magnetization, coercive field, and magnetic hardness/softness of the material.

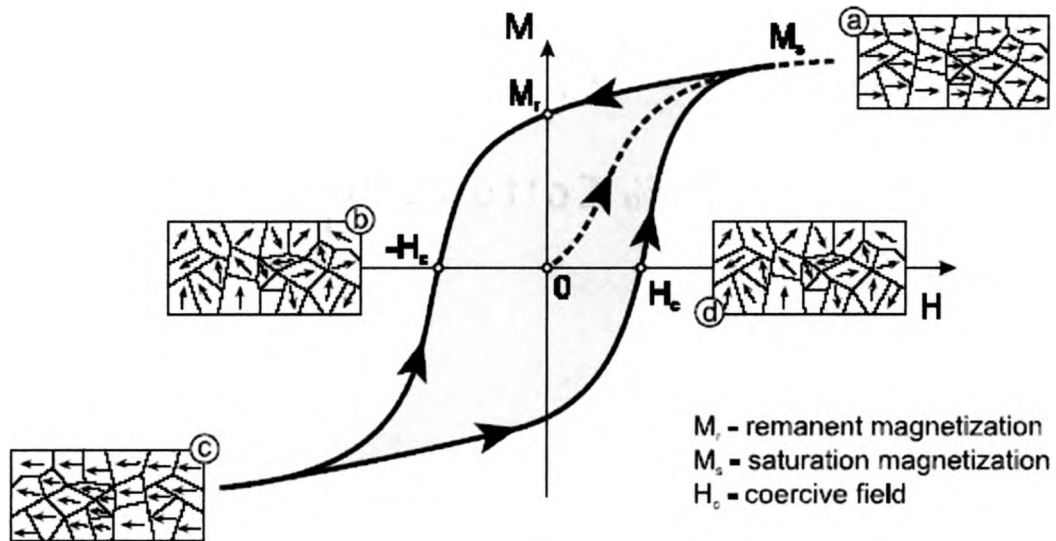


Figure 94: Points of Interest for a Standard Hysteresis Loop⁹⁷

7.2 Apparatus

The VSM instrument at TSU, pictured in the appendix, is an LDJ model with a minimum sensitivity of 0.01 emu and maximum field strength of 10,000 Oe. The system was calibrated using a nickel standard before each scan. Locating the optimized position between the coils was problematic due to the very thin films were investigating. To mitigate this problem, we used a small piece of nickel foil with the same dimensions as the sapphire substrate to find the optimized position. We then replaced the Ni foil with our sample and started taking data.

7.3 VSM Data

The initial scans of Mn/Ga/N:ZnO were carried out in Quick mode for in-plane and out of plane sample alignment. The scans are shown in figures 95 and 96.

Quick In-Plane Scan of Mn/Ga:ZnO

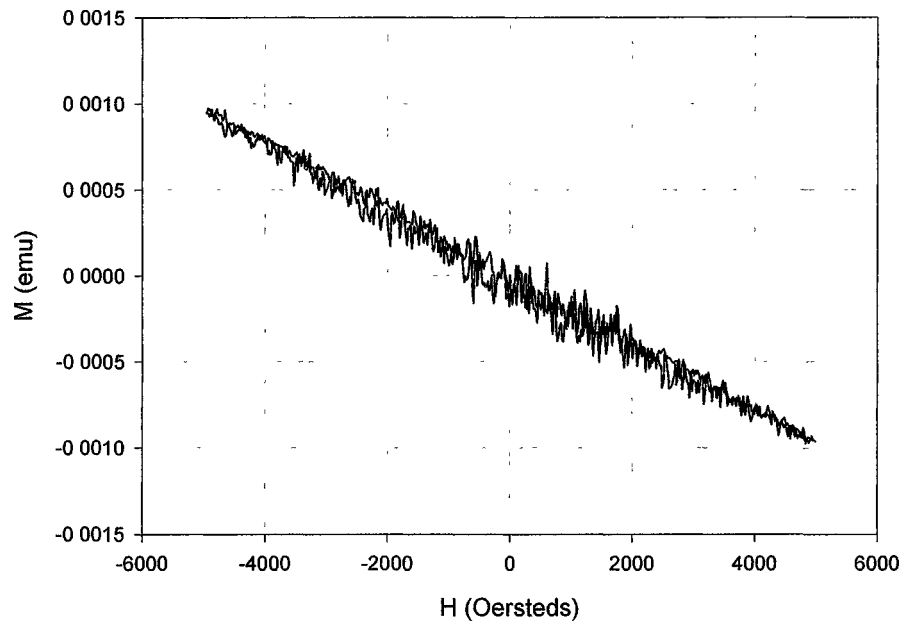


Figure 95: In plane Quick VSM Scan of Mn/Ga:ZnO

Quick Out of Plane Scan for Mn/Ga:ZnO

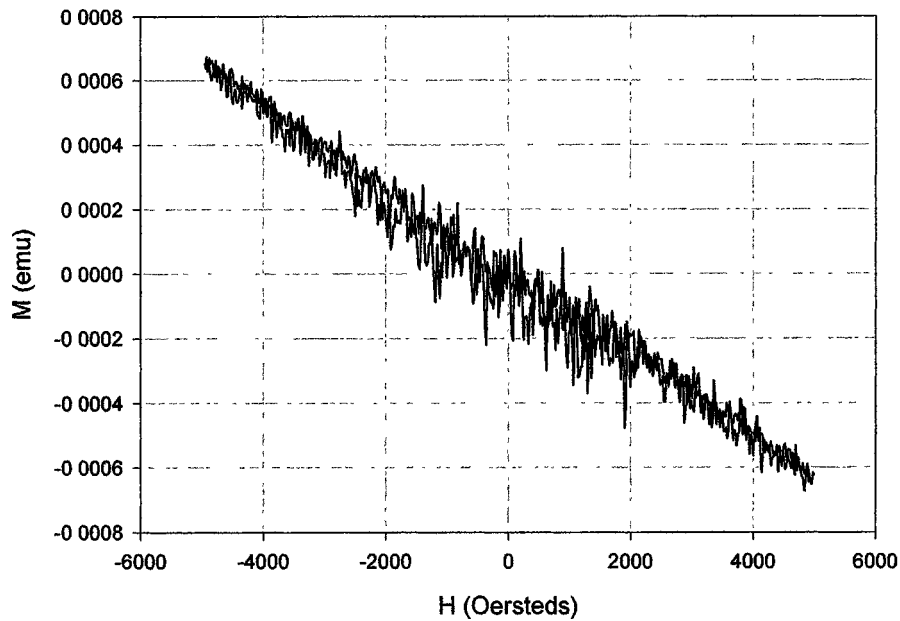


Figure 96: Out of Plane Quick VSM Scan of Mn/Ga:ZnO

We see only the dielectric response from the sapphire substrate. Because these quick scans have low sensitivity, we also attempted scans in accurate mode with higher count time, lower emu sensitivity, and lower Peak Field Strength. These scans, which typically ran for more than 8 hours, are shown in figures 97-99.

Accurate Scan of Mn/Ga/N:ZnO

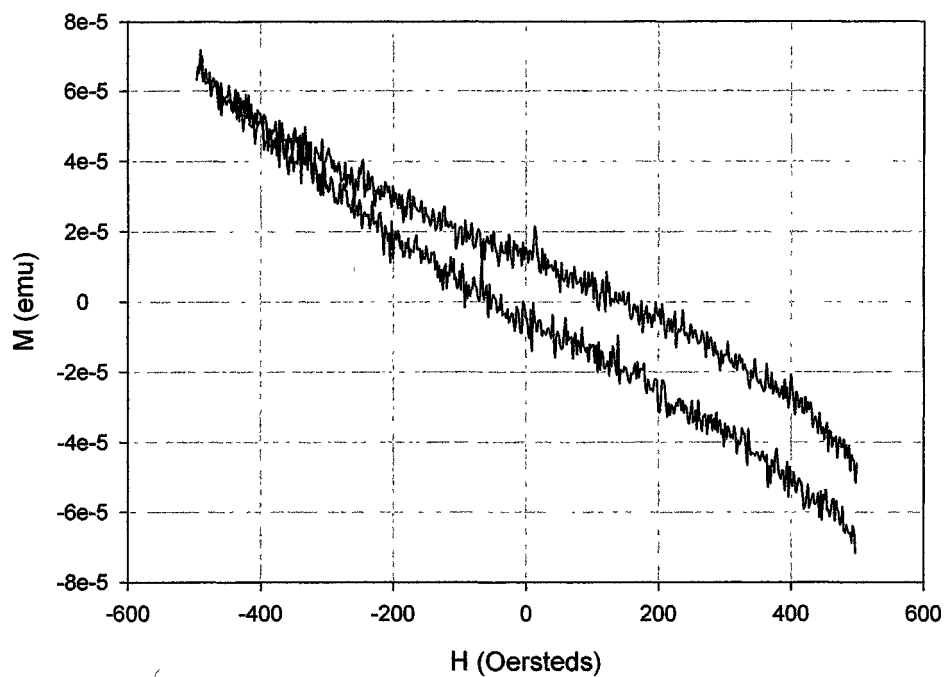


Figure 97: Accurate Scan of Mn/Ga/N:ZnO

Accurate Scan of Mn/Ga:ZnO

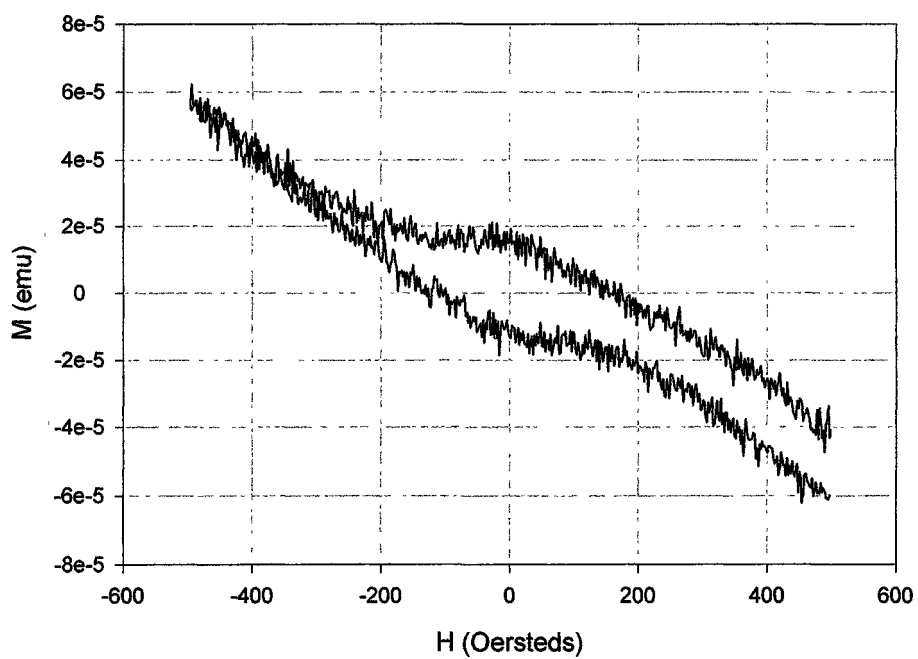


Figure 98: Accurate Scan of Mn/Ga:ZnO

Accurate Scan for Mn:ZnO

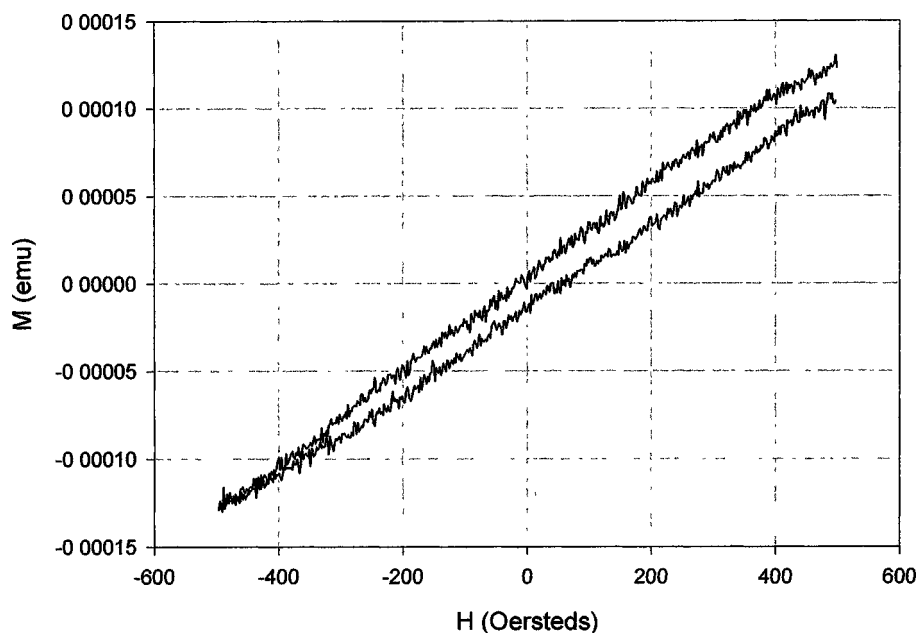


Figure 99: Accurate Scan of Mn:ZnO (400 °C)

Though some films look promising, we are dealing with an extremely small magnetic moment from the Mn ions. The tendency of the loop not to close at one end is evidence that we are very accurately measuring the drift for the instrument. Due to the small size of the moment for Mn ($\sim 0.16 \mu_B$) and the extremely thin layers, we have observed only the dielectric response from the substrate. We plan to investigate possible magnetic response below room temperature using a SQUID device at UT for thicker films.

VIII. CONCLUSIONS

We have successfully fabricated epitaxial ZnO films on sapphire substrates while examining the effect of Oxygen plasma treatment, Oxygen flow during deposition, and deposition temperature. Though widely reported in the literature as a prerequisite for epitaxial ZnO growth on sapphire, we found that Oxygen radical treatment from our OAR ARS may actually damage the sapphire surface. Yet films with pre-deposition treatment exhibit less strain than untreated films. Increased radical Oxygen flow during deposition resulted in both increased crystallinity and strain. Reflectivity scans also reveal an increased deposition rate, improved substrate interface, and Zn deficiency for increasing O flow. Deposition temperature radically affected both crystallinity and strain with higher temperatures producing the most favorable conditions for epitaxial growth. Homoepitaxial buffer layers were successfully employed to reduce strain for our ZnO films but MgO heteroepitaxial buffers, though touted in the literature, did not prove a useful technique for this work. Further investigation concerning the use of homoepitaxial buffer layers may help our research group realize Mn doped ZnO with room temperature ferromagnetic properties and p-type Gallium/Nitrogen co doped ZnO. This study raises important questions regarding the growth kinetics for doped ZnO. Growth of thicker films and integrating an advanced network of additional characterization tools with university collaborators are the near term goals for extending this work. I hope to co-

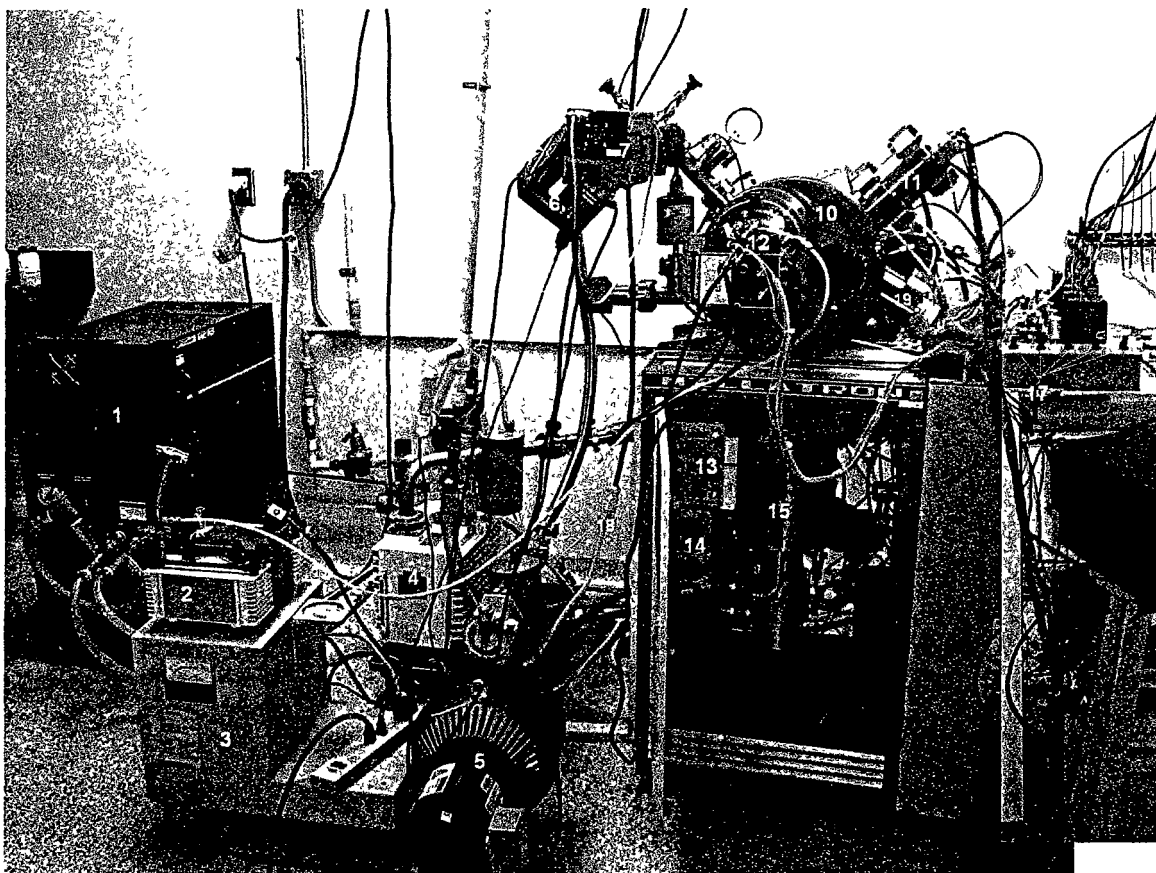
author a paper based on the findings of this research and use it as a stepping stone for related PhD dissertation studies.

In conclusion, ZnO is an attractive material with a wide range of possible applications. Successful engineering of the optical, mechanical, and electrical characteristics will prove to be a demanding but rewarding venture. It is my sincere hope that this work contributes in some way to the large scale manufacture of solar cells with transparent ZnO windows. This is quite possibly the most easily implemented and desperately needed application for an environmentally benign material like ZnO because the energy needs of the 21st century cannot wait until we run out of fossil fuels. Hopefully, the scientists and engineers will make use of novel materials like ZnO to responsibly transform and improve the quality of life for all.

APPENDICES

Appendix A: Radical Assist Ion Beam Sputtering System.....	147
Appendix B: Bede D1 Diffractometer.....	151
Appendix C: How to Find an Asymmetric Peak.....	152
Appendix D: Phi Scan Standard Operating Procedure.....	154
Appendix E: Center of Rotation Standard Operating Procedure.....	156
Appendix F: High Resolution X-Ray Diffraction Modeling with RADS.....	160
Appendix G: Texas State Instrument Workstations.....	163

APPENDIX A: RADICAL ASSIST-ION BEAM SPUTTERING SYSTEM



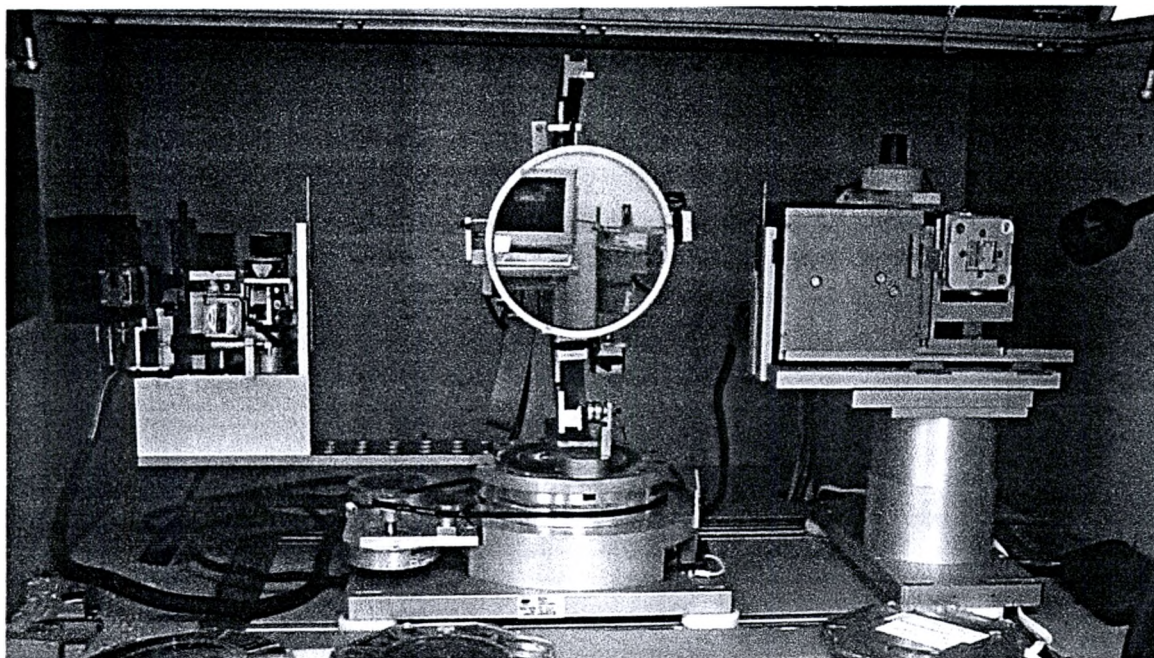
1. Work Chamber Refrigeration Unit – re-circulates water through the casing of the work chamber to keep it cool.
2. Small Mechanical vacuum pump – keeps air from entering the work chamber in the sample stage area when moving sample shield.
3. Pressure monitor and controller – regulates and gives the status of the turbo pump
4. Roughing Pump – The first pump used in the initial evacuation process. This mechanical pump is capable of bringing the work chamber down to the rough vacuum range ($\sim 10^{-2}$ torr).
5. Backing Pump – This mechanical pump backs the turbo pump.
6. Turbo Pump – This is the second pump introduced into the vacuum system. When the roughing pump reaches its limit, the turbo pump is activated to bring the chamber pressure down to high vacuum range ($\sim 10^{-5}$ torr).
7. Residual Gas Analyzer (RGA) – With the assistance of a computer interface the RGA is able to identify what gasses are present inside the chamber. This device can be used to identify several species of gasses during the sputtering process, and is also useful in determining the identity and location of leaks.

8. Valves – these two valves control which pumps have access to the chamber.
9. Bourdon Gauge- this gauge is used to determine the pressure in the work chamber during the initial pump down process. This gauge is useful down through the rough vacuum range.
10. Work Chamber – The stainless steel work chamber houses the sample, targets, and the plasma used for sputtering.
11. Kaufmann 3 cm Gridded Ion Source – This unit, also called the target source, ignites and sustains the sputtering plasma.
12. Stage controller – allows the operator to shield, orient, and rotate the sample.
13. Cooling System Valves – Interlock device that channels cooling system operation.
14. Flow control gauges – Interlock device that indicates proper cooling system operation.
15. Cryo-pump-partially responsible for bringing the work chamber to its lowest vacuum. Uses extremely cold temperatures to trap gas atoms that drift into its chamber.
16. Mass flow controllers – coupled with the electronic component, the mass flow controllers determine which gases, and how much of each, are entering the chamber at a given time.
17. Gas on/off switches – allows the operator to determine which gasses should be entering the system. Each toggle switch is for a different gas.
18. Backstreaming Traps – keep contaminants (i.e. mechanical pump oil) from entering the chamber through the vacuum pumps.
19. Assist Beam - houses another sputtering gun that is not used for sputtering but produces secondary ions to attune growth kinetics.

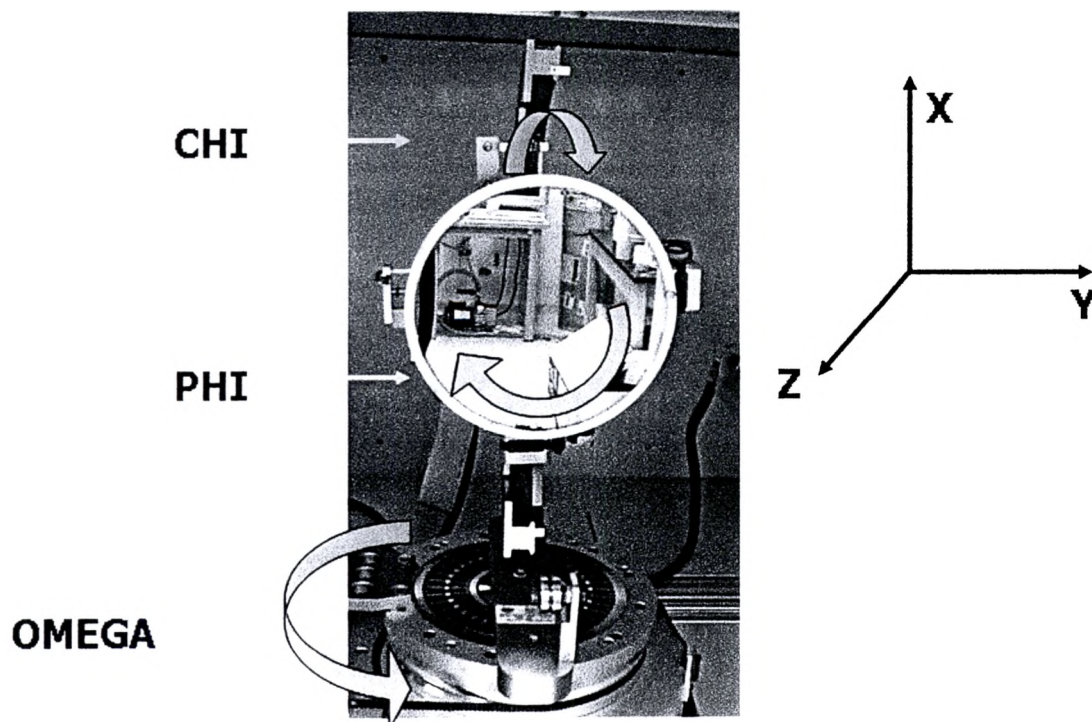


- A. R F Source (Primary Target)
Normal operation @ 300Watts
Used to energize plasma
- B. R F Source (Atomic source)
Normal operation @ 300Watts
Used to energize plasma
- C. Amp/Volt meter
- D. Timer
- E. Master Interlock
- F. Glassman Voltage Supply (Beam/Screen)
- G. Glassman Voltage Supply (Accelerator)

- H. Assist Beam Ion Drive
- I. Intermediate vacuum Gauge
 10^{-1} Torr – 10^{-4} Torr
- J. Regeneration Vacuum Gauge
Used when regenerating Cryo Pump
- K. High Vacuum Ion Gauge
 10^{-4} Torr – 10^{-8} Torr
- L. Automatic controls indicator panel
Indicates system activity
- M. Auto-tune Plasma Controller for Atomic Source
- N. Electronic Control Panel for mass flow controllers (MFCs)
- O. Gas Pulser / Neutralizer Current
- P. Neutralizer Filament current meter
- Q. Target Indexer Control/Indicator
- R. Cryogenic pump temperature
- S. PC Computer monitor
- T. High vacuum valve control and indicator
- U. Cryogenic pump regeneration control and indicator
- V. Rough vacuum valve control and indicator
- X. Back Fill valve control and indicator
- Y. Cryogenic Pump back Fill valve control and indicator
- Z. Mechanical Pump control and indicator
- AA. High vacuum pump control and indicator
- BB. Stage heater control
- \$ Not currently in use

APPENDIX B: BEDE D1 DIFFRACTOMETER

The sample stage hold up to 200mm wafers with full goniometer range of motion in Omega, X, Y, Z, Phi, and Chi



APPENDIX C: HOW TO FIND AN ASYMMETRIC PEAK

- Choose a well known symmetric peak with Miller indices (h, k, l)
- Choose an asymmetric peak with Miller indices (h', k', l')
- Using the following equation, solve for Ψ

$$\cos \Psi = \frac{hh' + kk' + ll'}{\left(\sqrt{h^2 + k^2 + l^2} \right) \left(\sqrt{h'^2 + k'^2 + l'^2} \right)}$$

- Using the ICDD or similar crystal database, look up the expected 2θ position for your symmetric peak
- Look up the expected position for your asymmetric peak
- Find the difference between your asymmetric peak position and your symmetric position and label it $\Delta 2\theta$
- Scan your material and note your observed symmetric peak position
- Add $\Delta 2\theta$ to your observed symmetric peak position and use that as your 2θ setting for your asymmetric peak scan
- Divide 2θ by 2 to find your expected ω
- Subtract this value from Ψ to get your ω setting

Note: Under the sample window in Bede Control, you have the option of letting the software perform this calculation for you. However, the material must be defined in the database. Simply select the material in question and select the Miller plane you want to find or manually enter the h, k, l indices. The program will return 2θ , ω , and χ values.

Now you are ready to start scanning for the asymmetric plane.

- 1) Remove all detector slits
- 2) Set 2θ and ω to the positions calculated in the previous section
- 3) Perform a narrow 2θ – ω scan (range 5°)
- 4) If you see the presence of a diffraction peak go to step 6 otherwise go to step 5
- 5) Scan Φ over a limited range (90°) to locate the peak
- 6) Insert 2mm vertical slits in the front and rear detector positions
- 7) Optimize the peak in ω and χ
- 8) Perform a triple axis rocking curve with the appropriate slits

APPENDIX D: PHI SCAN STANDARD OPERATING PROCEDURE

1. Locate the principle substrate peak in HRXRD mode in the normal fashion
2. Record the 2Theta position and Omega positions (ex. 2Theta = 44.8, Omega = 22.4)
3. Move 2Theta-Omega on top of the peak
4. Scan Omega, record the highest value (ex. Omega max = 21.73)
5. Return to Control Window and move Omega to max position (21.73)
6. Calibrate Omega to $\frac{1}{2}$ 2Theta Value (c \rightarrow 22.4)
7. Go to peak tools and optimize Omega with Chi
8. Record Maximized values for 2Theta, Omega, and Chi Observed

Use sample window in Bede Control or PCPDFWIN database to determine expected positions for the observed peak (note, you must know the miller indices of the peak in question)

Set up a table to keep track of expected and observed positions, for example:

ZnO (002)	observed	Expected	Delta = obs-exp
2Theta	34.186	34.4213	-0.2352
Omega	17.0832	17.2107	-0.1275
Chi	-0.1008	0	-0.1008

Now use sample window in Bede Control to determine the expected position of the asymmetric peak position

ZnO (012)	expected	Delta	Obs = exp+delta
2Theta	47.539	-0.2352	47.3038
Omega	23.7695	-0.1275	23.642
Chi	42.7685	-0.1008	42.6677

Move 2Theta, Omega, and Chi to your calculated observable positions and scan Phi

For your initial scan:

- scan with NO detector slits in place to ensure that the detector has the best chance of picking up the very narrow phi peaks
- scan over a smaller range (180deg)
- use a smaller step size (0.01deg) and longer count time (0.3 sec)

Once you are confident with the procedure and more familiar with the material being investigated, you'll want to:

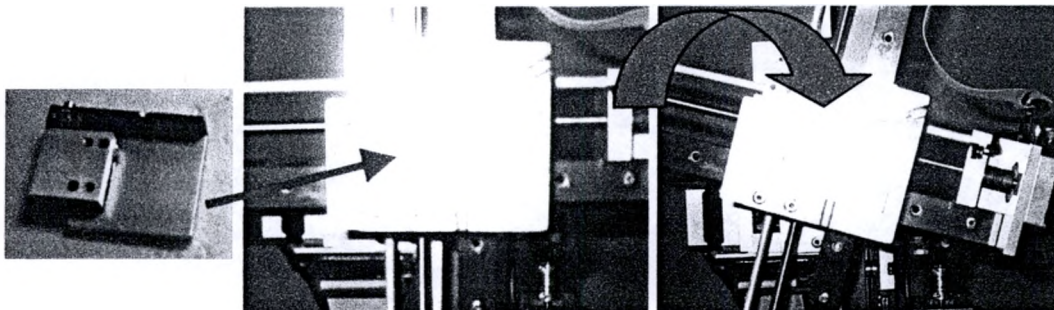
- Scan over the full range (360deg)
- Scan using larger stepsize (0.02deg) and shorter count time (0.1 sec)
- Scan using 5mm and 2mm detector slits to cut down on noise
- Phi scan both the substrate and epitaxial layers to show their related symmetry

APPENDIX E: CENTER OF ROTATION STANDARD OPERATING PROCEDURE

*****Prior to beginning Center of Rotation align the system in 2-bounce mode.**

1. Preparation

Place 50 μm special slit and rotate Φ to 90 degrees



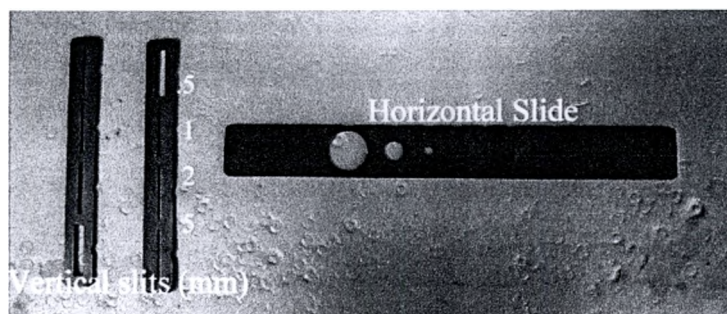
Set generator to 40/40 (ensure the detector is not saturated, i.e. >15 million cps)

Move x , y , z , ω , 2θ , and χ to zero

Remove all detector slits

Move horizontal slide to vertical slit and place the 1mm vertical slit in front of the optics stage

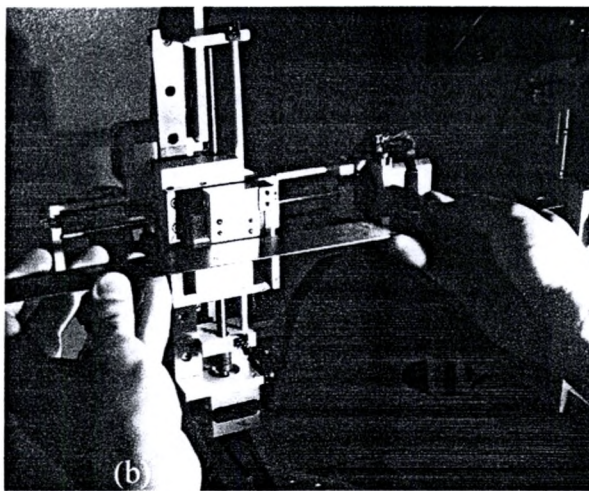
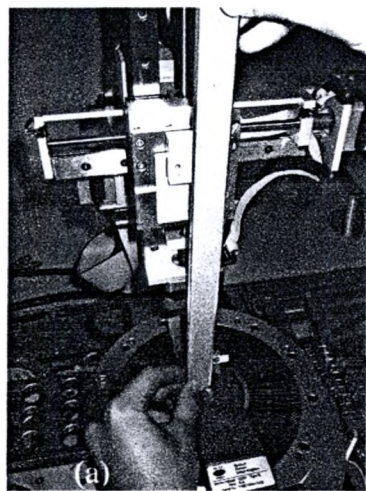
No attenuator



2. Align 50 μm special slit

As in Figure (a) move stage in x direction until the front plate of the 50 μm slit is aligned with the center of the screw at the base of the sample stage

As in Figure (b) move stage in y direction until the 50 μm slit is aligned with the vertical slit in front of the optics stage



3. Z position

Scan Z to get maximum counts per second (note cps)

Move Z to this position and record as Z_1

Move ω 180 degrees

Scan Z to get maximum counts per second (note cps)

Record this position as Z_2

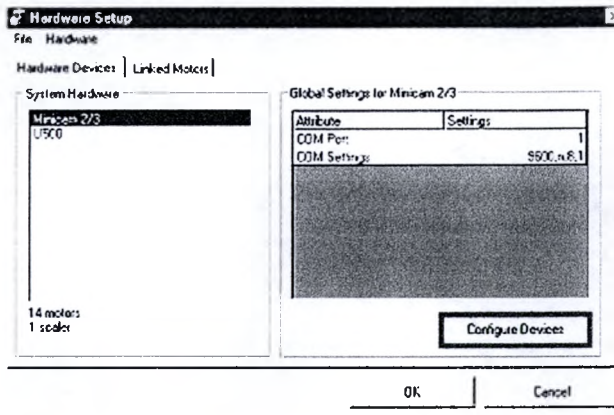
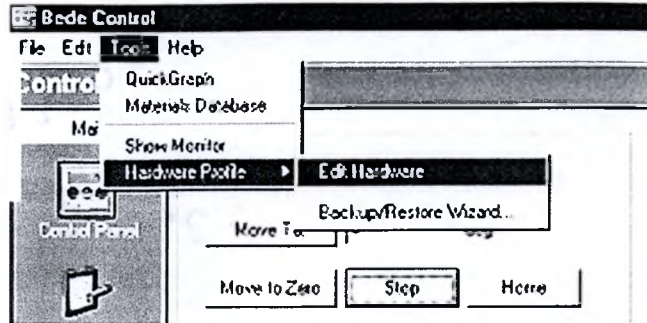
Move Z to $(Z_1+Z_2)/2$ and calibrate to zero

Move ω to zero

4. Source to detector alignment

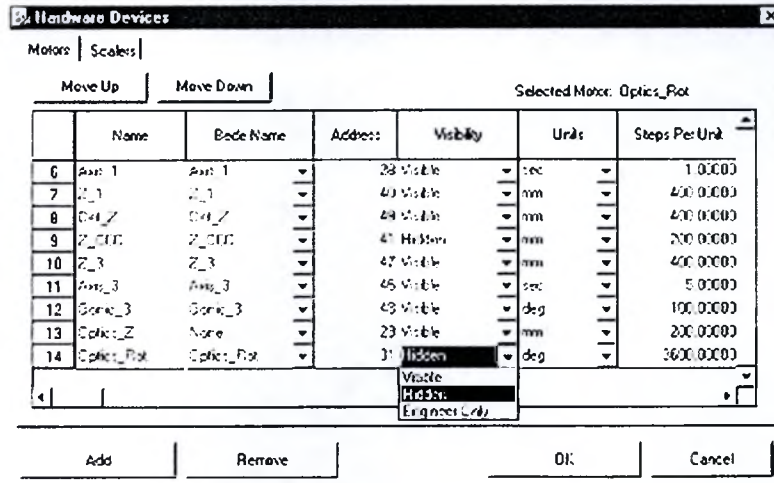
Insert 2mm front and back detector slits

Click tools
Hardware profile
Edit Hardware



Click Configure Devices

Change Optics Rot to visible



5. Scan optics rot (Range 1.5, Step 0.02)

Record peak position

Move optics rot to peak

Calibrate to zero (hit C, 0, OK)

Rehide Optics Rot

6. Scan optics Z (Range 5, Step 0.05)

Record peak position

Move optics Z to peak

Calibrate to zero

7. Scan 2θ (Range 2, Step 0.02)

Record peak position

Move 2θ to peak

Calibrate to zero

8. Scan Det Z (Range 5, Step 0.05)

Record peak position

Move Det Z to peak

Calibrate to zero

*Move Φ back to 0 degrees and remove the special slit

Congratulations! The Goniometer has been moved to the center of the x-ray beam.

Remember to move x-y to the appropriate positions for your sample.

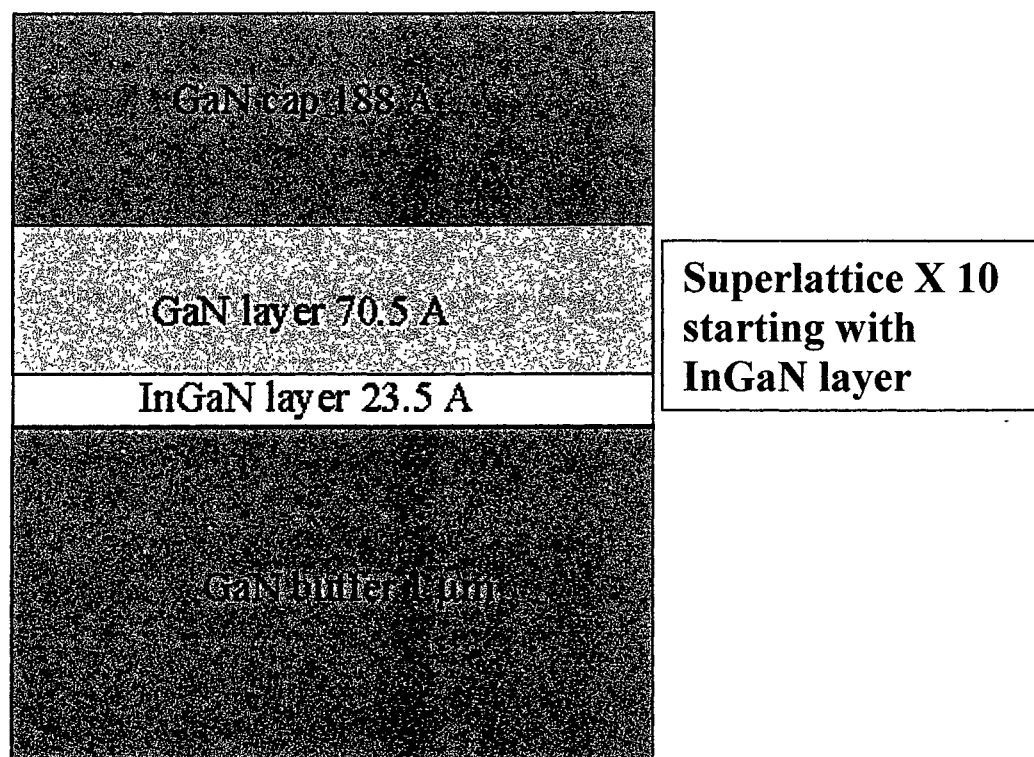
APPENDIX F: HIGH RESOLUTION X-RAY DIFFRACTION MODELING WITH RADS

We have conducted a preliminary investigation of the MQW structure STR204/6. The HRXRD scans were taken on our Bede D1 diffractometer using 2-bounce mode conditioned (Si CCC's) monochromatic Cu $K\alpha 1$ radiation. The scan parameters are as follows:

Scan Type: Omega-2Theta
 Range: 22000"
 Step Size: 10"
 Counting: 2 sec/point continuous

We have used the nominal layer model as depicted below.

Proposed Layer Model for MQW

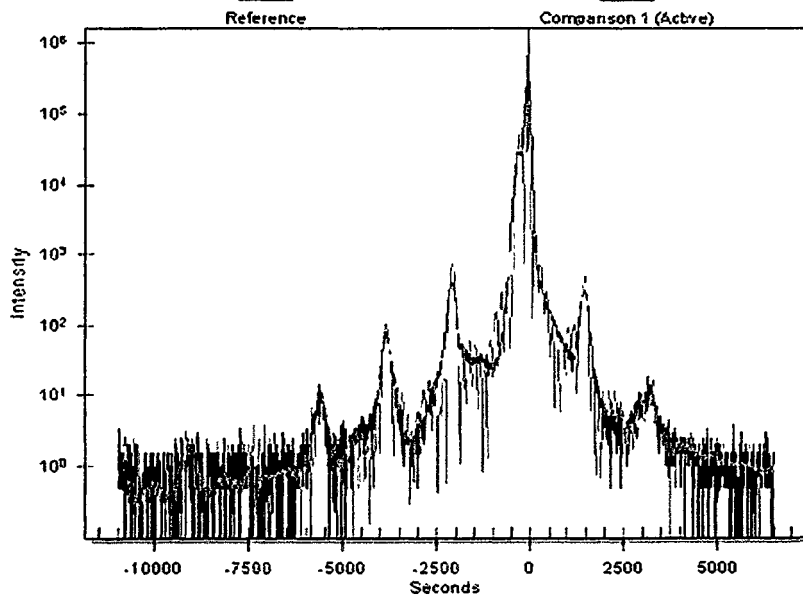


The program I used to fit the data is called RADS and is a component of the Bede program suite. The program uses dynamical simulation with seed values to match the data points. The assumptions I made during the simulation were:

- GaN buffer was thick enough to treat as the substrate
- All GaN layers were 100% relaxed
- (0002) reflections only

The data match is shown below with seed and calculated values.

Model | Graph | Iterations | Errors



Std Error 0.235 Iterations 6313

Normalization Factors

Incident	Low	High
1.727E+6	1E+5	5E+5

Background	Low	High
0.11	0	10

Substrate Peak Position
-87.7

Populations
40

Generations
1000

Diffuse Scatter

Diffuse Curve
None

Peak Position

Amplitude	Width	Peak Shape

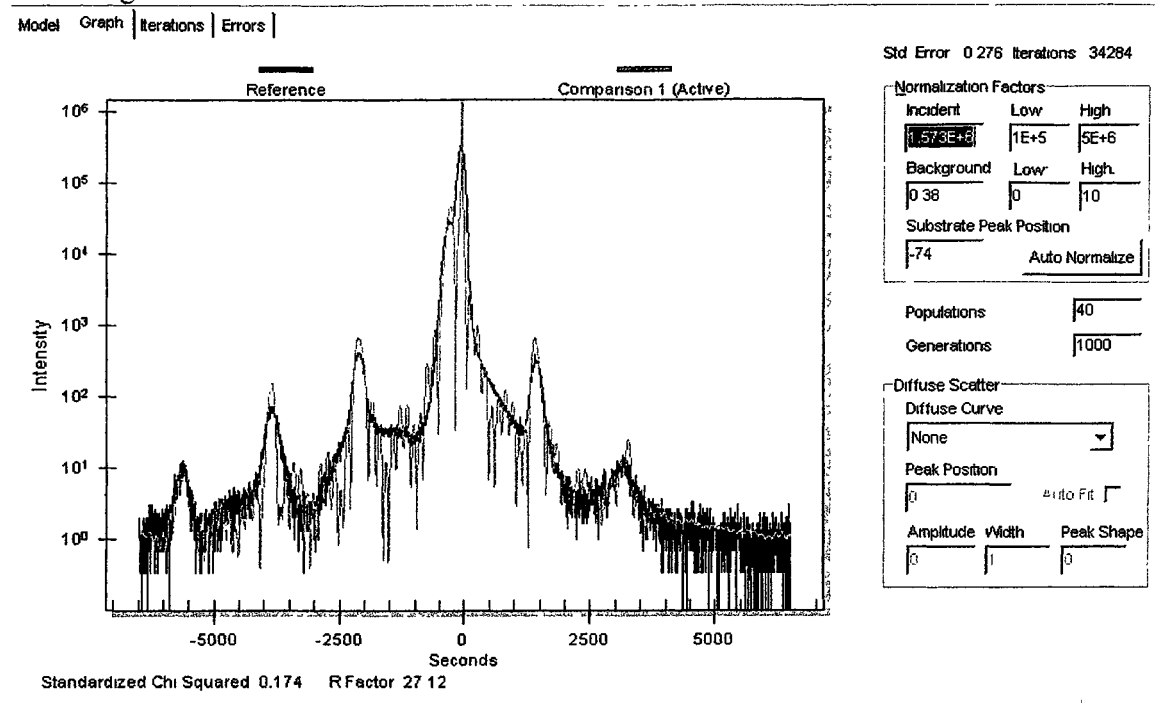
x = -3164, y = 2.923E4

Model | Graph | Iterations | Errors

	Thickness		Material	X		Y		Relaxation	Strain	
	Low	High		Low	High	Low	High		Low	High
21	182.15	150	GaN [hexagonal]	0.0000	0	0.0000	0	100	0	0
20	65.61	50	GaN [hexagonal]	0.0000	0	0.0000	0	100	19.7	0
1...	27.45	15	In _x Ga(1-x)N [hexagonal]	0.0795	0.03	0.5	0.0000	0	10.8	0
Sub.	∞	∞	GaN [hexagonal]	0	0	0	0	0	0	0

As you can see, our simulation yields a slightly thicker InGaN layer and a slightly thinner GaN layer within the superlattice but the period is less than 1% different than the nominal value of 94 Å. The relative atomic percentage for In is ~8%. Finally, the cap layer is only 3% smaller than the nominal value. The large value for strain within the superlattice is still a bit of an anomaly because I ran the same simulation without this parameter included only to get nearly identical results.

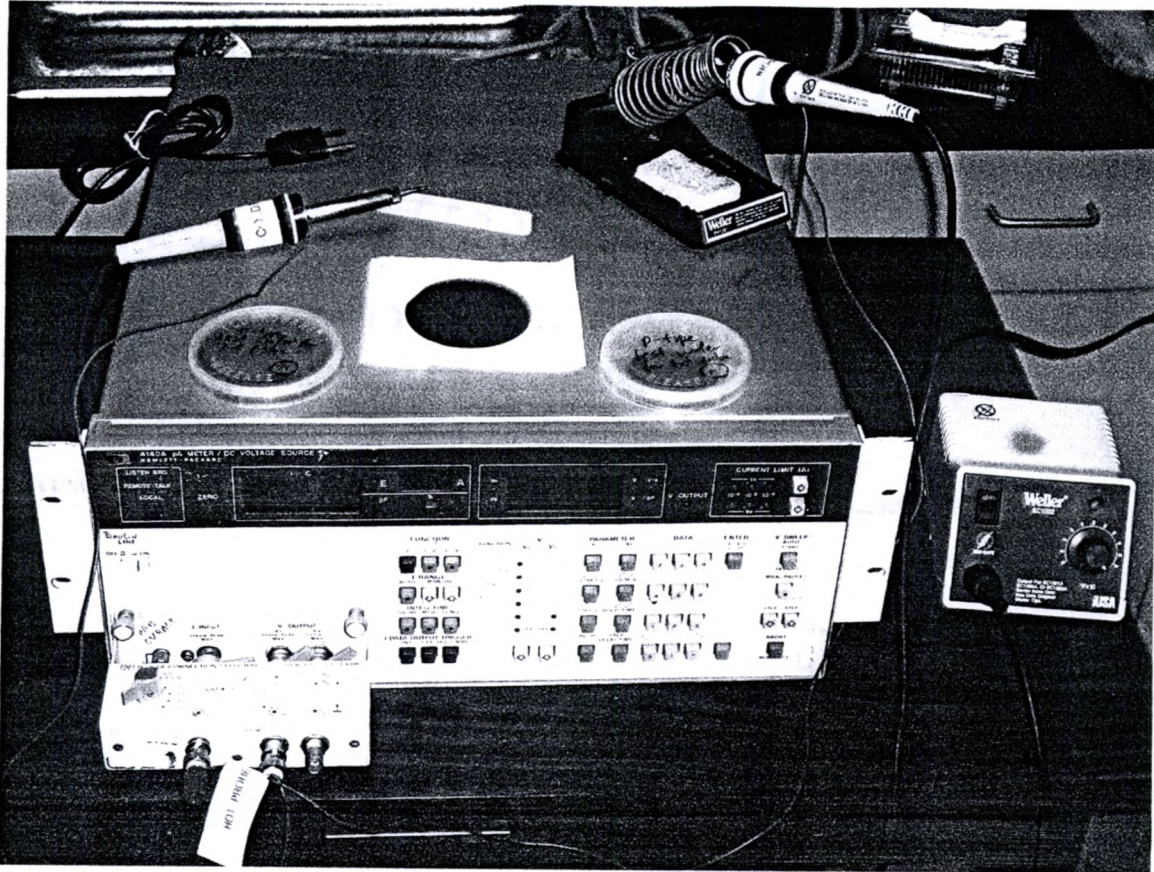
I also performed an analysis of a scan over a shorter range without strain to get the following results:



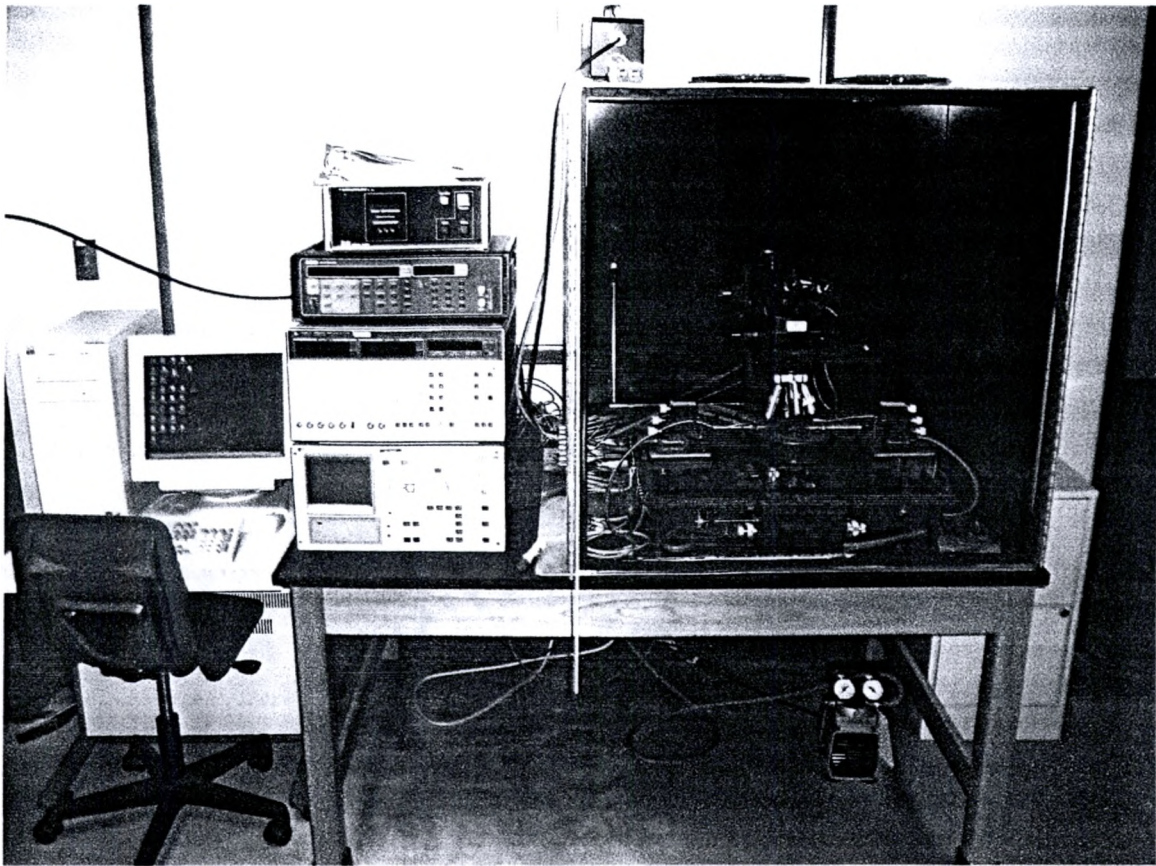
Model Graph Iterations Errors

	Thickness	Low	High	Material	X	Low	High	Y	Low	High	Relaxation	Strain	Low	High
21	241.95	150	250	GaN [hexagonal]	0.0000	0	0	0.0000	0	0	100	0	0	0
...20	66.03	50	100	GaN [hexagonal]	0.0000	0	0	0.0000	0	0	100	0	0	0
1...	27.83	15	50	In(x)Ga(1-x)N [hexagonal]	0.0871	0.05	0.5	0.0000	0	0	0	0	0	0
Sub.	∞	∞	0	GaN [hexagonal]	0	0	0	0	0	0	100	0	0	0

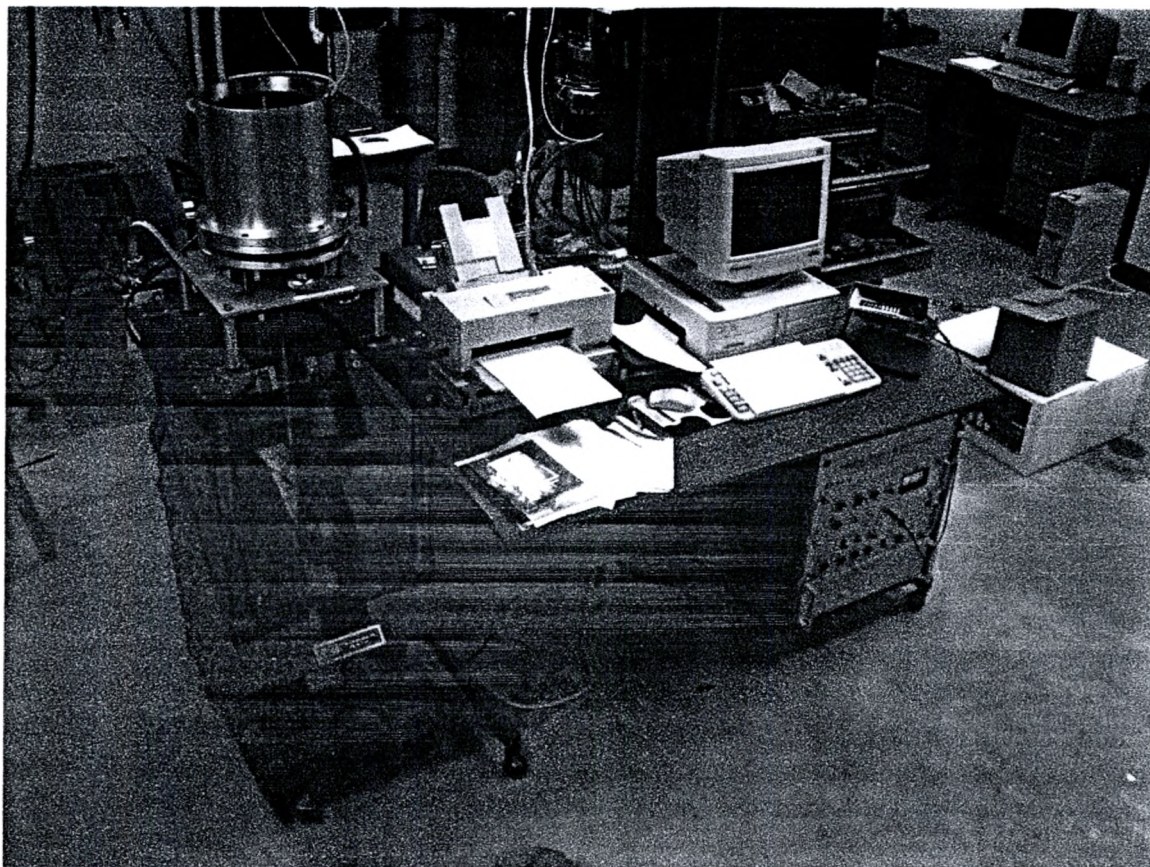
Here we see a little more deviation from the nominal value of the cap layer while superlattice values are almost unchanged. There is also a slight increase for the predicted amount of Indium to 8.71%.

APPENDIX G: TEXAS STATE UNIVERSITY WORKSTATIONS

Texas State Physics Thermal EMF Setup



Texas State Physics Contact Probe Workstation



Texas State Physics VSM Workstation

BIBLIOGRAPHY

- ¹C. Kittel, *Introduction to Solid State Physics*, 7th Ed. (John Wiley & Sons, New Jersey, 1996), pp 197-231.
- ²R. Harris, *Nonclassical Physics* (Addison-Wesley, California, 1998), pp.425-449.
- ³Carl Hepburn, Britney's Guide to Semiconductor Physics, WWW Document, (<http://britneyspears.ac/physics/basics/basics.htm>).
- ⁴R. Victor Jones, *Band Gap Engineering*, WWW Document, (http://people.deas.harvard.edu/~jones/ap216/images/bandgap_engineering/bandgap_engineering.html).
- ⁵Ioffe Institute, *New Semiconductor Materials. Characteristics and Properties*, WWW Document, (<http://www.ioffe.rssi.ru/SVA/NSM/Semicond/index.html>).
- ⁶B. Streetman and S. Banerjee, *Solid State Electronic Devices*, 5th Ed. (Prentice Hall, New Jersey, 1999) p. 524.
- ⁷Ed. D. Lide, *CRC Handbook of Chemistry and Physics*, 76th edition (CRC Press, Florida, 1995).
- ⁸Y. Chen *et al.*, J. Appl. Phys. **84** (7), 3912 (1998).
- ⁹S. Li, *Nitrogen Doped Zinc Oxide Thin Film*, UC Berkley, Thesis.
- ¹⁰S.J.Pearson *et al.*, Superlattices and Microstructures **34**, 3 (2003).
- ¹¹W. Wong, *Integration of GaN Thin Films with Dissimilar Substrate Materials by Wafer Bonding and Laser Lift-off*, UC Berkley, Dissertation.

- ¹²C. Cocksun et al, *Semicond. Sci. Technol.* **19**, 752 (2004).
- ¹³Ed. C. Chesterman, *National Audubon Society Field Guide to North American Rocks and Minerals*, (Alfred A. Knopf, New York, 1995), pp. 395.
- ¹⁴L. Berger, *Semiconductor Materials* (CRC Press, Florida, 1997), pp.183-187.
- ¹⁵T. Tsurumi et al., *Jpn. J. Appl. Phys.* **38**, 3682 (1999).
- ¹⁶Y. Chen et al., *Appl. Phys. Lett.* **76** (5), 559 (2000).
- ¹⁷H-J Ko et al., *J. Appl. Phys.* **92** (8), 4354 (2002).
- ¹⁸F. Vigue et al., *Appl. Phys. Lett.* **79** (2), 194 (2001).
- ¹⁹K. Hermann, *Cluster Studies on Metal Oxides and Surface Crystallography*, WWW Document, (<http://www.fhi-berlin.mpg.de/th/personal/hermann/ZnO.gif>).
- ²⁰S. J. Heyes, *Structures of Simple Inorganic Solids*, WWW Document, (http://www.chem.ox.ac.uk/icl/heyес/structure_of_solids/Lecture2/Lec2.html#anchor9).
- ²¹A. V. Chichagov, *Crystallographic Database for Minerals*, WWW Document, (http://database.iem.ac.ru/mincryst/s_carta.php?ZINCITE+5250).
- ²²Naval Research Lab, *Crystal Lattice Structures*, WWW Document, (<http://cst-www.nrl.navy.mil/lattice/spcgrp>).
- ²³F. Decremps et al., *Phys. Rev. B* **68**, 104101 (2003).
- ²⁴R. Ondo-Ndong et al., *Mat. Sci. and Eng. B* **97**, 68 (2003).
- ²⁵M. Matsuoka et al., *J. Appl. Phys.* **63** (6), 2098 (1988).
- ²⁶K.B Sundaram and A. Khan, *Thin Solid Films* **295**, 87 (1997).
- ²⁷I. Ohkubo et al., *Appl. Surf. Sci.* **159**, 514 (2000).
- ²⁸Y. Yoshino et al., *Vac.* **59**, 538 (2000).
- ²⁹J. Lee et al., *Mat. Res. Symp. Proc.* **666**, O8.20.1 (2001).

- ³⁰A. Barker *et al.*, Sens. and Act. A **58**, 229 (1997).
- ³¹Marketech Inter. Inc., *Sapphire Materials*, WWW Document,
(<http://www.mktintl.com/sapphires/>)
- ³²J. Narayan *et al.*, J. Appl. Phys. **84** (5), 2597 (1998).
- ³³I. Ohkubo *et al.*, Surf. Sci. **443**, L1043 (1999).
- ³⁴K.-K. Kim *et al.*, J. Appl. Phys. **87** (7), 3573 (2000).
- ³⁵P. Fons *et al.*, Appl. Phys. Lett. **77** (12), 1801 (2000).
- ³⁶F. Vigue *et al.*, J. Appl. Phys. **90** (10), 5115 (2001).
- ³⁷S. Park *et al.*, Appl. Phys. Lett. **77** (3), 349 (2000).
- ³⁸J.-M. Myoung *et al.*, Jpn. J. Appl. Phys. **41**, 28 (2002)
- ³⁹S. Yamauchi *et al.*, J. Crys. Gro. **214**, 63 (2000).
- ⁴⁰T. Nakamura *et al.*, Thin Solid Films **411**, 60 (2002).
- ⁴¹M. Joseph *et al.*, Physica B **302**, 140 (2001).
- ⁴²D. Gerhnsen *et al.*, Appl. Phys. Lett. **81** (21), 3972 (2002).
- ⁴³Y. Chen *et al.*, Appl. Phys. Lett. **78** (21), 3352 (2001).
- ⁴⁴H.-J. Ko *et al.*, J. Appl. Phys. **92** (8), 4354 (2002).
- ⁴⁵C. Van de Walle, Phys. Rev. Lett. **85** (5), 1012 (2000).
- ⁴⁶N. H. Nickel and K. Fleischer, Phys. Rev. Lett. **90** (19), 197402 (2003).
- ⁴⁷Hofmann *et al.*, Phys. Rev. Lett. **88** (4), 045504 (2002).
- ⁴⁸M. Kunat *et al.*, Phys. Rev. B **66**, 081402 (2002).
- ⁴⁹S. B. Zhang *et al.*, Phys. Rev. B **63**, 075205-1 (2001).
- ⁵⁰M. K. Jayaraj *et al.* Bull. Mater. Sci. **25** (3), 227 (2002).
- ⁵¹H. Naiwa, *Handbook of Thin Film Materials* (Academic Press, San Diego CA, 2002)

- ⁵²Y. Yan et al., Mat. Res. Soc. Symp. Proc **666**, f.2.6.1-f.2.6.11 (2001).
- ⁵³E-C. Lee *et al.*, *First-principles study of the compensation mechanism in N-doped ZnO*,
Korea Advanced Institute of Science and Technology.
- ⁵⁴Y. Sato and S. Sato, Thin Solid Films **281**, 445 (1996).
- ⁵⁵K. Iwata et al., J. Crys Growth **209**, 526 (2000).
- ⁵⁶X. Wang et al., J. Crys. Growth **226**, 123 (2001).
- ⁵⁷X-L. Guo et al., J. Crys. Growth **237**, 544 (2002).
- ⁵⁸S. Yamamuchi et al., J. Crys. Growth **260**, 1 (2004).
- ⁵⁹K. Minegishi *et al.*, Jpn. J. Appl. Phys. **36**, L1453 (1997).
- ⁶⁰D. C. Look et al., Appl. Phys. Lett. **81** (10), 1830 (2002).
- ⁶¹A. N. Georgobiani *et al.*, Nuc. Ins. & Meth. Phys. Res. A **514**, 117 (2003).
- ⁶²T. Yamamoto, Thin Solid Films **420**, 100 (2002).
- ⁶³L. G. Wang, and A. Zunger, Phys. Rev. Lett. **90** (25), 256401-1, (2003).
- ⁶⁴M. Joseph et al., Jpn. J. Appl. Phys. **38**, L1205 (1999).
- ⁶⁵K. Nakamura *et al.*, App. Phys. Lett. **79** (25), 4139 (2001).
- ⁶⁶K. Nakamura *et al.*, J. Crys. Growth **237**, 503 (2002).
- ⁶⁷M Komatsu et al., App. Surf. Sci. **189**, 349 (2002).
- ⁶⁸A. V. Singh *et al.*, J Appl. Phys. **93** (1), 396 (2003).
- ⁶⁹K. Sato and K. Yoshida, Jpn. Soc. Appl. Phys. **2** (6B), L555 (2000).
- ⁷⁰K. Sato and K. Yoshida, Physica B **308**, 904 (2001).
- ⁷¹K. Sato and K. Yoshida, Physica E **10**, 251 (2001).
- ⁷²K. Sato and K. Yoshida, Mat. Res. Soc. Symp. Proc. **666**, F4.6.1 (2001).
- ⁷³T. Fukumura et al., Appl. Phys. Lett. **75** (21), 3366 (1999).

- ⁷⁴T. Fukumura et al., Appl. Phys. Lett. **78** (7), 958 (2001).
- ⁷⁵Z. Jin et al., J. Crys. Growth **214**, 55 (2000).
- ⁷⁶Z. Jin et al., Physica E **10**, 256 (2001).
- ⁷⁷T. Fukumura et al., Appl. Phys. Lett. **78**, (24) 3824 (2001).
- ⁷⁸G-C. Yi et al., Appl. Phys. Lett. **80** (24), 4561 (2002).
- ⁷⁹P. Sharma et al., Nat. Mat. **2**, 673 (2003).
- ⁸⁰W. Sobie, *Ion Beam Technology for Thin Film Applications*, Vac. & Thinfilm reprint (1999).
- ⁸¹Kratos Analytical, *The Kauffman Ion Source*, WWW Document, (<http://www.kratos.com/EApps/Kaufmn.html>)
- ⁸²Dr. Carlos J. Gutierrez, *Radical Beam-Ion Beam Sputtering (RB-IBS): A New Strategy for Artificially-Structured Materials Engineering*, presentation
- ⁸³Oxford Applied Research, *RF Atom Sources*, WWW Document, (<http://www.oaresearch.co.uk/RFatom.htm>)
- ⁸⁴J. Brehm, W. Mullin, *Introduction to the Structure of Matter* (John Wiley & Sons, New Jersey, 1989), pp103-117.
- ⁸⁵Dr. Carlos J. Gutierrez, *The Physics of Grazing Incidence X-ray Diffraction of Microelectronic Material*, SCCCM Workshop, presentation.
- ⁸⁶ETH E-Collection, *(X-ray) Diffraction*, WWW Document, (http://e-collection.ethbib.ethz.ch/ecol-pool/lehr/lehr_54_folie2.pdf)
- ⁸⁷J. Connolly, *Introduction to X-Ray Powder Diffraction*, WWW Document, (<http://epswww.unm.edu/xrd/xrdclass/06-Diffraction-II.pdf>)
- ⁸⁸ Isabel Gallardo, *Introduction to X-Ray Diffraction*, Poster Presentation

- ⁸⁹Dr D Keith Bowen, *High Resolution X-ray Methods on the D1 diffractometer*, Bede Scientific Incorporated, presentation.
- ⁹⁰A. Vailionis, *Diffraction: Real Samples*, WWW document, (http://www-lam.stanford.edu/xlab/MatSci162_172/LectureNotes/04_Real%20Samples.pdf)
- ⁹¹T. Makino et al., *App. Phys. Lett.* **79** (9), 1282 (2001).
- ⁹²Oliver Kappertz, *Atomistic effects in reactive directcurrent sputter deposition*, WWW Document, (http://sylvester.bth.rwth-aachen.de/dissertationen/2004/063/04_063.pdf)
- ⁹³David Baselt, *The tip-sample interaction in atomic force microscopy and its implications for biological applications*, WWW Document, (<http://stm2.nrl.navy.mil/how-afm/how-afm.html#General%20concept>)
- ⁹⁴Bart J. Van Zeghbroeck, *The "hot-probe" experiment*, WWW Document, (<http://ece-www.colorado.edu/~bart/book/hotprobe.htm>)
- ⁹⁵NIST Semiconductor Electronics Division, *Hall Effect Measurements*, WWW Document, (<http://www.eeel.nist.gov/812/intr.htm>)
- ⁹⁶H. Groenland et al., *Vector Vibrating Sample Magnetometer*, WWW Document, (<http://www.el.utwente.nl/tdm/istg/research/vsm/vsm.htm>)
- ⁹⁷EM4: Magnetic Hysteresis, CHALMERS UNIVERSITY OF TECHNOLOGY, Lab manual

VITA

Casey Eben Smith was born in Fredericksburg, Texas, on July 28, 1977, the son of H. F. and Joan Smith. After completing his sophomore year of high school, he entered the Texas Academy of Math and Science, an early college admission program at the University of North Texas in Denton. He received the degree Bachelor of Arts from the University of Texas at Austin in May 1998. During the next four years he was employed as a science instructor at Canyon High School in New Braunfels, Texas. In September 2002, he entered the Graduate College of Texas State University-San Marcos.

Permanent Address: 1371 Scenic View Dr.

Canyon Lake, TX 78133

This thesis was typed by Casey Eben Smith.